THE CHARACTERIZATION AND APPLICATION OF A METHOD TO PREDICT THE BACKGROUND NEUTRON RESPONSE IN NUCLEAR SECURITY SYSTEMS

A Dissertation

by

JACKSON NICHOLAS WAGNER

Submitted to the Office of Graduate and Professional Studies of
Texas A&M University
in partial fulfillment of the requirements for the degree of

DOCTOR OF PHILOSOPHY

Chair of Committee,	Craig Marianno
Committee Members,	Sunil Chirayath
	Shikha Prasad
	Daren Cline
Head of Department,	Michael Nastasi

May 2021

Major Subject: Nuclear Engineering

ABSTRACT

Nuclear security operators employ gamma radiation spectroscopy and neutron counting techniques to locate radiological materials, particularly those that may be used for nuclear terrorism. One such method employed is the mobile radiological search system (MRSS). A challenge with an MRSS is its difficulty to discriminate background neutron signals. However, operational data suggested a linear relationship between the neutron count rate and the gamma spectrometer's high energy (>3 MeV) count rate. Such a relationship would enable the prediction of the neutron background, which would improve the MRSS's ability to discriminate non-environmental background responses. The purpose of this research was to verify this relationship, determine its source, and establish a method to predict neutron background in an MRSS. Verification measurements used a commercially available MRSS in a series of measurements in parking garages on Texas A&M University's campus. The natural variations of radiation background within the garages confirmed the correlation between the gamma and neutron radiation backgrounds. With the relationship verified, a cause for the correlation was sought. This was done through extended radiation background measurements using different configurations and types of gamma ray scintillators. Analysis of their high energy (4-85 MeV) spectra found that they were caused by muons. This result indicated that the correlation between the two detectors is significant: muons and neutrons are part of radiation background as both are produced by cosmic ray interactions with the Earth's atmosphere. Additional MRSS measurements sought to characterize this relationship by measuring locations throughout the Central

United States, sampling variables that affect the neutron and muon fluxes. These results showed that the neutron count rate followed a power law function of the muon count rate, indicating the neutron count rate indeed could be predicted. This prediction method was then applied to MRSS measurements of a parking garage while ^{252}Cf (a spontaneous fission neutron source) was present. These measurements found that the alarm method which came from the neutron prediction function performed properly when alerting for the presence of that radioactive material. Overall, these results show that MRSS operators can use similar systems to make such predictions, and the resulting alarm method should improve an MRSS's sensitivity to man-made radiological materials.

ACKNOWLEDGEMENTS

I would like to thank my committee chair, Dr. Marianno, and my committee members, Dr. Chirayath, Dr. Cline, and Dr. Prasad, for their guidance and support throughout the course of my research.

Thanks also go to my friends and colleagues and to the NUEN department faculty and staff for making my years at Texas A&M University enjoyable ones. Additionally, thanks are deserved to Texas A&M University and Brazos County officials for their work managing the COVID-19 pandemic, whose measures not only helped protect the public health but also enabled my research productivity to greatly increase.

I also wish to thank my mother and late father for their support and encouragement throughout my education while it has brought me so far away from home. And finally, I would like to thank my wife for being both a patient and supportive partner and an enormously helpful data collection assistant.

CONTRIBUTORS AND FUNDING SOURCES

Contributors

This work was supervised by a dissertation committee consisting of Professor Craig Marianno [advisor], Professor Sunil Chirayath, and Professor Shikha Prasad of the Department of Nuclear Engineering, and Professor Daren Cline of the Department of Statistics.

Some of the data analyzed in Chapter 4 were provided by Thomas McCullough formerly of the United States Department of Energy's Remote Sensing Laboratory at Joint Base Andrews. Additional data analyzed in Chapter 4 were provided by Kevin G. Hart of Sandia National Laboratories and Frank Moore of Argonne National Lab, both of whom are part of the United States Department of Energy's Radiological Assistance Program. Further data analyzed in Chapter 5 were also provided by Kevin G. Hart of Sandia National Laboratories and the United States Department of Energy's Radiological Assistance Program. These data WILL BE published in two separate articles in YEAR.

All other work for this dissertation was completed by the student independently.

Funding Sources

Graduate study was supported by a fellowship funded by the United States Nuclear Regulatory Commission (NRC) and a scholarship from the United States Department of

Defense (DoD) through their Science, Mathematics, and Research for Transformation (SMART) scholarship for service program.

NOMENCLATURE

CCG	Central Campus Garage (on Texas A&M University's campus)
DOE	United States Department of Energy
eV	electronvolt (SI unit of energy)
FLUKA	FLUktuierende KAskade (German: Fluctuating Cascade – a Monte Carlo Particle Transport Code)
FWHM	Full-Width at Half-Maximum
IAEA	International Atomic Energy Agency
IND	Improvised Nuclear Device
kT	kilotons of TNT (vis-à-vis explosive strength)
MCA	Multi-channel Analyzer
MCNP	Monte Carlo N-Particle (Transport Code)
MRSS	Mobile Radiological Search System
NIST	United States National Institute of Standards and Technology
NSG	North Side Garage (on Texas A&M University's campus)
PDT	Precision Data Technology
pmf	Probability Mass Function
PRG	Polo Road Garage (on Texas A&M University's campus)
PVT	Polyvinyl Toluene (a plastic scintillator material)
RAP	Department of Energy's Radiological Assistance Program
RDD	Radiological Dispersal Device
RED	Radiological Exposure Device

RSL	Remote Sensing Laboratory
SBG	Gene Stallings Boulevard Garage (on Texas A&M University's campus – formerly CAIN Garage)
SSG	Southside Parking Garage (on Texas A&M University's campus)
UCG	University Center Garage (on Texas A&M University's campus)
WCG	West Campus Garage (on Texas A&M University's campus)

TABLE OF CONTENTS

Page

LIST OF FIGURES

LIST OF TABLES

Page

1. INTRODUCTION

Nuclear security is necessary to counter the threat of nuclear terrorism, and an essential part of that is the ability to quickly find a nuclear device or other illicit radiological materials. A potential nuclear terrorism incident would likely occur using one of three types of devices: one that spreads radioactive material – a radiological dispersal device (RDD – otherwise known as a “dirty bomb”), one that exposes people to massive radiation doses – a radiation exposure device (RED), or one that achieves a nuclear detonation – an improvised nuclear device (IND). Recent events have shown the potential damage of a successful attack with an IND, specifically that of the devastating August 2020 explosion in Beirut, Lebanon. That explosion’s yield was estimated to be equivalent to 0.5-1.5 kilotons of TNT, approximately one twentieth the size of the 1945 Hiroshima nuclear bombing [1,2]. It is plausible that the explosive yield of an IND would meet or exceed that estimated one kiloton yield, which would result in similar, catastrophic damage to any city. Fortunately, these devices would emit radiation, and therefore, nuclear security operators can locate these devices before they detonate using radiation detection equipment.

Nuclear security operators work to locate these devices (or related radiological material) by employing methods to detect gamma rays and neutrons simultaneously. Measuring both types of radiation allows these operators to find a wide variety of radioactive isotopes, especially those that might be used in these devices. In these cases, spectroscopy systems are used to detect gamma rays, and simple counting systems are used to detect neutrons. Both detection methods require a quality characterization of the response to ambient (or background) radiation. This is necessary to be able to recognize a detector's response caused by man-made radiological material, especially that which might be used in illicit devices. If the detectors are static, this characterization is easily done by observing the detectors' responses for a short period. The averaged response over this period is then assumed to be constant and similar responses are ignored during measurements. However, some methods used by nuclear security operators that employ these detectors introduce complexities in characterizing their background response.

One common employment method for these detectors is the mobile search system, where the detectors are placed in a vehicle that canvasses an area of interest looking for any illicit material. This introduces a significant complexity in characterizing the background response since the detectors are constantly moving. Fortunately, this complexity is mitigated in the gamma spectroscopy system because it provides energy-dependent information [3]. In addition, the background gamma ray field has a spectrum of energies that is unique from those of any man-made source [4]. Thus, typical changes in the background gamma flux (and therefore the spectrometer's overall count rate) would cause no distinguishable change in the energy spectrum. Conversely, the neutron counting system does not have meaningful mitigation strategies as such systems only provide the neutron interaction rate in the detector. In mobile systems, this makes it difficult to determine whether small changes in the neutron count rate are the result of a normal change in the background neutron flux or the result of man-made radiological material. However, modified detection systems employed in mobile search operations have indicated a possible strategy.

Mobile search operations using a modified gamma spectrometer have shown a potential strategy to mitigate this issue for neutron counting systems. Specifically, it was noted that the count rate in the gamma spectrometer at high energies (much greater than 3 MeV) was correlated with the neutron count rate in background conditions [5]. In addition, tests noted that this high energy count rate was not affected by the presence of a neutron source [5]. That work suggested that this high energy response in the gamma spectrometer was the result of particles other than gamma rays – including exotic charged particles, but no conclusion was made. A well-defined relationship between the two would allow for the estimation of the background neutron response using the high energy spectrometer response throughout these mobile search operations.

The goal of this research was to define what caused this correlation, observe whether and how it varied with typical mobile search scenarios, and characterize and test a method to apply the correlation for neutron background prediction. When implemented, this prediction method would help reduce false alarms in these systems by better adjusting with normal changes in neutron background. Ideally, the method would increase the sensitivity of the neutron counting systems, allowing it to correctly indicate the presence of smaller amounts of neutron emitting radiological materials compared to current methods.

1.1. Background

1.1.1. Neutron Detection Using ^{3}He

Nuclear security operations typically use neutron counting systems when searching for illicit radiological material. The commonly employed system uses ^{3}He or some other gas to detect neutrons, which requires specific interactions between the neutrons and the atoms of the gas [3]. For these gas-filled detectors, neutrons are most likely to interact with the gas when the neutrons have very low kinetic energies, approximately 1 eV. Unfortunately, the average energy of background neutrons is 1 MeV, which Figure 1-1 shows is 1000 times less likely to be detected than 1 eV neutrons [6]. To improve the efficiency of these systems, the detectors are surrounded by polyethylene, a dense plastic. The polyethylene moderates – or slows down – the neutrons through collisions with the hydrogen atoms in the plastic, and this reduction in kinetic energy increases the chance they will interact with the gas [3]. Despite this improved efficiency, the background response in these detectors can be near zero for many situations. This is particularly true at locations near sea level, where average neutron count rates are approximately one count per second. This naturally depends on the number of detectors deployed, but ^{3}He is expensive, which greatly limits the number of detectors a security team uses. The low count rates present complexities when analyzing the distribution of counts that might occur due to background and deciding what is not from background, particularly if that background average count rate changes.

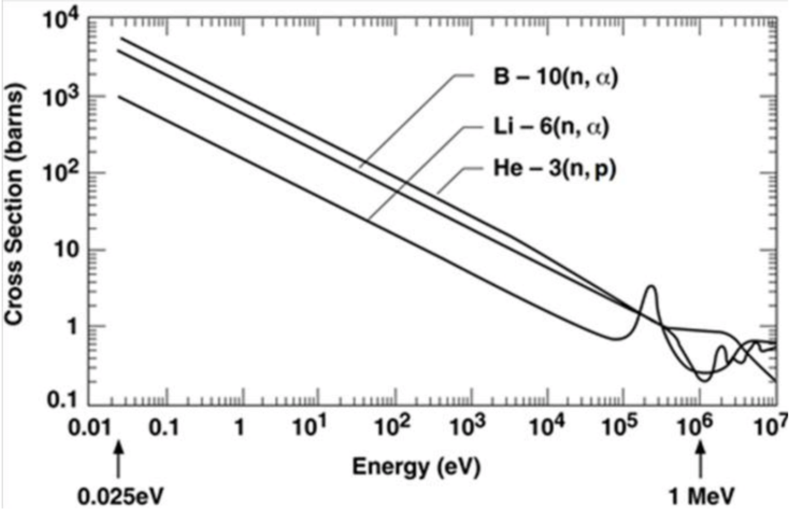

Figure 1-1. Neutron reaction cross sections for common detector materials (Reprinted from [6]).

1.1.2. Counting Statistics and Alarm Determination

The essential factor in using neutron counting systems is understanding when a detector's response is not caused by background. Any instantaneous observation using these systems will be one of a random distribution of count rates with a given average. As the number of these observations increases, the distribution of observed count rates will approach a true Poisson distribution, and its average will be proportional to the neutron flux. For example, Figure 1-2 shows a Poisson distribution of counts in one second from a system whose average result is one count per second. This distribution would indicate that for any single observation with this system, the most likely result (i.e. that with the highest probability) would be either zero or one count in one second. However, any result is possible as long as the distribution indicates a non-zero probability of that result (e.g. observing 6 counts in one second has a 0.05% chance to occur or is expected to occur once every 2000 observations).

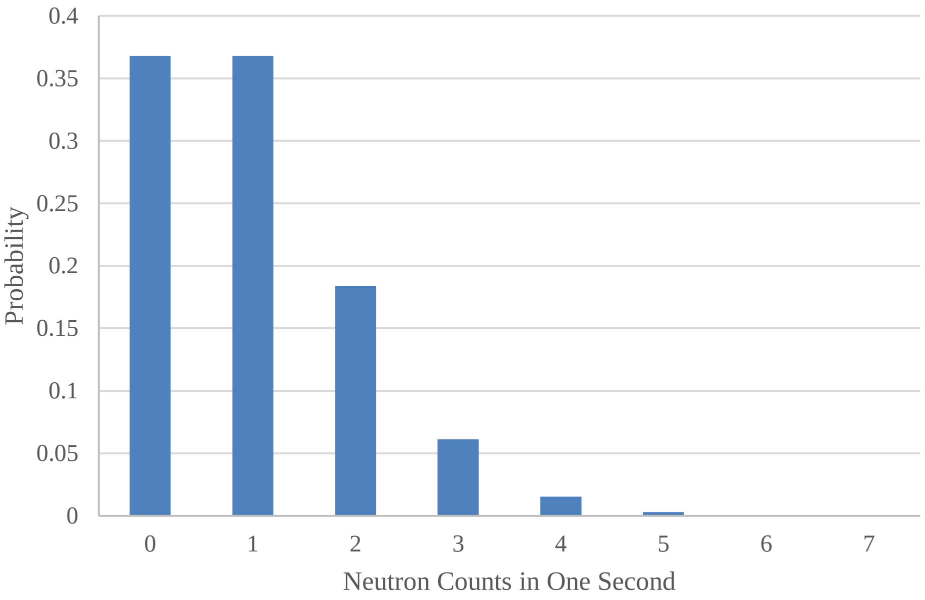

Figure 1-2. A Poisson probability distribution of counts in one second with an average of one. Counts with probability less than 10^{-5} are ignored.

If the distribution in Figure 1-2 was known to be the distribution for background, it can be used in reverse to determine if the detector is measuring man-made radiological materials. Instead of looking at the most likely count rate, operators would identify count rates that are above some critical level given this distribution and thus would produce a warning. They would typically choose a count rate such that it and those greater would have a cumulative probability of 5% or less according to the background distribution. In this example, that value (called the "alarm threshold") would be four. This means that if operators observe four or more counts in one second, there is only a 1.9% chance of it being the result of background (and thus a false positive/alarm). Conversely, those count rates would indicate that man-made materials are present with a 98.1% probability.

Neutron physics can cause problems with this method, particularly in warning for the presence of small amounts of man-made materials (i.e. amounts of material that cause relatively small changes to the average count rate). This is because many variables can cause small but significant changes to the background neutron flux, particularly elevation and surrounding buildings. Using the above example, consider a change to the neutron flux such that the detector's Poisson distribution now has an average of two counts in one second instead of one. The original alarm threshold of four counts or more in one second now has a 14.3% chance of occurring and triggering an alarm. If this change were the result of a normal background change, it being much higher than the standard probably of 5% would obviously lead to an increase in false alarms, causing nuclear security operators to spend precious time adjudicating them. However, if that change was the result of a small amount of radiological material, it has a high likelihood (85.7%) of not triggering an alarm resulting in operators missing that material. During an operation, answering the question of what might cause a change like this is important.

A further complication is the fact that it is difficult to determine the average count rate in the mobile search system's neutron counters. As noted above, it requires numerous observations of a given scenario for a Poisson distribution to develop. However, this cannot be done while the system is moving because it only can obtain one or a few observations for each situation. A long measurement at the start of a campaign can help mitigate this, but the variance in neutron background mentioned above can invalidate that observed average at various times during an operation. Similar concerns exist for the gamma spectrometers employed along with these neutron counters, but other features allow these detectors to better mitigate background changes.

1.1.3. Gamma Ray Detection Using NaI and PVT

The other radiation detection system used in nuclear security is the gamma spectrometer. These detectors commonly employ scintillation techniques using sodium iodide (NaI) or polyvinyltoluene (PVT). The detection system then counts the number of observations for each energy in a given time and presents that information in a single histogram or spectrum over a range of energies. What range of energies the detector "considers" depends on its calibrated scale, which changes based on settings like the voltage applied to the detection system. Naturally, counting statistics are also involved here for total observations overall and observations for each histogram bin. However, the detector's efficiency causes it to observe much higher count rates for background compared to the neutron counter. This causes the Poisson distribution to be more like a binomial or Gaussian distribution whose statistics are less complicated. However, these issues are rendered moot by the discrete nature of gamma radiation and the ability for the detector to distinguish the energy deposited. First, every gamma emitting isotope has a characteristic set of gamma rays. This coupled with the energy dependent response of the detector results in a unique spectrum for each material (or combination of materials) detected. This makes it simple to distinguish gamma rays from man-made materials from those from natural ones. While scintillation detectors are commonly used to detect gamma rays, it does not discriminate based on the particle that interact with it; this includes charged particles, whose interaction mechanisms are very different from gamma rays.

1.1.4. Charged Particle Interactions with Matter

Charged particles interact with materials through coulombic forces between themselves and the bound electrons within the material [3]. These forces cause the charged particle to lose kinetic energy while it travels through the material. The amount of energy lost per unit distance travelled is referred to as the stopping power, which depends on the mass and electric charge of the particle itself, the particle's kinetic energy, and the material's atomic composition and density. Because of this interaction, charged particles deposit energy along the path it travels through a material. This indicates that a charged particle would deposit energy in a scintillator dependent on its stopping power and the length it travels through the detector. Once this occurs, the detector emits light proportional to the amount of energy deposited; however, this energy is frequently higher than the detector's calibrated energy scale and is therefore not counted.

1.2. Objectives

The core objective of this research is to understand the relationship between the high energy count rate in the scintillator detector and the count rate in the neutron counter for mobile search systems. First, this will require understanding the cause of the high energy signals in the gamma spectrometer, its source, and how it varies in background conditions. The particles that cause these signals was determined using long background measurements with NaI and PVT gamma spectroscopy systems calibrated for high energies, and the results were confirmed using comparisons to simulations of similar scenarios using MCNP [7]. Understanding the source of these particles then came from literature review, and observation of their variance came from later measurements.

With the understanding of the cause, mobile search measurements were performed to obtain a representative sample of conditions that operational systems may experience. The majority of measurements took place as sweeps of urban areas, similar to those where operations frequently take place. More measurements collected data over a wide variety of elevations, with one more set of data measured in parking garages. These measurements observed if and how the relationship between the two count rates changed as a result of these conditions. With those observations, a relationship between the two could be fully defined for later application to estimate the neutron background. These data were compared against simulations, which calculated the flux of cosmic ray particles for each location measured using the FLUKA Monte Carlo code [8,9]. In addition to the measured data, similar operational data were provided for analysis. These data were collected from more locations throughout the United States, but data were collected in a way that was not as controlled as measurements performed for this research. As a result, strong conclusions could not be drawn from the provided data, but the analysis served to confirm the measured data's results.

The relationship between the neutron and high energy scintillator count rates can then be applied to estimate the background neutron count rate during a mobile search. This would help indicate when neutron-emitting radiological material is being detected and produce an alarm. There would be an additional potential benefit of decreasing the amount of material that would accurately produce an alarm in these systems. To judge the effectiveness of applying such a relationship, additional mobile search measurements were performed with known neutron sources. These measurements indicated how well the estimated method improve current methods of producing alarms from the neutron detector.

1.3. Literature Review

Considering the objectives outlined of this research, it was important to look to previous work both for reasons why the correlation may occur and if similar background neutron estimation methods exist. Since cosmic rays are the main driver of background neutron production, research on secondary cosmic particles helped indicate which particles (if any) the NaI/PVT spectrometer may detect. That review indicated that the primary and many of the secondary cosmic ray particles had electric charge; therefore, previous work measuring NaI's and PVT's response to these particles was useful for determining useful energy calibrations. Finally, since the main goal was to estimate the neutron background, it was naturally important to review previous research attempting to do the same in various situations and where problems occurred.

1.3.1. Secondary Cosmic Rays at the Earth's Surface

Earth is constantly bombarded by a wide variety of particles that come from outer space. The presence of these cosmic rays was first discovered in 1912 while the study of particle physics was in its infancy [10]. Today, the composition of primary cosmic rays is well understood. Most (92-93%) of these particles are protons (Z=1) with a small amount (6%) of alpha particles (Z=2) and the remainder are nuclei with higher Z values [11,13]. The most likely kinetic energy of primary cosmic rays is 200 MeV nucleon^{-1} [11,13,14]. Above that, the probability decreases exponentially through 1000 GeV nucleon^{-1} [11,13,14,15].

These primary cosmic particles interact with the nitrogen and oxygen in the upper atmosphere, and the high energies involved causes a cascade of exotic particles starting with kaons and pions. A diagram of this cascade is shown in Figure 1-3, and Table 1-1 shows a description of the cascade particles and their decay modes. The table shows that most of these particles are short lived and would decay before reaching the Earth's surface. Many of these particles retain much of the kinetic energy of the primary particles, which means relativistic effects apply. For example, muons with 430 MeV of kinetic energy (530 MeV of total energy) would have a velocity approximately 98% of the speed of light (where the speed of light is $3 \cdot 10^8$ m s^{-1}). Table 1-1 shows that most particles' mean decay times are too short for this to be a significant effect. However, muons' mean decay time is long enough such that relativistic time dilation allows them to reach the Earth's surface in appreciable amounts before they decay. This can be observed in the muon flux spectrum compared to those of neutrons, protons, and pions shown in Figure 1-4.

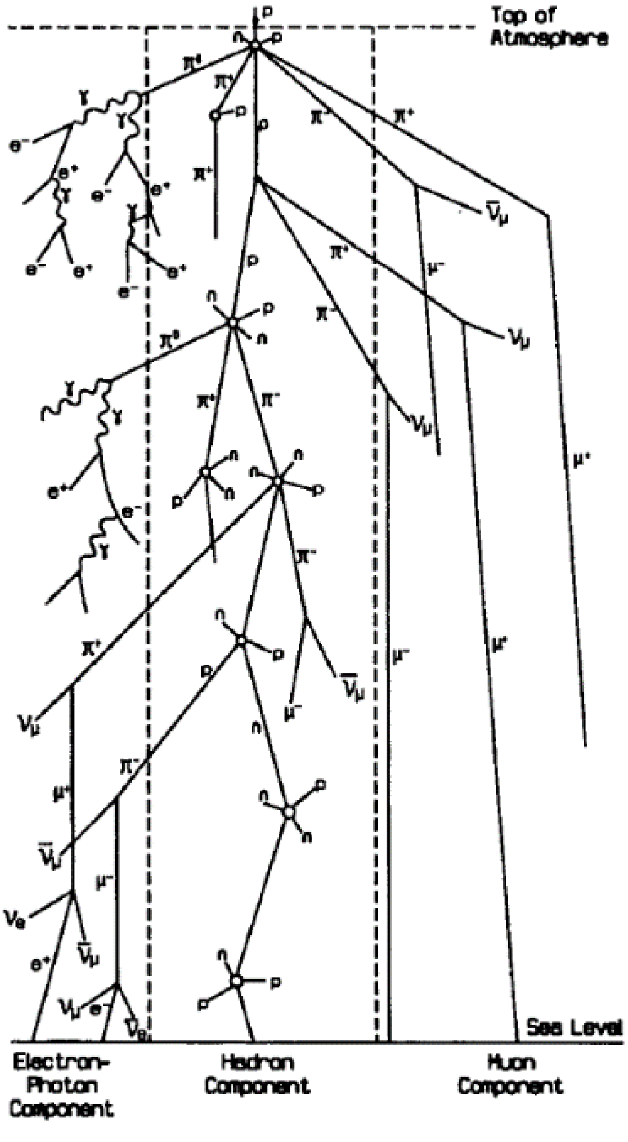

Figure 1-3. Diagram illustrating the cosmic ray cascades through the atmosphere (Reprinted from [12]).

Table 1-1. Rest mass, mean lifetime, and decay modes of mesons and leptons produced by primary and secondary cosmic ray interactions with nitrogen and oxygen atoms in Earth's atmosphere (Reprinted from [10]). Decays with branching ratios of less than 3% were ignored.

Particle	Rest Mass [MeV/c^2]	Mean Lifetime [s]	Decay Mode	Branching [%]
K_S^0	497.7(3)	$8.81(1) \times 10^{-11}$	$K^0 \to \pi^+ + \pi^-$	68.5(1.0)
			$K^0 \to \pi^0 + \pi^0$	31.5(1.0)
K_L^0		$5.77(59) \times 10^{-8}$	$K^0 \to \pi^\pm + e^\mp + \nu_e$	35.4(2.7)
			$K^0 \to \pi^\pm + \mu^\mp + \nu_\mu$	26.2(2.6)
			$K^0 \to \pi^0 + \pi^0 + \pi^0$	24.8(3.0)
			$K^0 \to \pi^+ + \pi^0 + \pi^-$	13.6(1.0)
K^+	493.78(17)	$1.229(8) \times 10^{-8}$	$K^+ \to \mu^+ + \nu_\mu$	63.2(4)
			$K^+ \to \pi^+ + \pi^0$	21.3(4)
			$K^+ \to \pi^+ + \pi^+ + \pi^-$	5.52(8)
			$K^+ \to \pi^0 + e^+ + \nu_e$	4.9(2)
K^-			$K^- \to \mu^- + \bar{\nu}_\mu$	63.2(4)
			$K^- \to \pi^- + \pi^0$	21.3(4)
			$K^- \to \pi^+ + \pi^- + \pi^-$	5.52(8)
			$K^- \to \pi^0 + e^- + \bar{\nu}_e$	4.9(2)
π^0	134.974(15)	$1.78(26) \times 10^{-16}$	$\pi^0 \to \gamma + \gamma$	98.823
π^+	139.580(15)	$2.551(26) \times 10^{-8}$	$\pi^+ \to \mu^+ + \nu_\mu$	99.9877
π^-			$\pi^- \to \mu^- + \bar{\nu}_\mu$	99.9877
μ^-	105.659(2)	$2.2001(8) \times 10^{-6}$	$\mu^- \to e^- + \bar{\nu}_e + \nu_\mu$	100
μ^+			$\mu^+ \to e^+ + \nu_e + \bar{\nu}_\mu$	100
$e^\pm$	0.511	Stable	--	--

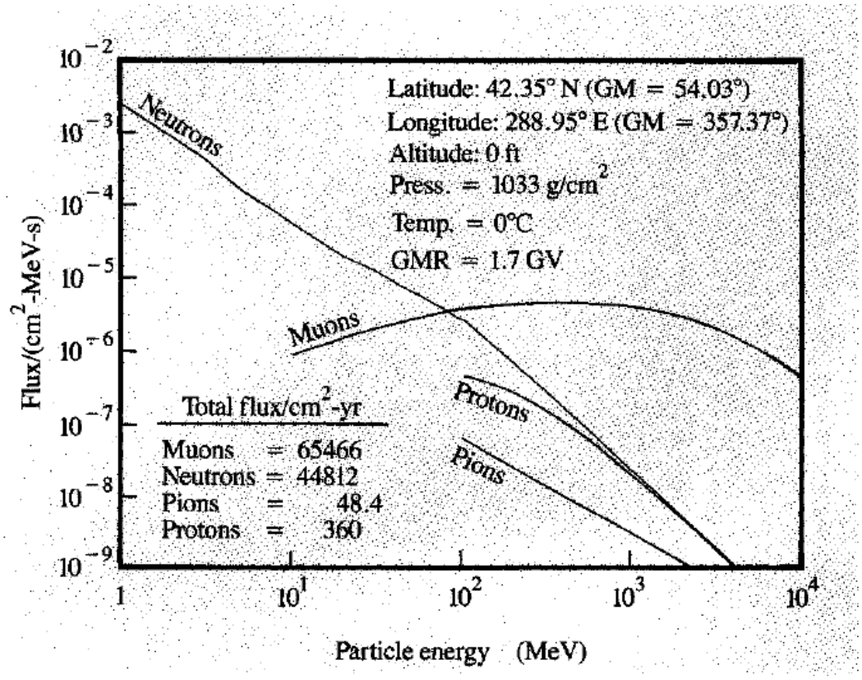

Figure 1-4. Energy dependent flux of various cosmic-ray particles (primary and secondary) in New York, New York (Reprinted from [11]).

Because these particles are produced in the upper atmosphere, the most significant effect on their flux is elevation or altitude. Literature shows that the secondary particle flux increases exponentially with decreasing atmospheric pressure (which correlates with altitude above the Earth's surface) but then decreases rapidly at very low atmospheric pressures (i.e. at very high altitudes) [11,12]. This rapid decrease in secondary cosmic particle flux is the result of decreasing primary cosmic ray interactions at very high altitudes. Two less significant effects on these fluxes are geomagnetic rigidity and solar modulation. The former refers to the strength of the Earth's magnetic field parallel to the Earth's surface, which is correlated with latitude and has a maximum near the equator [11,12,14]. The latter is correlated with solar activity. Active solar periods produce more solar wind which reduces the primary cosmic particles that reach earth, thus reducing the flux of secondary particles [11,12,14]. Of these effects, elevation is the most significant, with the highest flux (at extremely high altitudes) is 40 times that at sea level [12]. Geomagnetic rigidity is second with the maximum flux (near a magnetic pole) being 60% larger than the flux at the magnetic equator [12]. Solar activity is the least significant of these effects as an active solar period only reduces the flux by 20% compared to a quiet solar period [11].

1.3.2. Charged Particle Detection Using NaI and PVT

Much work exists studying scintillators' responses to various charged particles, particularly as charged particles are a significant part of the cosmic background. This research shows that sodium iodide (and similarly behaving cesium iodide) emit light when protons and heavier charged particles interact, which is an essential part of these scintillation systems. The light output increases linearly with proton energy and the relationship becomes increasingly non-linear with energy for increasing particle mass [16,17]. These relationships can be seen in Figure 1-5 for cesium iodide. A similar response has been shown to appear in plastic scintillators as shown in Figure 1-6 [18].

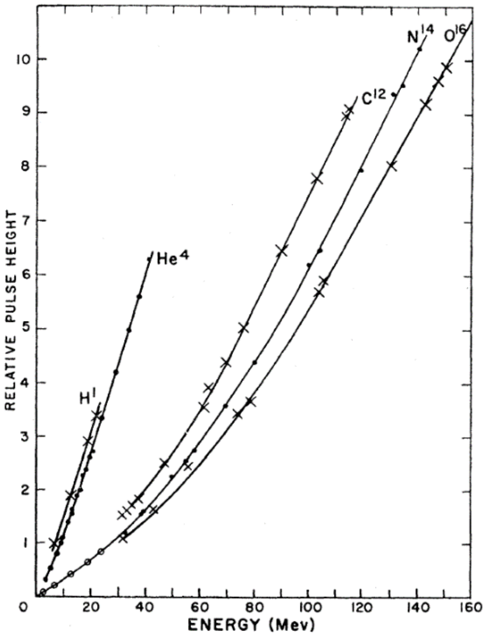

Figure 1-5. CsI pulse height as a function of charged particle energy (Reprinted from [17]).

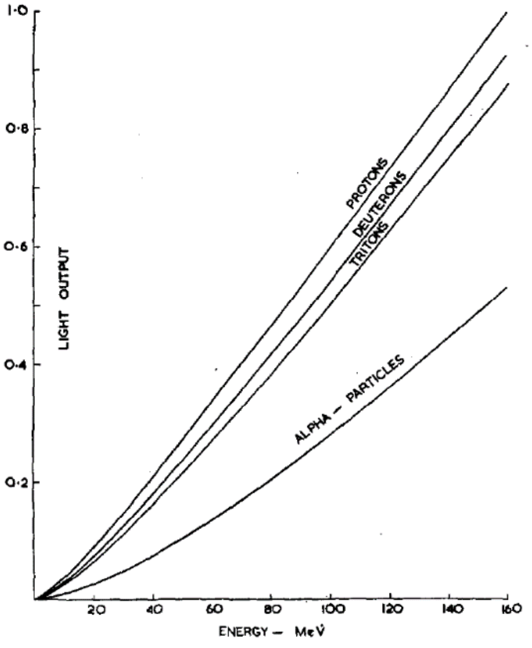

Figure 1-6. Light output from NE 102 plastic scintillator as a function of energy for different charged particles (Reprinted from [18]).

Similar efforts have measured the muon response in sodium iodide and plastic scintillator detectors. One measured the energy spectrum in a 4 inch diameter cylindrical sodium iodide detector. This was done by counting in coincidence with a proportional counter and produced the spectrum shown in Figure 1-7 [19]. Other work measured muons' directional spectrum using sodium iodide and plastic scintillators in coincidence [20]. While this work did not display the measured spectra for either detector type, it indicates that muons can be measured using both types of scintillator detector. Similarly, the only work that appeared which measured muons without coincidence methods was that of the CosmicWatch muon detector [21]. This detector counts muons using a small plastic scintillator, which indicates that similar techniques are possible in similar systems used to measure gamma rays.

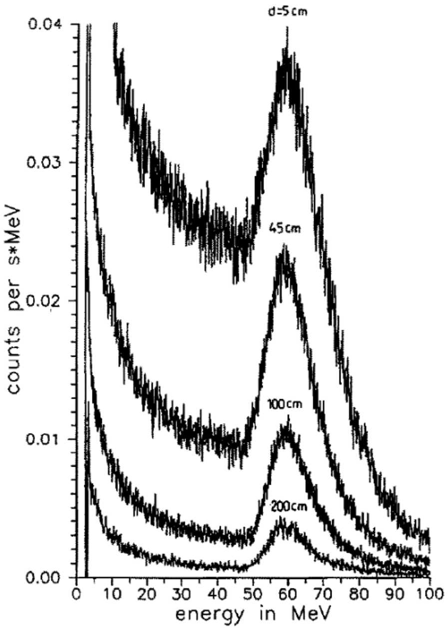

Figure 1-7. Energy spectrum of muons in a NaI detector in coincidence with a multiwire proportional counter with varying distance between them (Reprinted from [19]).

1.3.3. Neutron Background Rejection Methods

Methods to identify and reject background neutron counts have been researched before with little success. One noteworthy example was that done by the National Institute of Standards and Technology (NIST). The work sought to use coincidence measurements between neutrons and muons to identify and suppress neutron counts from background. Unfortunately, that work did not observe any significant neutron/muon coincidence. However, it did observe neutron/neutron coincidence, but not at sufficient levels to be practical [22]. Despite this result, the logic that was the basis of their work is important: that background neutrons and muons are produced by similar interactions. The reasoning for this should be clear when considering the previous section. As a result, similar logic will be applied for this research. The main difference is that the particles' fluxes (and therefore detectors' average count rates) will be considered proportional but not coincident. Cosmic ray interactions as shown in Figure 1-3 suggest this is true: while the same interactions eventually produce both particles, muons are produced indirectly (by pion decay) by the interactions that produce neutrons. It follows then that these two would not appear at the Earth's surface in coincidence.

1.4. References

1. "Beirut explosion: What we know so far." *BBC News*. 11 August 2020. Available at https://www.bbc.com/news/world-middle-east-53668493 (accessed 19 February 2021).
2. S.E. Rigby, T.J. Lodge, S. Alotaibi, et. al "Preliminary yield estimation of the 2020 Beirut explosion using video footage from social media." Shock Waves 30, 671-675

(2020). Available at https://doi.org/10.1007/s00193-020-00970-z (accessed 19 February 2021).

3. G. F. Knoll, *Radiation Detection and Measurement*, 4th Edition, John Wiley & Sons, 2010.
4. T. Ichimiya, T. Narita, K. Kitao, Natural background gamma-ray spectrum List of gamma-rays ordered in energy from natural radionuclides (JAERI-Data/Code--98-008), Japan Atomic Energy Research Institute, 1998. https://inis.iaea.org/collection/NCLCollectionStore/_Public/29/033/29033666.pdf.
5. T. McCullough, M. Kiser, and S. Bender. "NA-84 Measurements Campaign: Neutron Count Prediction Methodology for Search Applications." Remote Sensing Laboratory – Andrews. 27 April 2017.
6. Pickrell, Mark, et. al. "The IAEA Workshop on Requirements and Potential Technologies for Replacement of ^{3}He Detectors in IAEA Safeguards Applications." *Journal of the Institute of Nuclear Materials Management*, Vol 41 (March 2013). p. 14-29.
7. C.J. Werner, et al., "MCNP6.2 Release Notes", Los Alamos National Laboratory, report LA-UR-18-20808 (2018).
8. T.T. Böhlen, F. Cerutti, M.P.W. Chin, A. Fassò, A. Ferrari, P.G. Ortega, A. Mairani, P.R. Sala, G. Smirnov and V. Vlachoudis, "The FLUKA Code: Developments and Challenges for High Energy and Medical Applications" *Nuclear Data Sheets* 120, 211-214 (2014)

9. A. Ferrari, P.R. Sala, A. Fasso`, and J. Ranft, "FLUKA: a multi-particle transport code" CERN-2005-10 (2005), INFN/TC_05/11, SLAC-R-773
10. S. Hayakawa, *Cosmic Ray Physics – Nuclear and Astrophysical Aspects*, John Wiley & Sons, 1969.
11. J. F. Ziegler, “Terrestrial Cosmic Rays”, *IBM Journal of Research and Development,* 1996.
12. P. K. F. Grieder, *Cosmic Rays at Earth – Researcher’s Reference Manual and Data Book,* Elsevier, 2001.
13. C. Patrignani et al. (Particle Data Group), Chin. Phys. C, 40, 100001. 2017. Available at https://pdg.lbl.gov/2017/reviews/rpp2017-rev-cosmic-rays.pdf (Accessed 19 February 2021).
14. W. Heinrich, S. Roesler and H. Schraube. “Physics of Cosmic Radiation Fields.” *Radiation Protection Dosimetry*. Vol. 86, No. 4, pp 253-258 (1999).
15. T. Stanev. *High Energy Cosmic Rays*. 2nd Edition, Praxis Publishing Ltd. 2010.
16. C.J. Taylor, et. al. “Response of Some Scintillation Crystals to Charged Particles.” *Physical Review*. Vol. 84, No. 5 (1 December 1951). pp. 1034-1043.
17. A. R. Quinton, C. E. Anderson, and W. J. Knox. “Fluorescent Response of Cesium Iodide Crystals to Heavy Ions.” *Physical Review*. Vol. 115, No. 4 (15 August 1959). pp. 886-887.
18. T.J. Gooding and H.G. Pugh. “The Response of Plastic Scintillators to High-energy Particles” *Nuclear Instruments and Methods*. Vol. 7 (1960) pp. 189-192.

19. W. Preusse and S. Unterricker, “The contribution of cosmic ray muons to the background spectrum of gamma ray spectrometers.” *Nuclear Instruments and Methods in Physics Research* B. Vol. 94 (1994) pp. 569-574
20. C. Y. E. Ho, “Cosmic Ray Muon Detection Using NaI Detectors and Plastic Scintillators,” University of Virginia. Available at https://home.fnal.gov/~group/WORK/muonDetection.pdf accessed on September 7th, 2020).
21. S.N. Axani, J.M. Conrad, and C. Kirby. “The desktop muon detector: A simple, physics-motivated machine- and electronics-shop project for university students,” *American Journal of Physics* 85, 948 (2017).
22. C.R. Heimbach. “Cosmic Coincidences: Investigations for Neutron Background Suppression.” *Journal of Research of the National Institute of Standards and Technology* 112, 95-105 (2007).

2. PARKING GARAGE MEASUREMENTS INDICATING A GAMMA SPECTROMETER-NEUTRON COUNTER BACKGROUND CORRELATION*

2.1. Introduction

Radiological search operations typically employ gamma spectroscopy and gross neutron counting systems. These systems are often employed and analyzed independently, but operational data have indicated a possible relationship between the background count rates in both these detector systems. Specifically, the relationship appears to be between the background neutron count rate and the background count rate of signals greater than 3 MeV in the gamma spectrometer. This study sought to show this relationship using data collected with these systems from different floors of five parking garages. If a relationship exists for background measurements, it is possible that the background count rate in the gamma spectrometer could be used to predict the background count rate in the neutron counting system.

2.1.1. Background

Nuclear security operations commonly employ the simultaneous collection gamma spectra and neutron counts. This enables operators to find man-made radiological materials ranging from industrial and medical sources, which generally emit gamma-rays, to special nuclear materials, many of which emit both gamma and neutron radiation. Locating sources of gamma radiation is relatively simple because gamma rays have discrete energies which can be distinguished using a gamma spectrometer. Because of this, it is possible to quickly discern background gamma radiation from man-made sources [1].

---

*Reprinted with permission from "Parking Garage Measurements Indicating a Gamma Spectrometer-Neutron Counter Background Correlation" by Jackson N. Wagner, Craig Marianno, and Thomas McCullough in the *International Journal of Nuclear Security*, Vol. 6: No. 1, Article 6.

Conversely, locating sources of neutron radiation is more difficult because the detection systems typically only collect counts resulting from neutron interactions within the detection media. These interactions are most likely to occur when these neutral particles have very little kinetic energy (< 1 eV), but most neutrons - either background or emitted from a source - have energies greater than 1 MeV (with background neutrons often having energies over 100 MeV). Therefore, these detectors are often surrounded by materials that moderate neutrons to improve detection efficiency [1]. Despite this moderation, the background neutron count rate is typically very low and can vary with search environmental changes like elevation or surrounding building materials, particularly if the operation is a mobile search. The result is that the true background neutron count rate is difficult to identify in many situations.

A way to mitigate this issue is to estimate the expected background neutron count rate, which could be done based on the collected gamma ray spectrum. Gamma spectroscopy systems are often calibrated to a 3 MeV scale. With this calibration, gamma rays (or other particles) detected that have energies greater than 3 MeV are ignored. This is typical because the vast majority of gamma ray emitting radioisotopes emit gamma rays with energies less than 3 MeV [2]. While employing this scale for search operations, it is also possible to implement an “overflow” channel, which counts all the signals above 3 MeV. Analysis of data from operations with this feature indicated a possible relationship between the background count rates of the overflow channel and the neutron counter. The overflow channel count rate is unlikely to be the result of gamma rays since gamma rays from terrestrial sources rarely have energies above 3 MeV; therefore, these counts are likely a result of a different particle or a rare gamma ray of extraterrestrial origin. Measurements at various levels in a parking garage will illustrate this relationship between the background responses of these two systems at varying levels of intervening materials.

2.2. Materials and Methods

Parking garage measurements were collected using Ortec brand gamma spectroscopy and neutron counting systems (NAI-SS-4-P) [3]. Gamma spectroscopy was employed using one 4”-by-4”-by-16” (10.16 cm-by-10.16 cm-by-40.64 cm) NaI crystal with an Ortec digiBASE tube-base MCA [4]. This detector was calibrated to a 50 MeV scale by setting the bias voltage to 650V and the fine gain to 0.85x, which placed the ^{137}Cs 662 keV photopeak at channel 13 of 1024 channels (the first channel is identified as channel 0). The detector had a shaping time of 2 µs. Since the relationship of concern corresponds to high energy gamma signals, the lower-level discriminator was set to channel 81 such that signals below 4 MeV were ignored. The Ortec neutron counting system employed four 1”-by-18” (2.54 cm-by-45.72 cm) ^{3}He tubes pressurized to 3.039 bar (3 atm). The tubes were moderated by a layer of high-density polyethylene surrounding each with a minimum thickness of 1” (2.54 cm) [3]. Each ^{3}He tube had a Precision Data Technology (PDT) monitoring module to process the signals: three had a PDT10A-HN module and one had a PDT20A-HN module [5]. Data from these detectors were collected on a Windows-based computer via a USB connection to the digiBASE. The neutron counting system’s signal output was connected to the digiBASE via the digiBASE’s “enable” port, which allowed its signal to be collected via the digiBASE’s USB connection. The digiBASE system operated on USB power while the neutron counting system was powered by a 12 VDC car outlet. The connections for this system are outlined in the block diagram shown in Figure 2-1, and the detectors themselves are shown in Figure 2-2. Additional neutron counting measurements were collected using a Thermo brand backpack system (FHT 1377 PackEye) which has two 2”-by-15” (5.08 cm-by-38 cm) ^{3}He tubes pressurized to 2.5 bar (2.467 atm) and a 3.54”-by-4.72” (9 cm diameter-by-12 cm) plastic scintillator detector [6]. The data from this detector were collected via a Windows-based PDA system connected via Bluetooth. The PackEye system is shown in Figure 2-3, and both this and the Ortec systems were mounted in an SUV-type vehicle as shown in Figure 2-4.

This system was used to measure the background count rates at as many levels as possible (of the totals listed) within five different parking garages on the Texas A&M University campus:

1. University Center Garage (UCG) – 5 levels
2. Northside Garage (NSG) – 6 levels
3. Central Campus Garage (CCG) – 8 levels
4. West Campus Garage (WCG) – 7 levels (2 roof levels)
5. Cain Garage (CSS) – 5 levels

Since these are active public parking garages, measurements could not be collected in the exact same horizontal position on each floor, and measurements could not be collected on some floors due to the lack of availability or other instituted restrictions. Additionally, since all these garages were within the same general area of College Station, Texas, it was assumed that any differences in elevation would have a negligible effect on background count rates. Data on similar garages suggest that a standard garage floor is 10 inches (25.4 cm) thick, and it was assumed that all these garages followed this standard [7].

Measurements were collected for 15 to 20 minutes at each level of each parking garage in an effort to reduce the variance in the results, particularly in the unmoderated backpack neutron counting system. To reduce the overall time of the campaign, 15-minute measurements were collected on the roof and the first level below the roof since neutron count rates were higher at those locations, and 20-minute measurements were collected at all other levels. The variance was reduced further by applying a five second moving average to the data, which means a count rate at a given time is the average count rate over the previous five seconds (i.e. total counts over the last five seconds divided by five seconds). The Thermo FHT 1377 PackEye system did this automatically when recording its data, and the Ortec NAI-SS-4-P system recorded counts for each second, and the moving average was calculated in post-processing. Since these measurements follow Poisson processes, variances were calculated in relation to measurements’ total counts. Therefore, standard deviations, σ, presented with count rate data were estimated as $\frac{\sqrt{rt}}{t}$, where r represents a measurement’s overall count rate in s^{-1} and t is the measurement time.

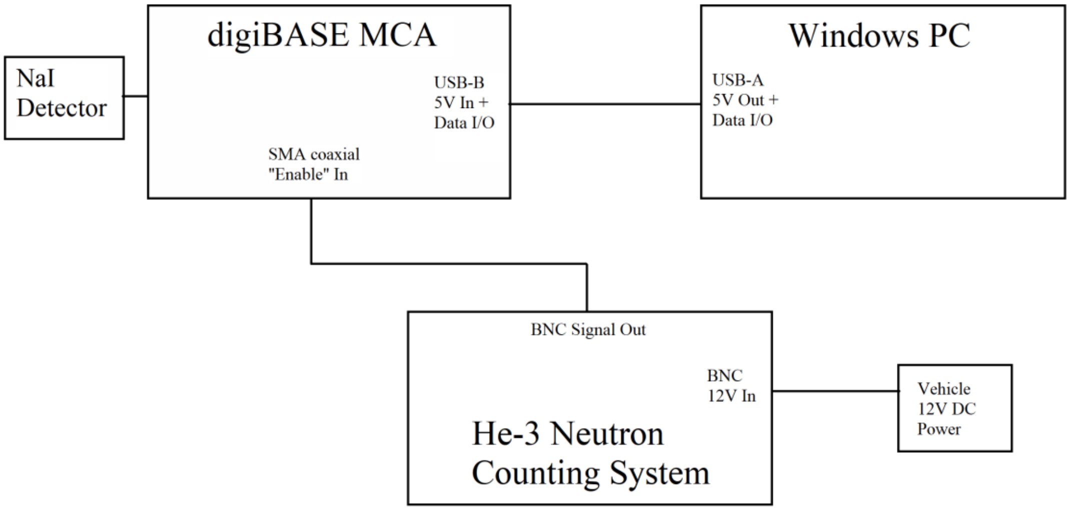

Figure 2-1. Block diagram outlining the connections when operating the Ortec NAI-SS-4-P system.

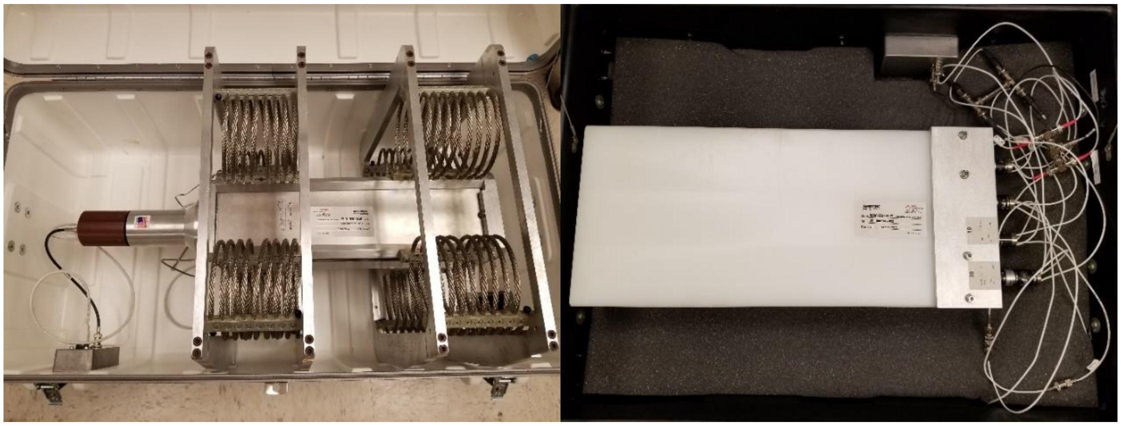

Figure 2-2. Photos of Ortec NAI-SS-4-P system in their ruggedized cases including the 4”-by-4”-by-16” NaI scintillation detector (left) and the four ^{3}He tubes in polyethylene moderator (right).

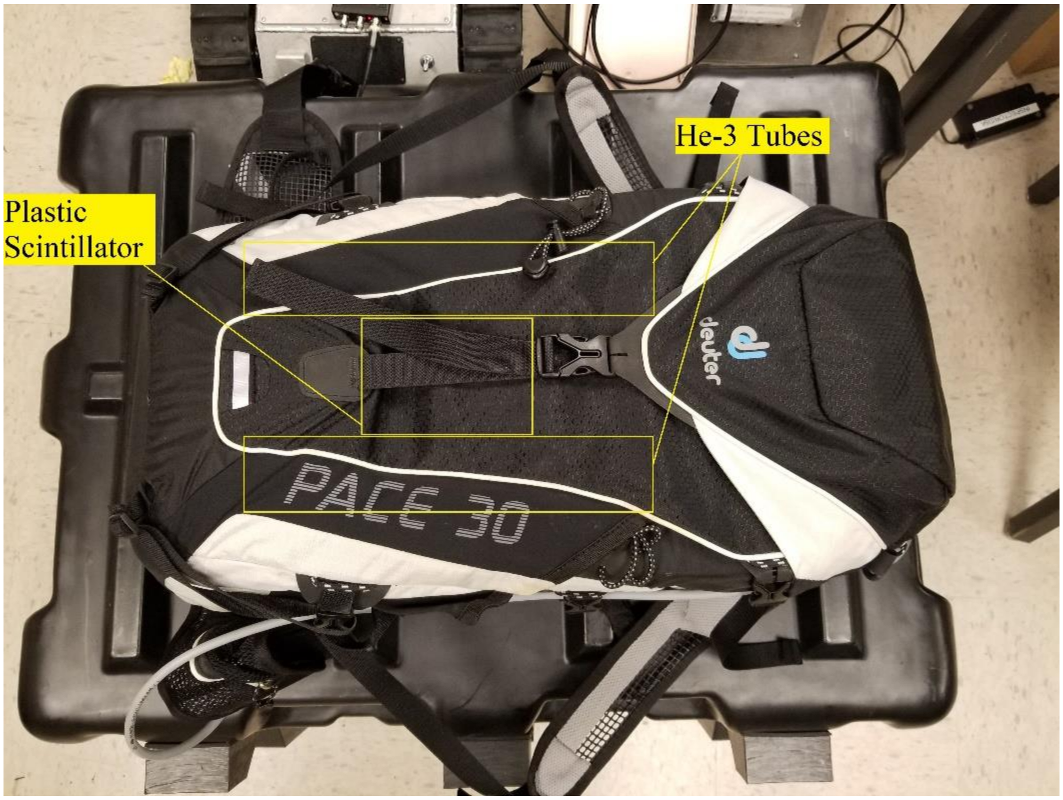

Figure 2-3. Diagram of Thermo FHT 1377 PackEye backpack detector system displaying the approximate positions of the plastic scintillator detector and the two ^{3}He tubes.

Figure 2-4. Photos displaying the detector systems' placements when mounted in an SUV-type vehicle for these measurements looking into the vehicle from the rear passenger side door (left) and the trunk (right).

2.3. Results and Analysis

The mean count rate of each detection system at each position was compared against the depth at which the detector was placed in the garage (i.e. the number of levels below the garage's roof) as shown in Figures 2-5, 2-6, and 2-7.

These plots show similar decreases in the count rate in both the Ortec gamma spectroscopy and neutron counting systems as the detectors move further below the roof of each garage. The plot shows that the relationship is linear with a constant slope up to a depth of at least four floors below the roof. An indicator of how well a linear equation fits the data is the R^2 value, which is a value between 0 and 1 where a model that fits all the data exactly has an R^2 value of 1. Linear fits on all the data produced R^2 values of 0.9119 and 0.8823, respectively, and linear fits excluding data below the fourth floor produced R^2 values of 0.9657 and 0.9045, respectively. A similar relationship appears in the Thermo neutron counting system with a key difference: the linear behavior occurs after an increase in the count rate between the roof and the first level down. This is a natural result of the unmoderated neutron counting system: the count rate increases in this way due to the moderation introduced by moving one level below the roof. A fit on these data (excluding the roof) produced an R^2 value of 0.8541. Similar to the Ortec systems, the plot suggests the slope decreases below a depth of five floors from the roof. There is less evidence to support the presence of this feature in all three systems as there were only two garages that allowed measurements below this depth; however, it suggests that an exponential relationship is also plausible. Exponential fits on these data had R^2 values of 0.9491, 0.9154, and 0.9319 for the Ortec gamma, Ortec neutron, and Thermo neutron detectors, respectively.

Because of the apparent relationships between the count rates and depth, it is meaningful to compare the mean neutron count rate against the mean gamma spectrometer count rate as shown in Figures 2-8 and 2-9 for two garages.

Figures 8 and 9 illustrate the linear relationship between the neutron count rate and the NaI count rate between 4 MeV and 50 MeV for both neutron detection systems in the Central Campus and University Center Garages (CCG and UCG). Similar trends appeared in the data collected within the other three garages. The larger values occurred at the roof and higher floors because there was little to no concrete to moderate and shield the particles registered in the higher gamma energy channels. The smaller values occurred at the deepest floors in each garage (greater than 4 floors below the roof) because there was significant amount of intervening concrete. The only significant deviation from a linear relationship appears in the relationship involving the mean Thermo PackEye neutron count rate, and that only occurs when the detectors were on the roof as noted previously. Linear regressions on these data produced equations of the neutron count rate as functions of the 4 MeV to 50 MeV NaI count rate shown in Eq. 2-1 and Eq. 2-2. The regression on the data from the Thermo system ignored the data collected from the roofs of the parking garages. These regressions had R^2 values of 0.955 and 0.929, respectively.

$$n_{Ortec} = 0.0245\, g - 0.09633 \tag{2-1}$$

$$n_{Thermo} = 0.0689\, g - 0.2621 \tag{2-2}$$

Where:

n_{Ortec} = mean count rate of the Ortec neutron counting system [s^{-1}]

n_{Thermo} = mean count rate of the Thermo PackEye neutron counting system [s^{-1}]

g = mean count rate of Ortec NaI system between 4 MeV and 50 MeV [s^{-1}]

There are two notable features of these models. First, the intercepts are not zero as initially expected. The models suggest that the mean NaI (4-50 MeV) count rates would be approximately 3.93 s^{-1} and 3.80 s^{-1} when the mean neutron count rate in the Ortec and Thermo neutron detectors reach zero, respectively. The second feature is that the slope varies for the different systems. The slope of the fit for the Thermo neutron system was nearly three times larger than that for the Ortec neutron system.

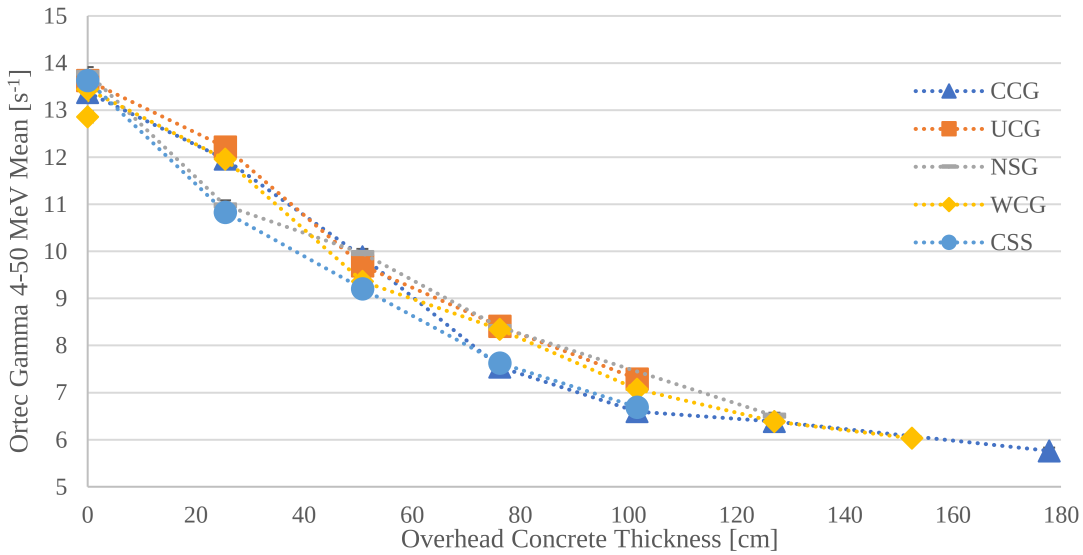

Figure 2-5. The mean Ortec NaI count rate (between 4 MeV and 50 MeV) at each location in each parking garage plotted as a function of concrete thickness above the detector. The data were collected continuously over 15-20 minutes and had a five second rolling average applied before calculating the mean. 1-σ error bars are shown, but some of them may be obscured by the data markers.

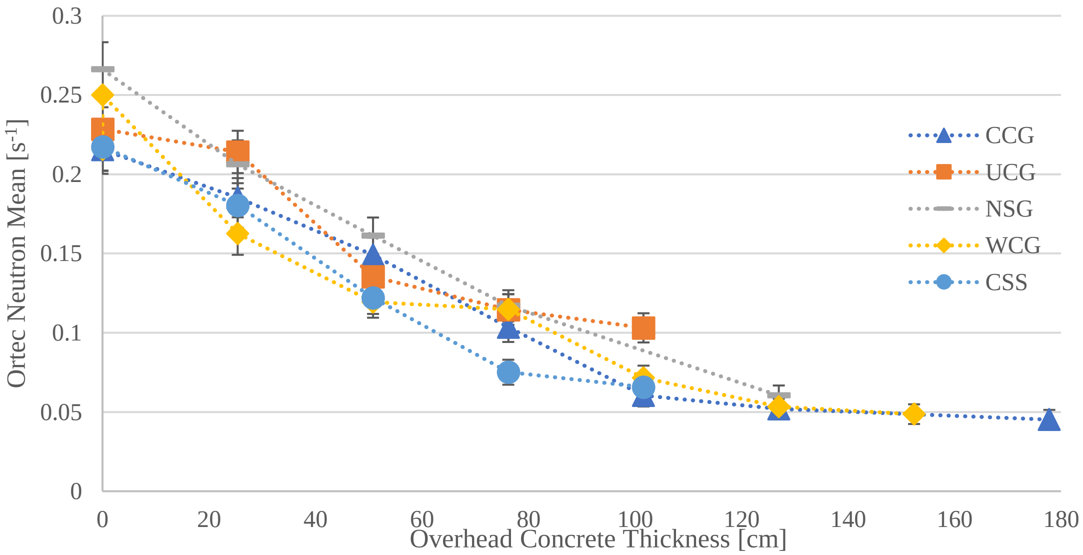

Figure 2-6. The mean Ortec neutron count rate at each location in each parking garage plotted as a function of concrete thickness above the detector system. The data were collected continuously over 15-20 minutes and had a five second rolling average applied before calculating the mean. 1-σ error bars are shown, but some of them may be obscured by the data markers.

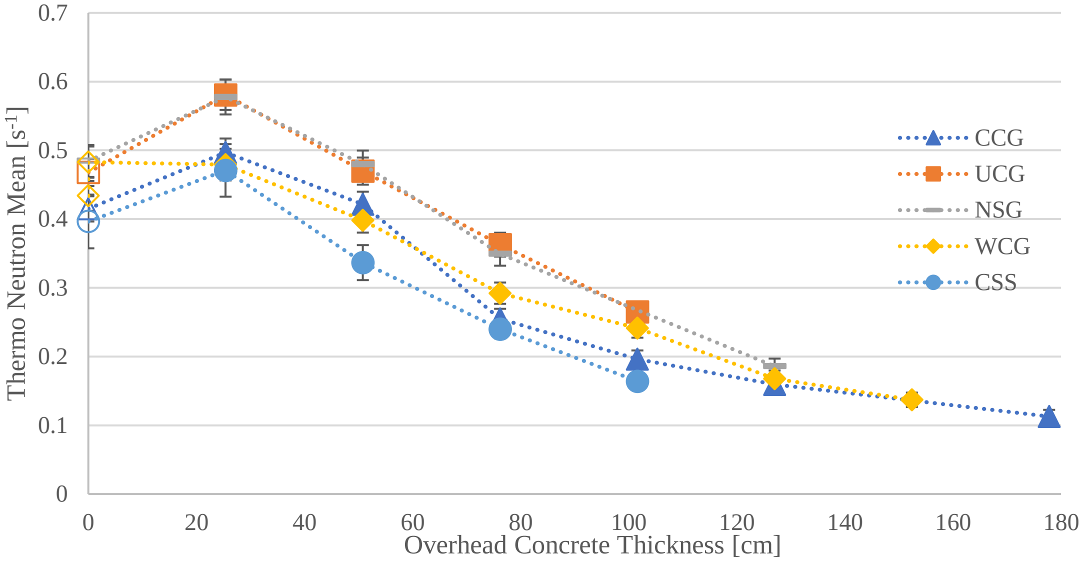

Figure 2-7. The mean Thermo PackEye neutron count rate at each location in each parking garage plotted as a function of concrete thickness above the detector system. The data were collected continuously over 15-20 minutes and had a five second rolling average applied before calculating the mean. 1-σ error bars are shown, but some of them may be obscured by the data markers.

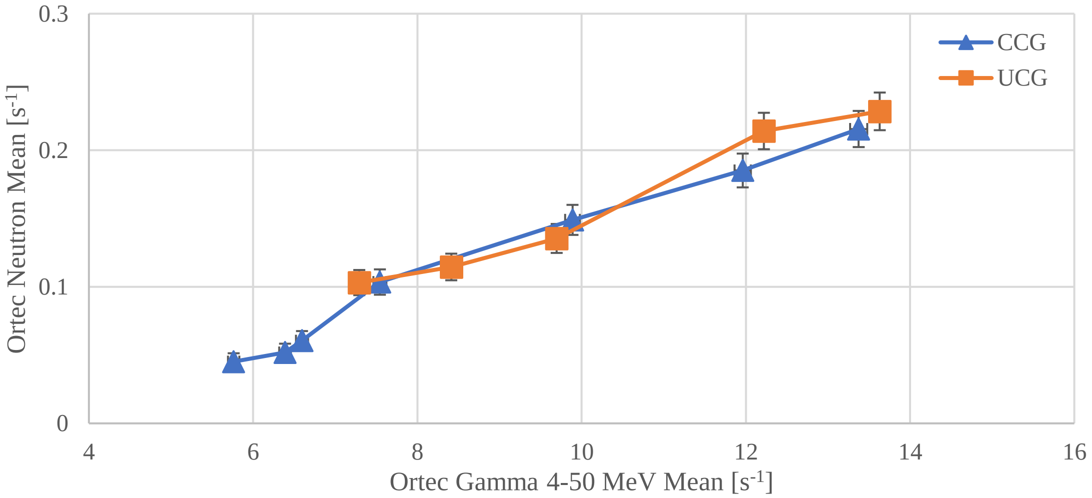

Figure 2-8. The mean Ortec neutron count rate as a function of the mean Ortec NaI count rate (between 4 MeV and 50 MeV) at each location in the Central Campus and University Center Garages (CCG and UCG). The data were collected continuously over 15-20 minutes and had a five second rolling average applied before calculating the mean. 1-σ error bars are shown, but some of them may be obscured by the data markers.

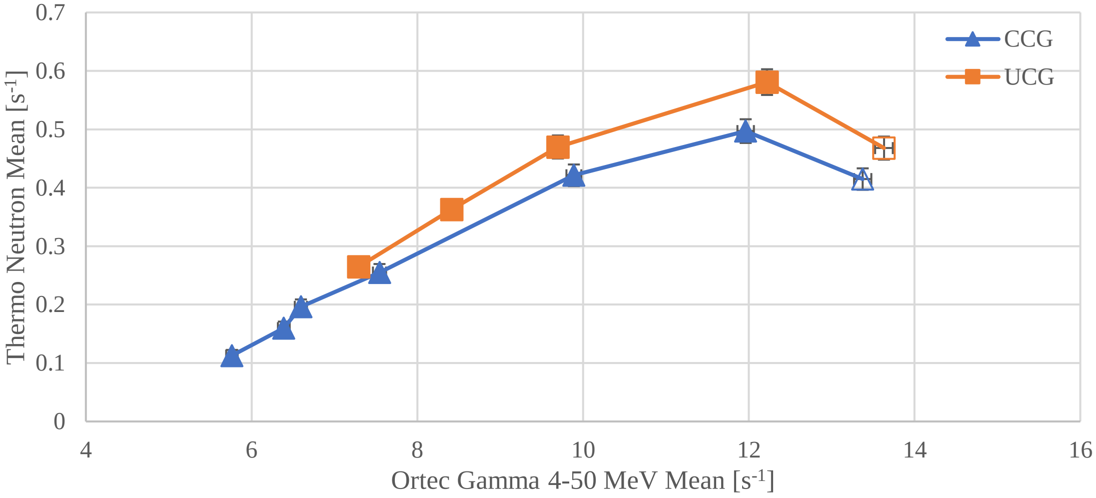

Figure 2-9. The mean Thermo PackEye neutron count rate as a function of the mean Ortec NaI count rate (between 4 MeV and 50 MeV) at each location in the Central Campus and University Center Garages (CCG and UCG). The data were collected continuously over 15-20 minutes and had a five second rolling average applied before calculating the mean. Data collected from the roof of a garage are denoted by the unfilled points. 1-σ error bars are shown, but some of them may be obscured by the data markers.

There are three theories that would explain the cause of the high energy signal in the NaI detector:

1. High energy cosmic gamma rays
2. Cosmic muons
3. Protons from the decay of background neutrons (free neutron half-life is ~11 minutes)

All these theories are based around interactions of cosmic rays in the upper atmosphere, which produce all of these particles and the majority of the background neutrons that the ^{3}He systems count. Extraterrestrial cosmic rays interact with the upper atmosphere and create showers of various particles, including neutrons, muons, and gamma rays (among others). These theories assume the particles produced by these showers are produced in similar amounts (i.e. the production rate of each particle follows a normal distribution with a different mean)

For theory 1, gamma rays produced by cosmic rays appear on a wide spectrum, which would not produce a peak in the NaI spectrometer on the 4 MeV to 50 MeV range. Additionally, the NaI count rate versus depth relationship could be considered as exponential rather than linear, which is the usual behavior gamma ray attenuation. If that were the case, the data suggest that the half value layer of concrete was approximately 50” (127 cm - assuming each level of each garage was 10” thick) [7]. However, NIST reports the mass attenuation coefficient of 20 MeV gamma rays as 0.01539 cm^2 g^{-1} that remains relatively constant as the energy increases [8]. This results in a half value layer of 19.6 cm, but the half value layer suggested by the data is approximately 6.5 times larger. While an exponential relationship may explain the decrease in slope of the NaI count rate versus depth data, this discrepancy cannot be overlooked without additional research.

Theories 2 and 3 are similar to each other. The muons and protons that would reach the detector would likely have energies much greater than 100 MeV. These particles would then deposit energy in the NaI detector proportional to the particle’s energy and the path length it travels in the detector, which would frequently produce signals in the 4 MeV to 50 MeV range. Both particles would also have the energy to penetrate the concrete shielding seen in this study. The range of an average energy background muon (4 GeV) in concrete is approximately 13 km, and the range of a proton produced by the decay of an average energy neutron (100 MeV) in concrete is approximately 58.3 cm [9,10]. The former means that muons would only see linear energy loss with each layer of concrete they penetrate. The latter would suggest that protons from neutron decay outside the garage would not penetrate the third level of the garages; however, it is plausible for neutrons to decay after penetrating multiple levels in the garage and be detected.

2.4. Conclusion

This research indicates a correlation between the background high energy count rate of an NaI scintillator (between 4 MeV and 50 MeV) and the background count rate of a neutron counting system, which appeared to be linear as a function of the amount of intervening moderating material. The results of this work also suggest that that the background high energy count rate of the NaI scintillator is likely the result of particles that are different from common background gamma rays.

Additional work will be required to test the suggested theories regarding the cause of the relationship. If one or more of these theories are true, it would indicate the cause of the linear relationship shown: the background NaI 4-50 MeV count rate would be proportional to the background neutron count rate because the particles being detected are produced proportionally by cosmic ray interactions with the upper atmosphere. The result would be the ability to use these or more robust versions of the linear models shown to infer the true background neutron count rate using the high energy NaI count rate. Future research could produce algorithms to distinguish neutron "background" count rates from man-made neutron sources. This improvement would make search operations more efficient by reducing the need to investigate nuisance neutron alarms.

2.5. References

1. G. F. Knoll, *Radiation Detection and Measurement*, 4th Edition, John Wiley & Sons, 2010.
2. T. Ichimiya, T. Narita, K. Kitao, Natural background gamma-ray spectrum List of gamma-rays ordered in energy from natural radionuclides (JAERI-Data/Code--98-008), Japan Atomic Energy Research Institute, 1998. https://inis.iaea.org/collection/NCLCollectionStore/_Public/29/033/29033666.pdf.
3. D. L. Upp, R. M. Keyser, Performance of a car-mounted neutron and gamma-ray monitoring system for illicit material detection, in: Proc. 45th INMM Annual Meeting Institute of Nuclear Materials Management, 2004.
4. AMETEK Inc. – ORTEC, digiBASE 14-Pin PNT Tube Base with Integrated Bias Supply, Preamplifier, and MCA (with Digital Signal Processing) for NaI Spectroscopy, available at https://www.ortec-online.com/-/media/ametekortec/brochures/digibase.pdf (accessed on December 29th, 2018).
5. Precision Data Technology Inc., Data Sheet: PDT10 & 20 Series, available at http://www.pdt-inc.com/products/10series/10series_datasheet.htm (accessed on December 29th, 2018).
6. Thermo Fisher Scientific Inc., FHT 1377 PackEye – Radiation Detection Backpack, available at https://static.thermoscientific.com/images/D19393~.pdf (accessed on

December 29th 2018).

7. F. Barth, et. al, Cast-In-Place Concrete Parking Structures, available at http://www.crsi.org/pdf/ParkingStructures.pdf (accessed on December 29th 2018).
8. J. H. Hubbell, S. M. Seltzer, Tables of x-ray mass attenuation coefficients and mass energy-absorption coefficients 1 keV to 20 MeV for elements z=1 to 92 and 48 additional substances of domestic interest, National Institute of Standards and Technology (NIST) Data, 1995. https://physics.nist.gov/PhysRefData/XrayMassCoef/tab4.html.
9. D. E. Groom, N. V. Mokhov, S. I. Striganov, Muon Stopping Power and Range Tables 10 MeV – 100 TeV, Atomic Data and Nuclear Data Tables, 78-2 (2001) 183-356.
10. M.J. Berger, Stopping-Power and Range Tables for Electrons, Protons, and He: estar, astar and pstar National Institute of Standards and Technology (NIST) Data, http://physics.nist.gov/PhysRefData/Star/Text/contents.html.

3. IDENTIFICATION OF THE AMBIENT RESPONSE RELATIONSHIP IN NEUTRON COUNTING AND SCINTILLATION MEASUREMENT SYSTEMS*

3.1. Introduction

The threat of nuclear terrorism is a concern for many nations. A nuclear terrorist attack would most likely occur at a public event and would use a radiological dispersal device (RDD – commonly known as a “dirty bomb”) or an improvised nuclear device (IND). A common tool for securing these events is the mobile search system. This employs gamma spectroscopy and neutron counting techniques during a large-area search to locate radioactive material.

To efficiently locate sources of radiation, the mobile search system detectors must have well understood ambient (or “background”) responses. This is simple for a gamma spectroscopy system as the background has a spectrum that is unique from any illicit gamma ray-emitting material [1, 2]. The system also has the benefit that the source of most background gamma rays is the Earth, which produces little variance in the overall count rate during a mobile search. However, the background response in a neutron counting system is much more difficult to characterize because the user is only provided a count rate. This is compounded by the fact that the main source of background neutrons is secondary cosmic ray interactions in the Earth’s upper atmosphere (mainly through spallation processes) [3]. This and the physics of neutron interactions means the neutron count rate can vary with elevation changes along with the presence and composition of

---

*Reprinted with permission from “Identification of the Ambient Response Relationship in Neutron Counting and Scintillation Measurement Systems” by Jackson N. Wagner and Craig Marianno in *Radiation Science and Technology*, Vol. 7, No. 1.

surrounding buildings or material. This makes it more difficult to determine if a change in neutron count rate is due to one of these background changes or from an illicit source.

Previous work has suggested that employing a different data stream from the gamma spectrometer has the potential to improve the neutron background’s characterization during mobile searches. Specifically, that the background count rate of high energy signals in the gamma spectrometer (greater than 3 MeV) is correlated with the background neutron count rate. This was initially indicated by operational data, and its presence has been shown with varying concrete shielding from parking garages [4]. In a continuing effort to explain and generalize this correlation, this work sought to explain the cause of these high energy signals.

3.2. Materials and Methods

To determine the source of high energy signals produced in gamma spectrometers, spectra from long background measurements were compared to simulations of candidate particles interacting with the same detectors. Measurements were performed with spectrometers commonly used during mobile searches: sodium iodide (NaI) and polyvinyl toluene (PVT) scintillator detectors. The NaI detector had dimensions of 2”-by-4”-by-16” (5.08 cm-by-10.16 cm-by-40.64 cm) and was manufactured by Alpha Spectra Inc. (model #: 8D16X64A5/3.5), and the PVT detector had dimensions of 2.5”-by-6.5”-by-24.5” (6.35 cm-by-16.51 cm-by-62.23 cm) and was manufactured by Alpha Spectra Inc. (model #: P8l24X96/2) [5,6,7].

Signals from these detectors were collected using an Ortec digiBASE. This multi-channel analyzer (MCA) was set to 1024 channels and was calibrated so particles over 10 MeV could be registered [8]. The scale of the NaI spectrum was calibrated to approximately 70 MeV using the photopeaks from ^{137}Cs and ^{22}Na, while the PVT scale was set to approximately 85 MeV using the Compton Edge energies for the 662 keV photon from ^{137}Cs and the 1274 keV photon from ^{22}Na. The spectral features aligning with the respective channels are shown in Table 1. The detectors were connected to a computer running Ortec's MAESTRO software for Windows as shown in the block diagram in Figure 1 [9]. To minimize the variance in the measured spectra, data were collected using this system for 36 hours for each measurement scenario.

Table 3-1. Calibration information for NaI and PVT detectors.

	Isotope			^{137}Cs	^{22}Na	
	Gamma Ray Energy		[keV]	662	511	1274
NaI	Photopeak	Energy	[keV]	662	511	1274
		Channel Number		10.5 ± 1	8 ± 1	19.5 ± 1
	digiBASE Voltage		[V]	500		
	Calibration		[keV ch^{-1}]	68.0 ± 10.7		
PVT	Compton Edge	Energy	[keV]	477.65	-	1061.18
		Channel Number		8 ± 1	-	15 ± 1
	digiBASE Voltage		[V]	720		
	Calibration		[keV ch^{-1}]	83.3 ± 16.8		

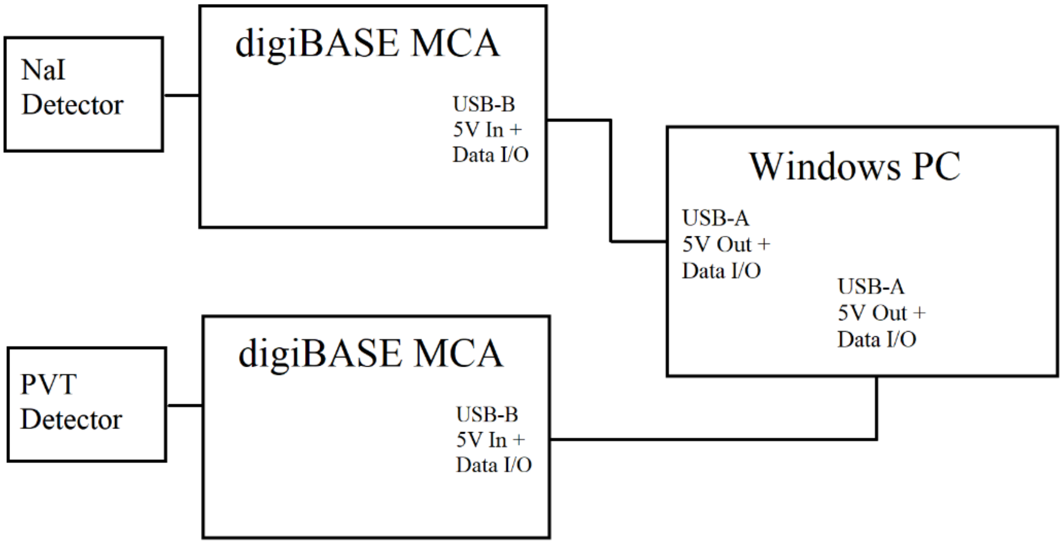

Figure 3-1. Block diagram of connections of detectors to computer for all measurements.

The potential particles of interest in these detectors as calibrated are high energy gamma rays, protons, and muons (negatively charged particles 200 times more massive than electrons). All three of these particles are the result of secondary cosmic ray interactions in the atmosphere. In addition to the gamma rays, the protons and muons interact with the NaI and PVT detectors [1]. Research has shown that these detectors have a linear response as a function of energy for protons and an increasingly non-linear response as particle mass increases [10,11]. Previous measurements have also shown that muons produce a peak (or mode) in a scintillator’s spectrum at energy scales similar to those described above. However, these experiments were performed using coincidence measurements and mainly for laboratory applications [12].

Considering the literature more broadly suggests that the muons are the most likely candidate of these three particles. Previous work has shown that the proton flux at the Earth's surface is two orders of magnitude smaller than that of muons [13]. Published research on the photon component of cosmic rays at the Earth's surface suggests their flux is negligible compared to muons [3,14]. The low flux for protons and gamma rays (relative to muons) would make it difficult to distinguish their respective spectral features from those of muons. Additionally, the lack of literature on the characteristics of high-energy gamma rays near Earth's surface would make their simulation difficult because of the inability to accurately model the particles' source [3,14].

As stated above, these muons are the product of cosmic ray interactions. The primary cosmic rays are mainly comprised of protons from outer space with energies much greater than 1 GeV. When these particles interact with the nitrogen and oxygen atoms of the atmosphere, strong nuclear processes produce a shower of exotic particles, initially comprised of short-lived kaons and pions (mean lifetimes: 12-50 ns). These eventually decay into muons, and many have enough kinetic energy to reach the Earth's surface before decaying (mean lifetime: 2.2 μs) [3].

Since the muons are charged particles, detector orientation was an important parameter for this research. Energy deposition of the charged particle depends on its path length through the detector, and these cosmic muons have a mostly downward trajectory as indicated in Figure 2. This figure illustrates that 40% of cosmic muons have an angle of incidence less than 20 degrees from the vertical axis and 90% have an angle less than 62 degrees [15]. This characteristic would likely produce variance in the measured spectra with different detector orientations, particularly because changing the detector geometry relative to the vertical axis will change the distribution of possible muon paths, thus changing the energy spectrum. Three separate detector orientations were used to collect data. For the purposes of this analysis, the orientations are referred as “Vertical,” where the smallest detector face was parallel to the ground; “Horizontal, Short Side Up,” where the second largest detector face was parallel; and “Horizontal, Long Side Up,” where the largest detector face was parallel. These orientations are illustrated in Figure 3.

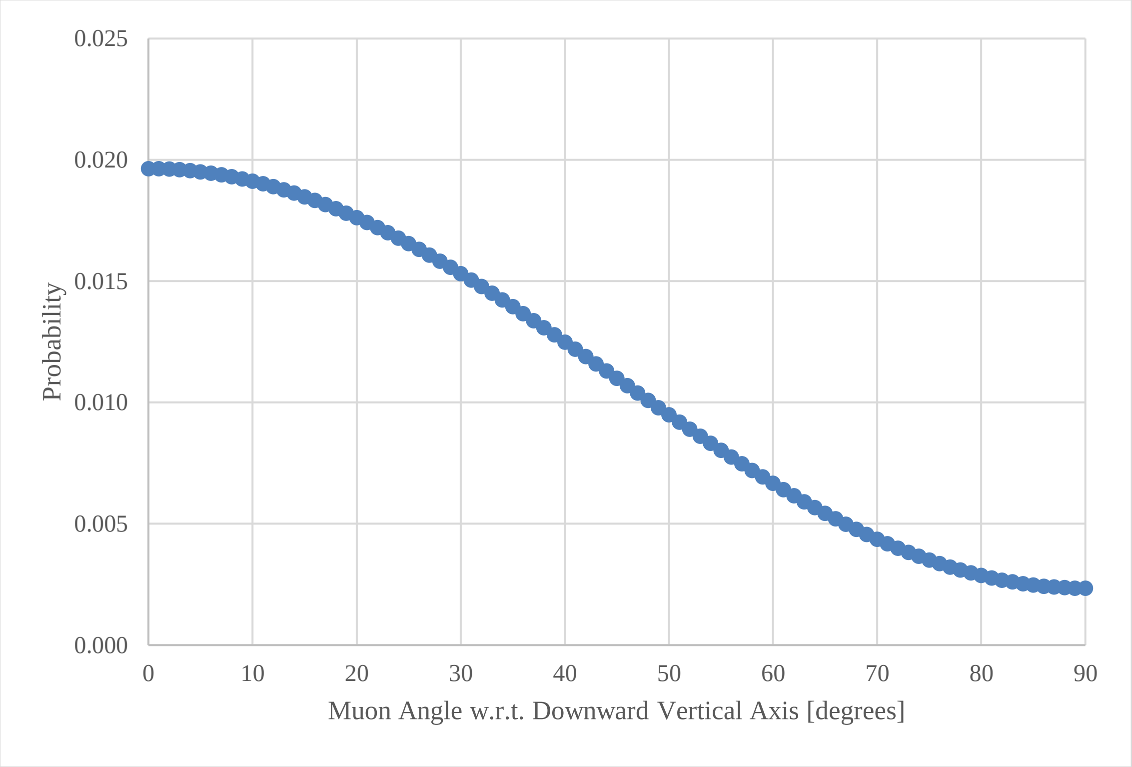

Figure 3-2. Muon direction probability density function (Reprinted from [15]).

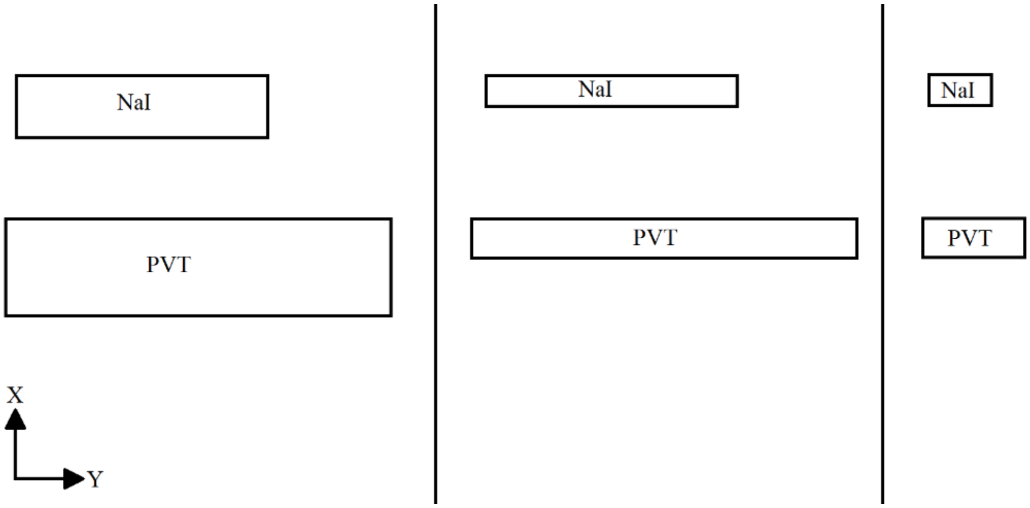

Figure 3-3. Diagrams showing the top-down views of the NaI and PVT detectors for the orientations used, which are named “Horizontal, Long Side Up” (left), and “Horizontal, Short Side Up” (center), and “Vertical” (right).

Because these particles interact with the detectors differently than gamma rays, the measured spectra required a slightly different terminology for analysis than gamma ray spectra. Specifically, analysis of the spectra looked for global and local modes in a statistical sense (i.e. the most frequent value of a spectrum or a subsection of it). This is similar to that for a gamma ray spectrum, but those modes are referred as “photopeaks” (or simply “peaks”) because they correlate with gamma rays undergoing a photoelectric process within the detector. Since muons and protons cannot undergo a photoelectric process, it would be incorrect to refer to statistical modes of a spectrum as “peaks.” Therefore, analysis of measured and calculated spectra will refer to the modal data.

If the particles are muons, an approximation of the expected energy spectrum can be calculated for each detector in each orientation. This was done by calculating the distribution of potential path lengths through the detector using a Python script. For all possible muon entry points on the detector's surface, this script calculated the possible path lengths a muon could travel from that entry point through the detector for all possible directions. These directions fell on cones whose half angles were governed by the distribution of angles with the vertical axis shown in Figure 2. This script had a 2 mm resolution of entry locations, and a 1 degree resolution of both polar angles for direction, where these resolutions were limited by available computer memory. The energy spectrum was approximated by multiplying these path lengths by a muon's minimum linear energy deposition. This value is 4.785 MeV cm^{-1} for NaI and 2.019 MeV cm^{-1} for PVT. The actual linear energy deposition does depend on energy, but the minimum values for each material appear near the mean energy of a background muon, which is 4 GeV on a log-normal distribution [15,16]. These energies were then collected in 50 keV bins to produce an energy spectrum to be compared against measured data. A full listing of the Python script used to generate these energy spectra can be found in Appendix A.

To confirm that the particles measured are muons, the recorded spectra were also compared against MCNP simulation results [17]. These computer models simulated the muon's response in the two scintillators in the orientations used in the physical measurements. The cosmic muon source was modeled with a direction-biased spectrum derived from cited measurements as shown in Figure 2. The muon's energy spectrum was modeled as a log-normal distribution with a mean of 4 GeV and standard deviation of 220 GeV, where the latter was selected to match the shape of the spectrum in literature as shown in Figure 4 [15]. The simulation used a disk for the muon source placed 10 m above a simplified detector geometry. Biasing was applied to source the muons' direction as a function of radius to improve the speed of the simulation's convergence. In addition, the F8 tally had a Gaussian energy broadening modifier to simulate the detector's energy variance.

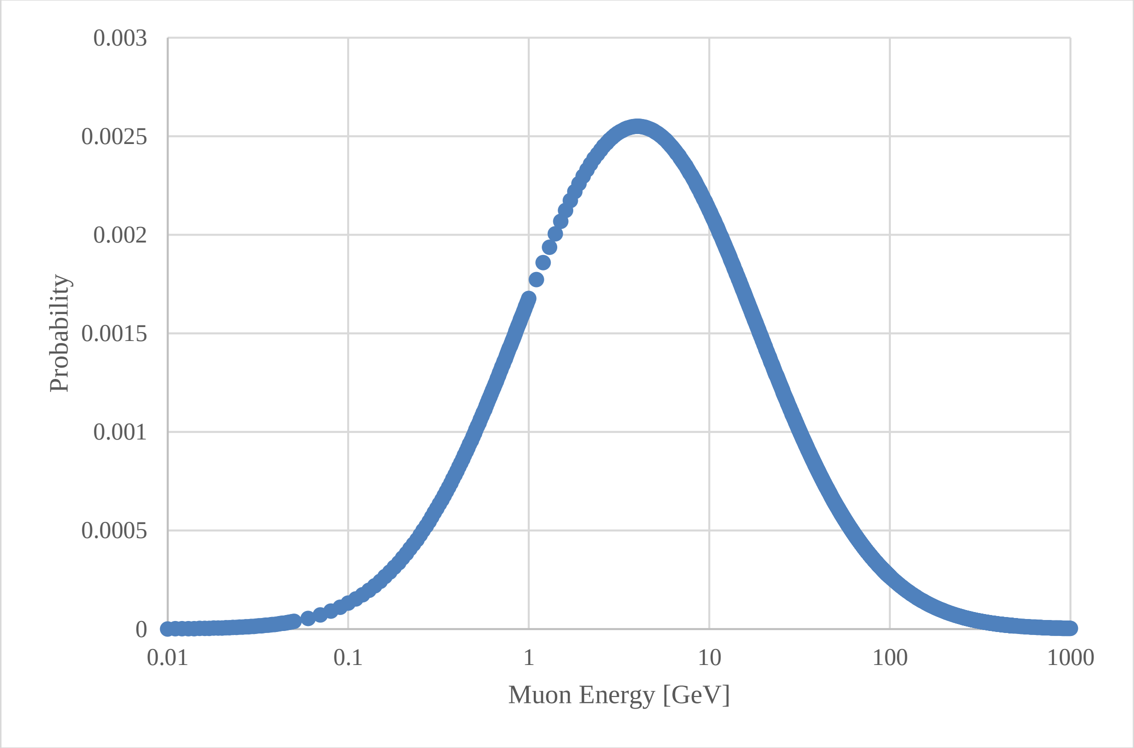

Figure 3-4. Muon probability as a function of energy for MCNP model, modeled as a log-normal distribution with a mean of 4 GeV and a standard deviation of 220 GeV (Reprinted from [15]).

3.3. Results and Discussion

The measurements described above produced the spectra shown in Figure 5 for NaI and those for PVT are shown in Figure 6. These spectra show distinct modes that vary with the orientation of the detector. Data about these modes are shown in Table 2. In NaI, modes appeared at 25.5 ± 4.0 MeV in the Horizontal-Long Side Up orientation, at 28.9 ± 4.5 MeV and 48.0 ± 7.5 MeV in the Horizontal-Short Side Up orientation, and at 27.1 ± 4.3 MeV in the Vertical orientation. The count rates of all signals above 8.0 MeV were 8.50 ± 0.01 s^{-1}, 6.51 ± 0.01 s^{-1}, and 4.94 ± 0.01 s^{-1}, respectively. In PVT, modes appeared at 9.6 ± 1.9 MeV in the Horizontal-Long Side Up orientation, at 11.8 ± 2.4 MeV and 26.1 ± 5.3 MeV in the Horizontal-Short Side Up orientation, and at 11.3 ± 2.3 MeV in the Vertical orientation. The count rates of all signals above 4.8 MeV were 15.69 ± 0.01 s^{-1}, 10.88 ± 0.01 s^{-1}, and 10.02 ± 0.01 s^{-1}, respectively.

Table 3-2. Modal data for NaI and PVT measurements by orientation including modes' full-widths at half-maximum (FWHMs), when its calculation was possible. Missing data for "Mode 2" indicates that only one mode existed for a given measurement.

		Detector	NaI			PVT		
		Orientation	Horizontal, Long Side Up	Horizontal, Short Side Up	Vertical	Horizontal, Long Side Up	Horizontal, Short Side Up	Vertical
Measurement Time		[s]	129600	129600	129600	129600	129600	129600
Net Count Rate		[s^{-1}]	8.495	6.514	4.940	15.687	10.878	10.016
σ		[s^{-1}]	0.008	0.007	0.006	0.011	0.009	0.009
Mode 1	MCA Channel		375	416	399	115	142	136
	Energy	[MeV]	25.50	28.29	27.13	9.59	11.84	11.34
	σ	[MeV]	4.01	4.45	4.27	1.94	2.39	2.29
	FWHM	[MeV]	12.65	-	-	4.50	-	-
		[%]	49.61	-	-	46.92	-	-
Mode 2	MCA Channel		-	706	-	-	313	-
	Energy	[MeV]	-	48.01	-	-	26.09	-
	σ	[MeV]	-	7.55	-	-	5.27	-

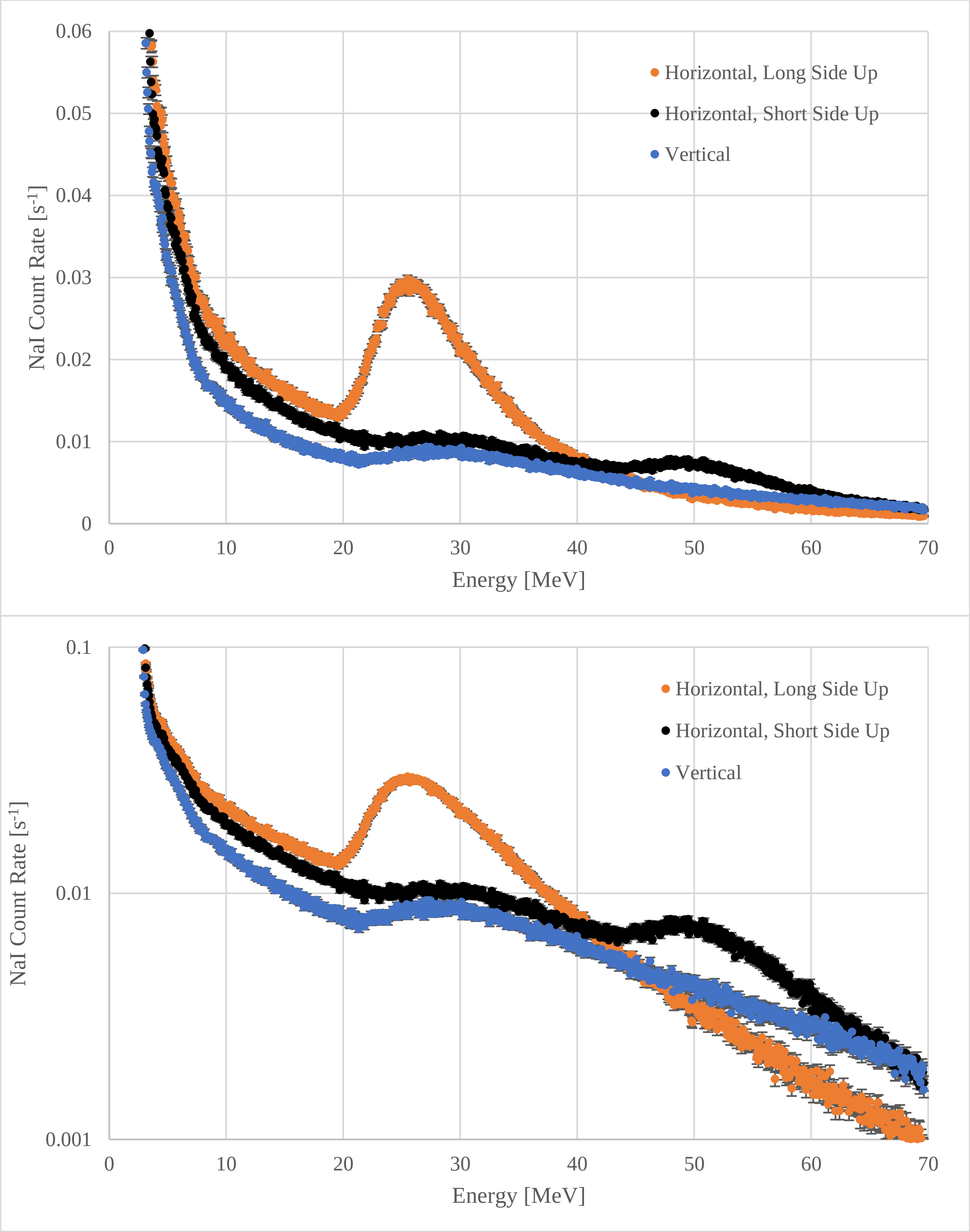

Figure 3-5. Measured energy spectra for NaI detector shown in absolute (top) and logarithmic (bottom) scales in the Horizontal-Long Side Up (orange), Horizontal-Short Side Up (black), and Vertical (blue) orientations. 1-σ error bars are included, which were calculated according to Poisson statistics. However, most error bars are obscured by the data markers.

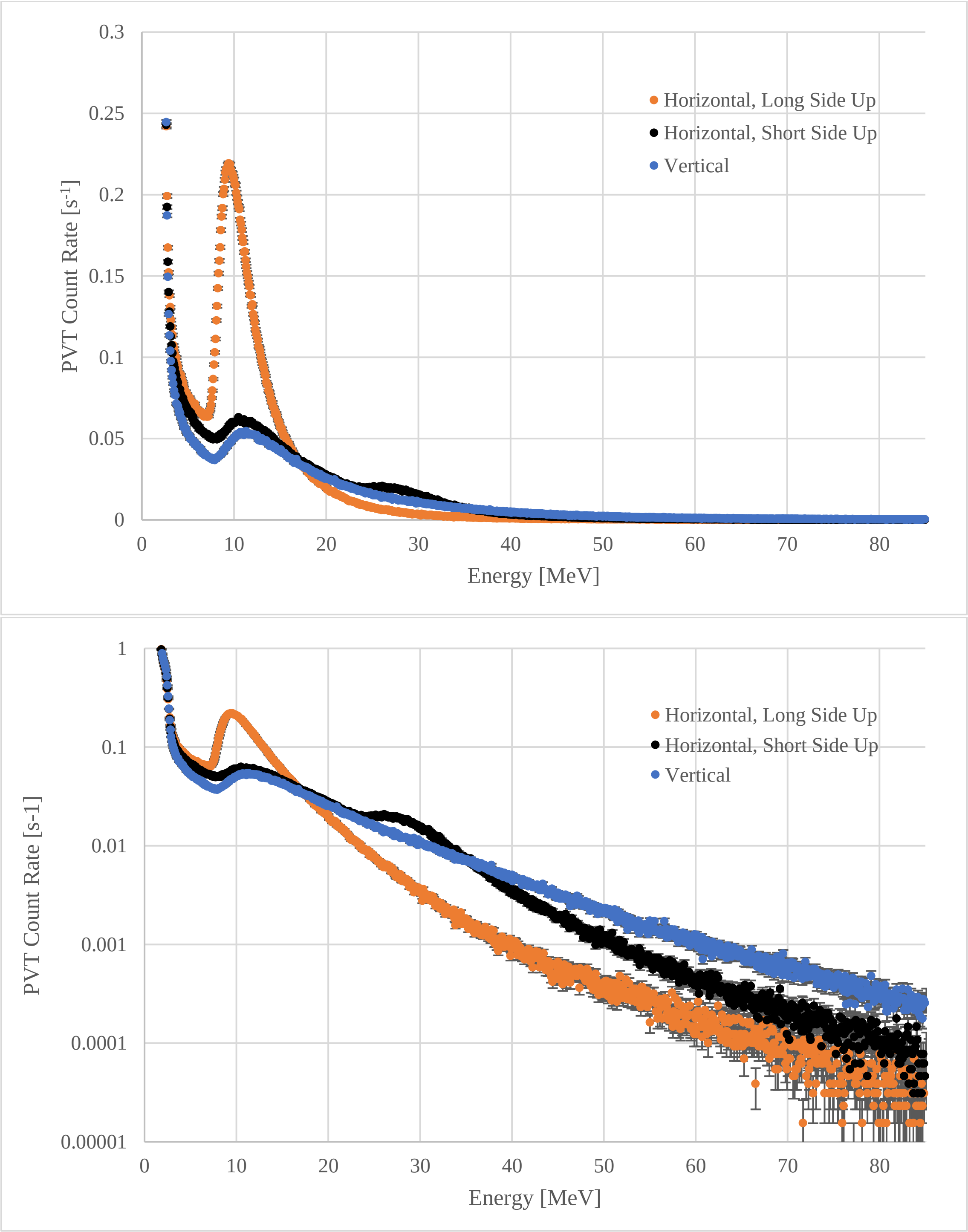

Figure 3-6. Measured energy spectra for PVT detector shown in absolute (top) and logarithmic (bottom) scales in the Horizontal-Long Side Up (orange), Horizontal-Short Side Up (black), and Vertical (blue) orientations. 1-σ error bars are included, which were calculated according to Poisson statistics. However, most error bars are obscured by the data markers.

These data show that the count rates vary with the detector’s geometry, following a positive relationship with the detector’s surface area orthogonal to the vertical axis. This indicates that the detected particles are produced at some distance either above or below the detectors. That aspect fits with the expectation that the particles are secondary cosmic rays produced in the atmosphere. The variance in the spectra with differing orientation suggest that the particles deposit energy as a function of path length and thus have electric charge. Specifically, the spectral features suggest that the charged particles are muons. This is indicated in the data for the Horizontal, Short Side Up orientation, whose modes’ energies are statistically the same as the expected muon energy deposition for the detectors’ two smaller dimensions as shown in Table 3.

Table 3-3. Comparison of measured modes’ energies in the Horizontal, Short Side Up orientation with expected muon energy deposition for path lengths equal to each detector’s two smallest dimensions.

		Measured		Calculated
	Dimension [cm]	Mode Energy [MeV]	Mode Energy Uncertainty [MeV]	Muon Energy Deposition [MeV]
NaI	5.08	28.29	4.45	24.31
	10.16	48.01	7.55	48.62
PVT	6.35	11.84	2.39	12.82
	16.51	26.09	5.27	33.33

For comparison against these measured spectra, the plots produced from the Python calculations of muon spectra are shown in Figure 7 for NaI and Figure 8 for PVT. The general shape of the calculated spectra match those from measurements, particularly where at least one mode is visible in each spectrum and instances where a second modes distinctly appear in some orientations. Similar to the measured data described above, the energy of a given mode correlates to a muon path length equal to one of the detector's dimensions. Both the modes' locations and the spectra's overall similarity indicate further that the measured spectra are produced by muons. With this result, it is worthwhile to consider the physics that contribute to the shape and variance of the spectra.

To better analyze the physics that cause these spectra, Figure 9 shows a magnified version of the calculated spectra for PVT in the Horizontal, Short Side Up orientation labeled for different spectral features. The idealized nature of this calculated spectrum aids in the precision of describing the physics. First are the modes of the spectrum, labelled B and D. The mode at B appears at 12.8 MeV indicates a path length of 6.35 cm, the detector's shortest dimension. The mode at D appears at 33.3 MeV similarly indicates a path length of 16.51 cm, the detector's middle dimension. Considering that with the detector's orientation indicate that B is the result of muons entering one of the detector's vertical faces (i.e. two of its larger "sides") with an approximately horizontal trajectory, and D is the result of muons entering the detector's upper horizontal face (i.e. its "top") with an approximately vertical trajectory. Diagrams of these muon paths can be seen in Figures 10(b) and 10(d), respectively. In this orientation, both modes are equally likely with probabilities of 0.032 and 0.035, respectively, and this is the result of the distribution of the muon trajectories and the detector's geometry. Muons are 8.4 times more likely to appear travelling vertically than horizontally (see Figure 2), but the detector's vertical face is 2.6 times larger than its horizontal face, which means there are 5.2 times more potential horizontal muon paths then vertical ones. This suggests that the peak probability of mode D would be 1.6 times that of mode B. While Figure 9 shows that the probability of D is only 1.1 times that of B, the difference from this expectation is likely a result of the binning scheme for the calculations.

Two other features on this spectrum are continuums. The first is a continuum of energies less than mode B, labelled A, which is the result of muon path lengths shorter than the detector's shortest dimension. Energies within this continuum are equally likely, and they have a probability approximately one third of that of mode B. This is largely the result of muons entering the detector through one face and exiting though an orthogonal face: entering through the top and leaving out a side, entering through a side and leaving through the bottom, or entering through one side and leaving through a perpendicular side (i.e. "cutting the corners"). The other continuum is that of energies between modes B and D, labelled C. Similar to A, it is the result of muon path lengths longer than the detector's shortest dimension and shorter than its middle dimension. This continuum has a similar physical cause as that at A, but it also is the result of muons entering and exiting parallel sides of the detector with a non-zero angle with these faces' normal vectors. Unlike A, the energies within this continuum vary in their likelihood, where the energies near B are half as likely as that of B and the energies near D are approximately one eighth as likely as B. This is a result of an energy's stronger dependence on the muon's vertical angle of trajectory that decreases in probability as the angle increases. Diagrams of the muon paths that produce continuums A and C can be seen in Figures 10(a) and 10(c), respectively.

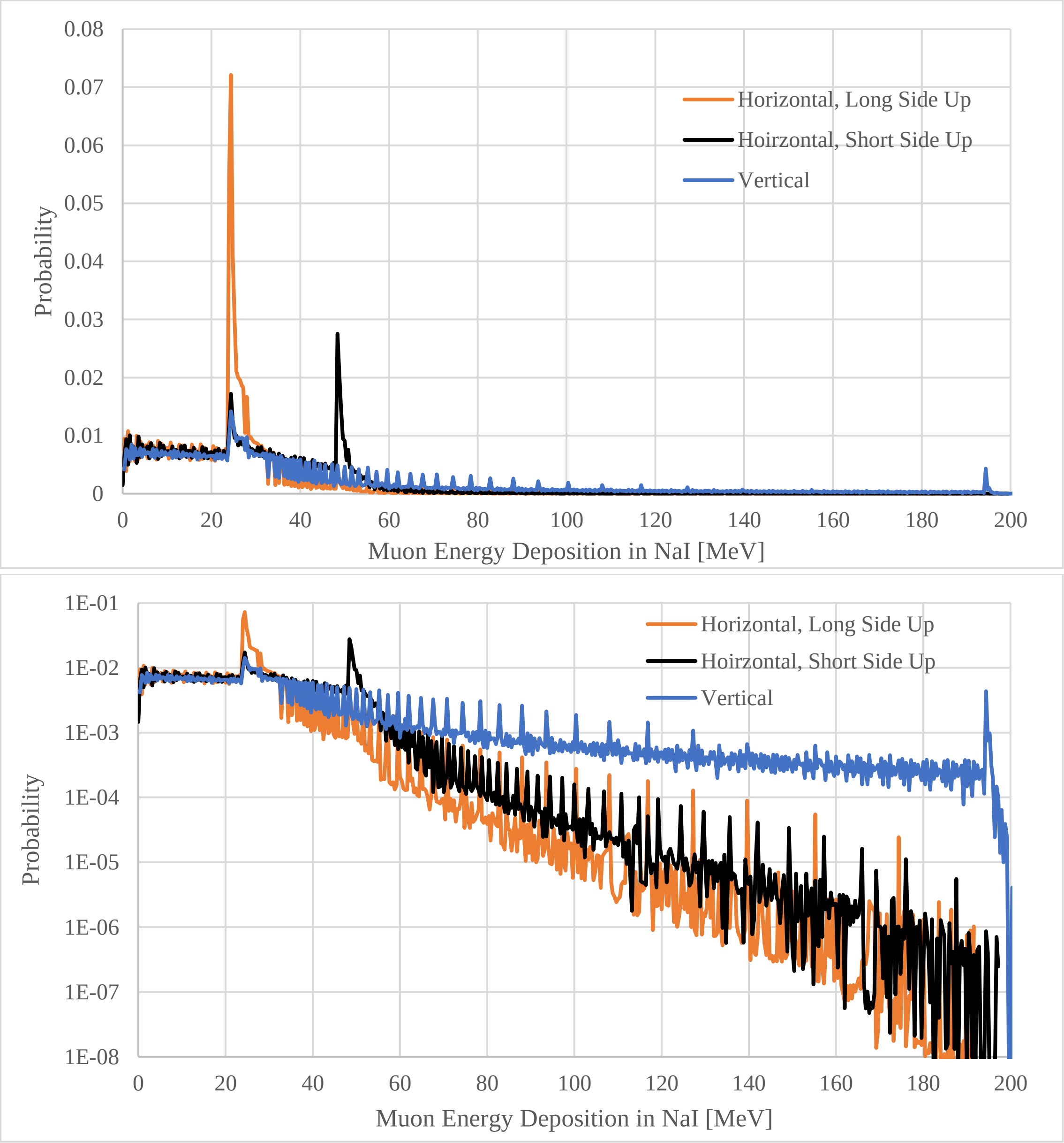

Figure 3-7. Energy spectra for NaI detector calculated as the muon path length distribution multiplied by its linear energy deposition, which are shown in absolute (top) and logarithmic (bottom) scales in the Horizontal-Long Side Up (orange), Horizontal-Short Side Up (black), and Vertical (blue) orientations.

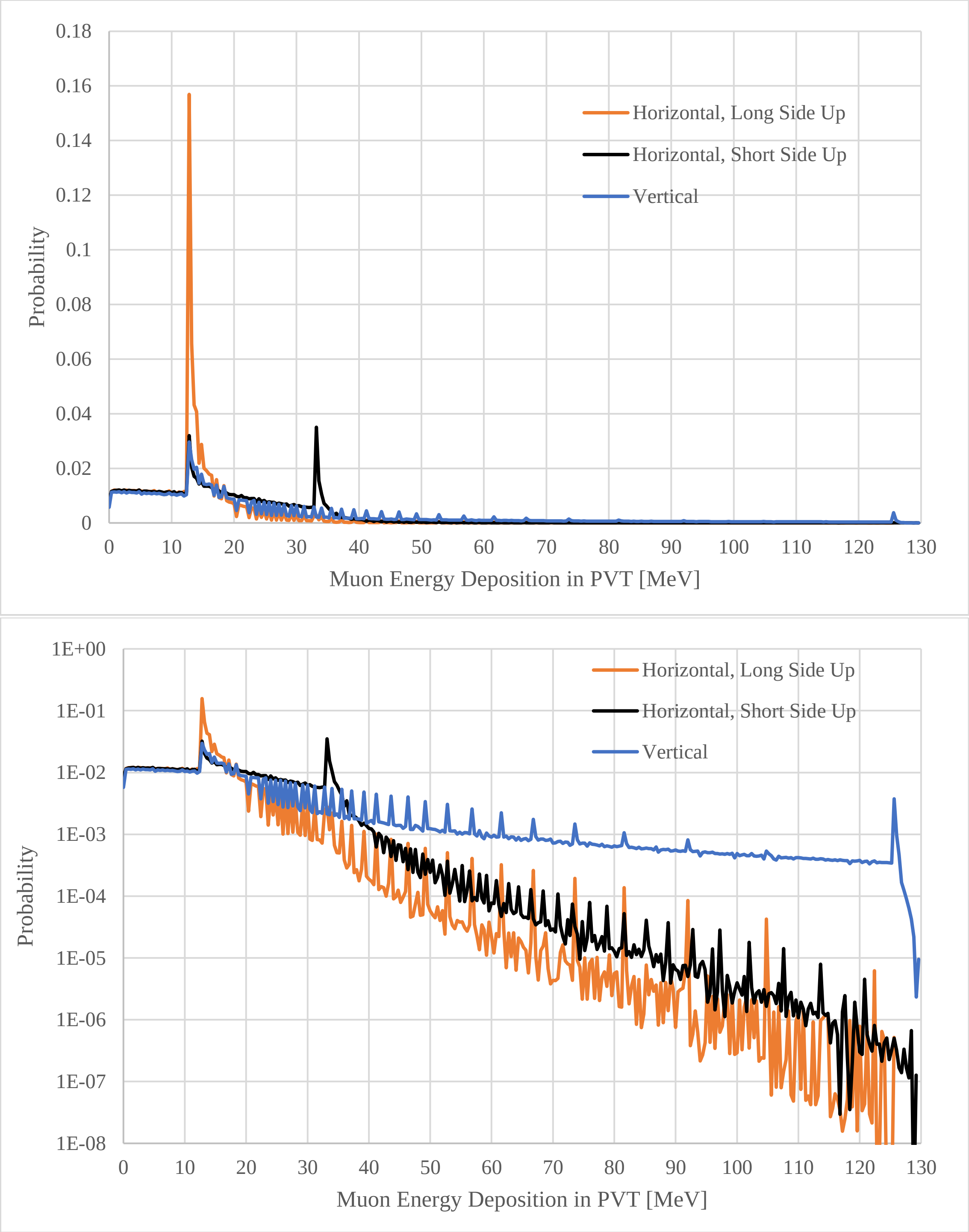

Figure 3-8. Energy spectra for PVT detector calculated as the muon path length distribution multiplied by its linear energy deposition, which are shown in absolute (top) and logarithmic (bottom) scales in the Horizontal-Long Side Up (orange), Horizontal-Short Side Up (black), and Vertical (blue) orientations.

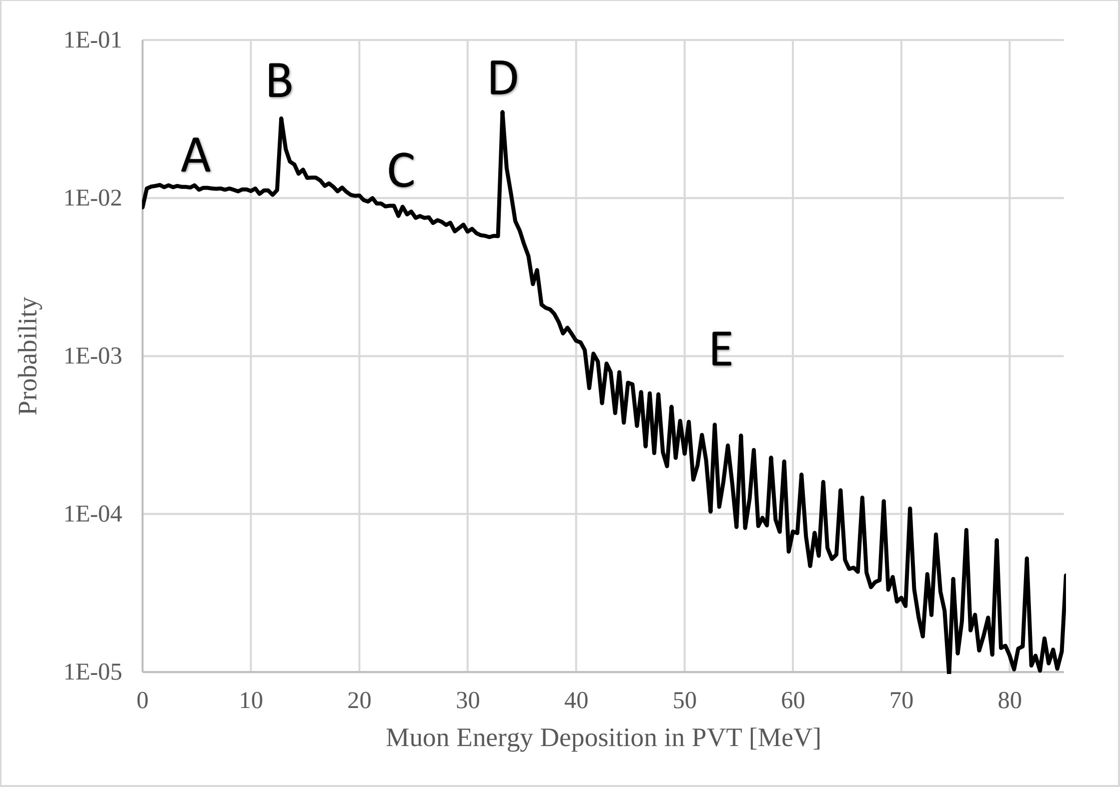

Figure 3-9. Calculated spectra for the Horizontal, Short Side Up orientation of PVT labeled for various characteristics.

The last feature of the energy spectrum is for energies above that of mode D, labelled E. Energies in section E have an exponential decline in probability as energy increases up to that for the maximum muon path length, which is that of an exactly diagonal trajectory through the detector (64.70 cm or 130.62 MeV). The cyclic spikes in this section are a result of both the binning scheme and the calculation resolution. These spikes can be smoothed out by either increasing the bins' width or increasing the resolution in the muons' entry locations and polar angles when doing these calculations. The latter is increasingly taxing on computer memory, but a coarser resolution causes an increasing undercount of long trajectories. Along with the exponential decline, the area near mode D has a much smaller slope than that exponential, which creates a “shoulder” on the right side of the mode at D. These are the result of muons with a variety of paths through the detector, and their energy largely depends on angle that the muon’s trajectory has with the vertical axis. At lower energies, the muons enter the top of the detector with a non-zero vertical angle that is small enough for it to still leave through the bottom of the detector (i.e. path lengths slightly longer than the detector’s vertical dimension). At increasing energies, the muons’ trajectory has an increasing vertical angle, and they either enter through the side of the detector and leave through the bottom or enter through the top and leave out the side. At the highest energies, the muons will have a large vertical angle, resulting in a trajectory approximately parallel with the detector’s longest dimension, which results in very long path lengths. This dependence on the muon’s vertical angle thus produces the exponential decline in probability with energy. Examples of these possible paths can be seen in Figure 10(e).

These features are visible with varying prominence in all three orientations for both detectors, and the energy ranges will remain the same for the same detector. For PVT in the Vertical orientation, the energy of mode B remains the same, and that of mode D increases to 125.6 MeV. That increase is because muons are more likely to travel vertically and thus take a 62.23 cm path, which means that a second mode would appear in the measured data if the detectors were calibrated to measure these higher energies. This increase naturally comes with a widening of continuum C (as more intermediate path lengths/energies are possible) and a contraction of section E (as there are only a few paths longer than the detector’s longest dimension). In this case, the mode at B is more likely than that at E because of the large difference between the area of the detector’s side surface (which is the detector’s largest surface) and that of its top surface (its smallest surface). This difference allows for 19.6 times more possible horizontal paths than vertical ones. Combining this with the difference in vertical to horizontal muon trajectories (a factor of 8.4 as stated above) suggests that mode B should be 2.3 times more likely than mode D. However, the calculated spectrum shows this difference has a factor of 7.9. This variance from expectation is likely a result of the calculation’s resolution since longer paths are more likely to be undercounted with decreasing position and polar angle resolution.

For PVT in the Horizontal, Long Side Up orientation, the mode D disappears while the other features are still present. This, again, is the result of the difference in surface areas of the top and sides of the detector. The top is now the detector’s largest surface, allowing for 1.3 times more vertical paths, which means that a muon with a vertical trajectory is 10.9 times more likely to interact with the detector than one with a horizontal trajectory. This effectively causes mode D to disappear, both in the calculated and measured spectra. Despite this aspect, the continuum C is still visible upon closer inspection. Like in the other horizontal orientation, that continuum appears above energies of mode B (i.e. for muon path lengths equal to the detector’s shortest dimension) and below energies for muon path lengths equal to the detector’s middle dimension (where mode D would be). Again, this is a result of muons (which largely enter the top of the detector) that have paths of intermediate length between the detector’s shortest and middle dimensions. Besides the differences in the modes, the spectral features A and E in this orientation are largely the same as those in the other horizontal orientation.

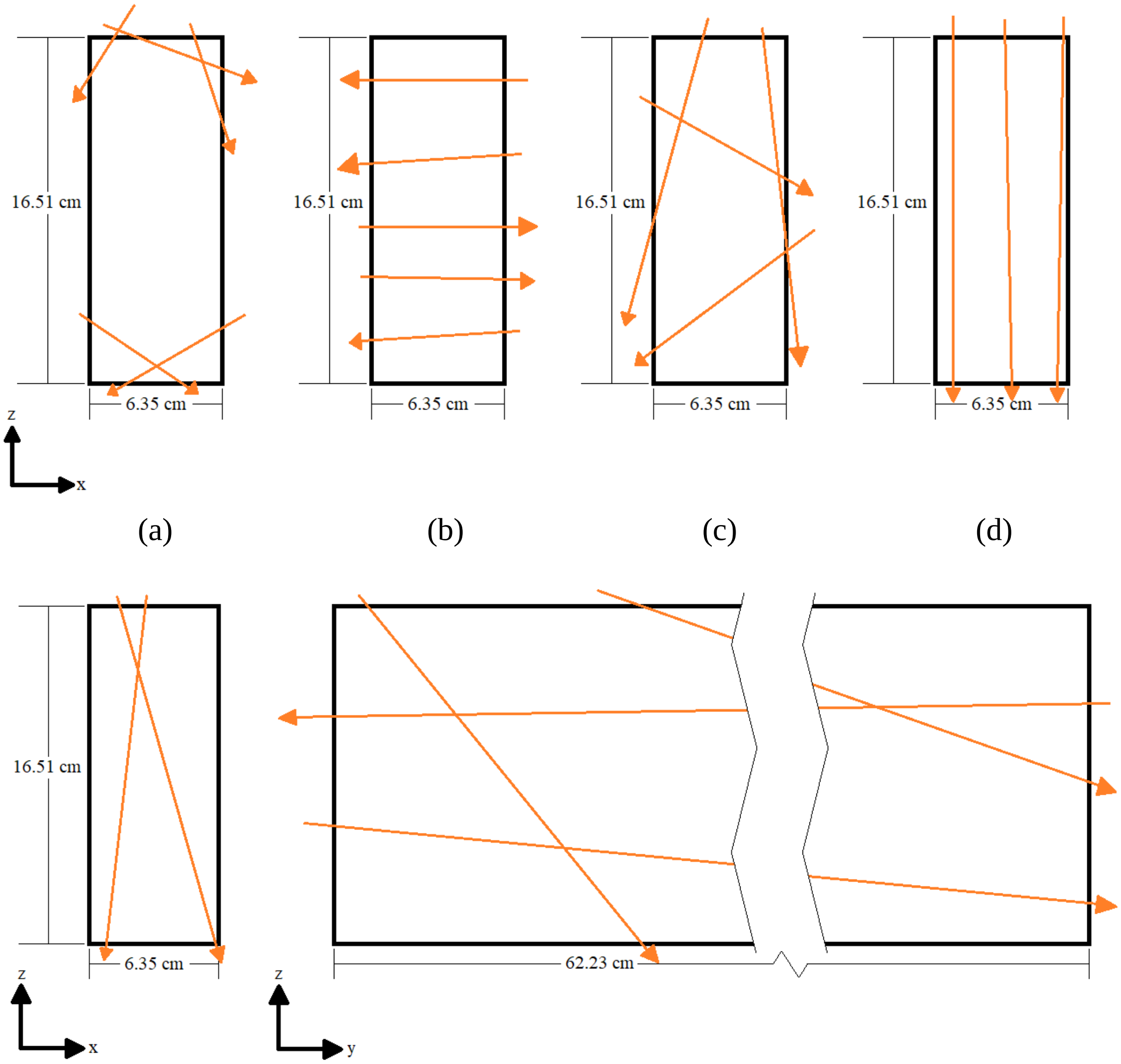

(a) (b) (c) (d)

(e)

Figure 3-10. Diagrams showing the examples of muon paths (orange arrows) through PVT in the Horizontal, Short Side Up orientation which contribute to spectral features A-E, respectively labeled (a)-(e).

The MCNP simulated muon spectra are shown in Figure 11 for the NaI detector and in Figure 12 for the PVT detector. The shapes of these spectra are similar to those from measurements and those from Python calculations. More importantly, similar spectral variations based on orientation are visible. The modal data for the simulations are shown in Table 4. The energies of these modes are similar to those from measurements. This includes a prominent mode in all orientations that appears for muon path lengths equal to the detector’s shortest dimension, and in the Horizontal, Short Side Up orientation, a second mode appears for path lengths equal to the detector’s middle dimension. Comparing these modes to those from measured data as shown in Table 5 reveal that all the modes’ energies are statistically the same at the 2-σ level and half are the same at the 1-σ level.

Table 3-4. Modal data for simulations of background muon response in NaI and PVT by orientation.

		Detector	NaI			PVT		
		Orientation	Horizontal, Long Side Up	Horizontal, Short Side Up	Vertical	Horizontal, Long Side Up	Horizontal, Short Side Up	Vertical
Mode 1	Energy	[MeV]	22.316	28.084	31.824	11.968	13.396	13.736
	FWHM	[MeV]	13.396	[1]19.588	16.796	7.344	5.984	8.772
		[%]	50.9	[1]69.7	52.8	61.4	44.7	63.9
Mode 2	Energy	[MeV]	-	52.360	-	-	31.960	-

[1] Linear extrapolation used to estimate the left half-maximum value.

Table 3-5. Comparison of modal data for both measured and simulated background muon response in NaI and PVT by orientation.

			Detector	NaI			PVT		
			Orientation	Horizontal, Long Side Up	Horizontal, Short Side Up	Vertical	Horizontal, Long Side Up	Horizontal, Short Side Up	Vertical
Mode 1	Measured	Energy	[MeV]	25.50	28.29	27.13	9.59	11.84	11.34
		σ	[MeV]	4.01	4.45	4.27	1.94	2.39	2.29
	MCNP	Energy	[MeV]	22.316	28.084	31.824	11.968	13.396	13.736
	Difference		**[MeV]**	**3.184**	**0.206**	**4.694**	**2.378**	**1.556**	**2.396**
	Difference/σ			**0.794**	**0.046**	**1.099**	**1.226**	**0.651**	**1.046**
Mode 2	Measured	Energy	[MeV]	-	48.01	-	-	26.09	-
		σ	[MeV]	-	7.55	-	-	5.27	-
	MCNP	Energy	[MeV]	-	52.360	-	-	31.960	-
	Difference		**[MeV]**	**-**	**4.350**	**-**	**-**	**5.870**	**-**
	Difference/σ			**-**	**0.576**	**-**	**-**	**1.114**	**-**

These data indicate that muons are the particle responsible for the background response in these scintillator detectors. This aspect is especially useful for mobile search systems as background muons and neutrons are largely produced by secondary cosmic ray interactions, and therefore, their fluxes would likely be proportional in most situations [13]. As mentioned above, this proportionality has been seen in operational data employing high energy scintillator measurements. These characteristics suggest that it could be possible to apply the high energy scintillator response to characterize background more effectively in neutron counting systems during mobile searches.

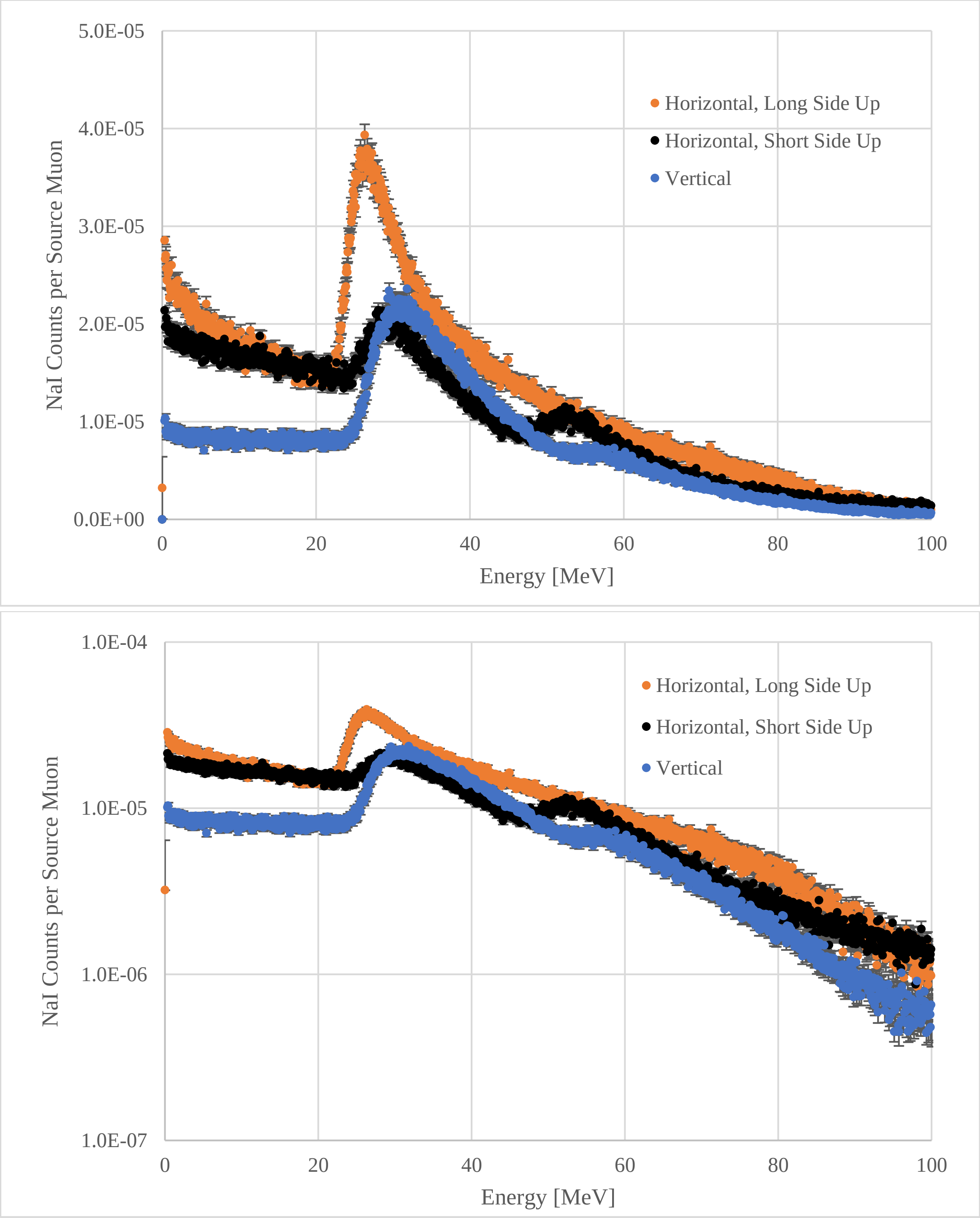

Figure 3-11. Simulated energy spectra for NaI detector shown in absolute (top) and logarithmic (bottom) scales in the Horizontal-Long Side Up (orange), Horizontal-Short Side Up (black), and Vertical (blue) orientations. Counts were modified such that the relative proportions by orientation were like measured data. 1-σ error bars are included, which were calculated from the MCNP-reported relative error. However, most error bars are obscured by the data markers.

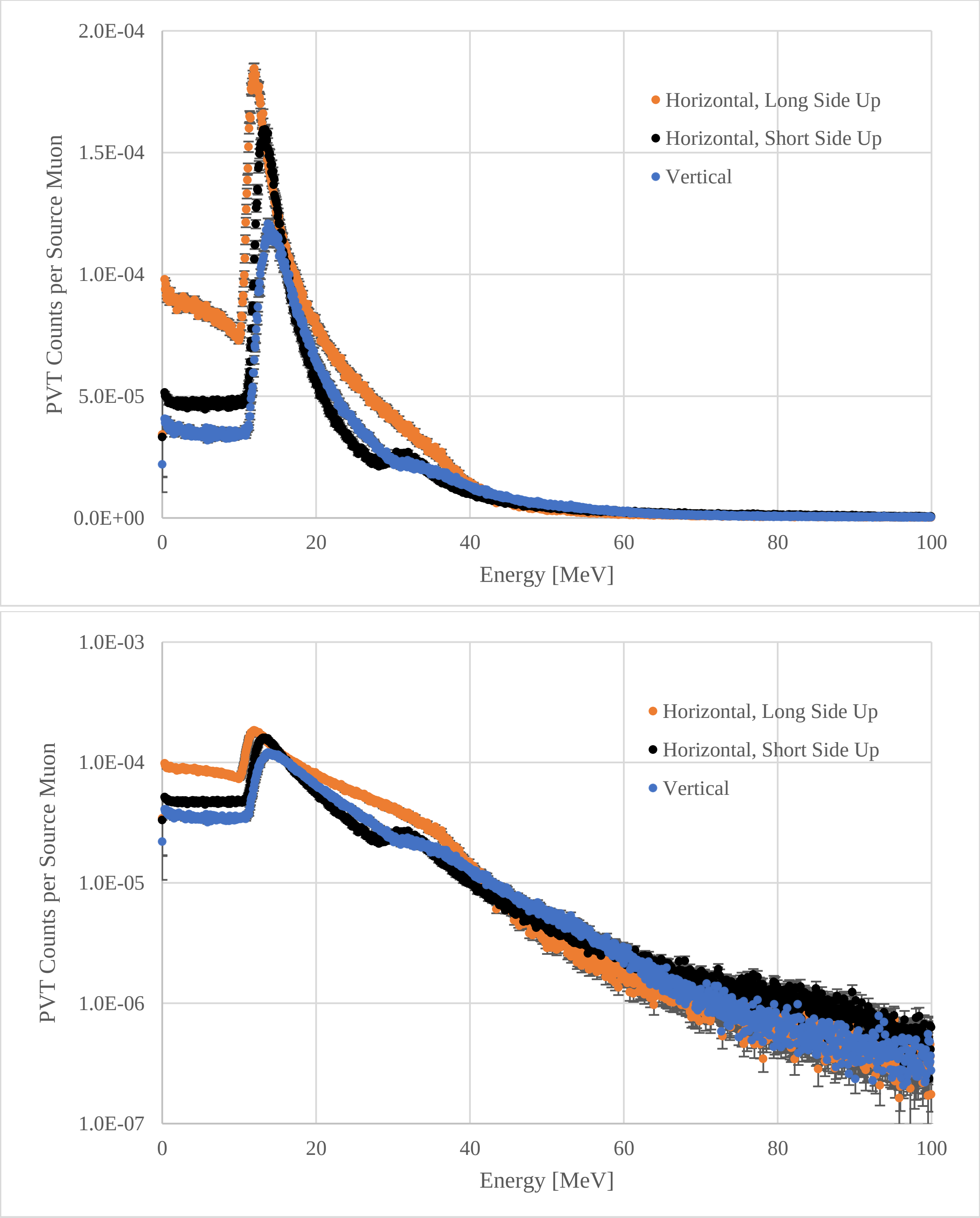

Figure 3-12. Simulated energy spectra for PVT detector shown in absolute (top) and logarithmic (bottom) scales in the Horizontal-Long Side Up (orange), Horizontal-Short Side Up (black), and Vertical (blue) orientations. Counts were modified such that the relative proportions by orientation were like measured data. 1-σ error bars are included, which were calculated from the MCNP-reported relative error. However, most error bars are obscured by the data markers.

3.4. Conclusion

This work shows that the background response at high energies in scintillation detectors is mostly the result of muons. These muons produce peaks whose centroids appear at energies between 5 MeV and 60 MeV depending on the detector's orientation and composition. Mobile search systems commonly use these scintillation materials, and operational data (along with previous work) show that these high energy signals (caused by muons) are correlated with the background response from a neutron counter. Because of this, it seems plausible that a method could be devised to predict the background response in a neutron counting system using the background response from muons. This aspect will require further study to characterize the relationship and test the method's applicability for mobile searches.

3.5. References

1. G. F. Knoll, *Radiation Detection and Measurement*, 4th Edition, John Wiley & Sons, 2010.
2. T. Ichimiya, T. Narita, K. Kitao, "Natural background gamma-ray spectrum List of gamma-rays ordered in energy from natural radionuclides (JAERI-Data/Code--98-008)," Japan Atomic Energy Research Institute, 1998. https://inis.iaea.org/collection/NCLCollectionStore/_Public/29/033/29033666.pdf.
3. S. Hayakawa, *Cosmic Ray Physics – Nuclear and Astrophysical Aspects*, John Wiley & Sons, 1969.
4. J. N. Wagner, C. Marianno, T. McCullough, "Parking Garage Measurements Indicating a Gamma Spectrometer-Neutron Counter Background Correlation,"

International Journal of Nuclear Security, Vol. 6: No. 1, Article 6. July 2020. Available at: https://trace.tennessee.edu/ijns/vol6/iss1/6/

5. Alpha Spectra, Inc. "ASI 2" x 4" x 16" Detector Data Sheet," available at https://alphaspectra.com/wp-content/uploads/ASI-2in-x-4in-x-16in-NaITl-Data-Sheet.pdf (accessed on 7 September 2020).
6. Alpha Spectra, Inc. "Nomenclature – ASI Model Numbers Explained," available at https://alphaspectra.com/nomenclature/ (accessed on 7 September 2020).
7. Alpha Spectra, Inc. "ASI-100 Plastic Scintillator," available at https://alphaspectra.com/wp-content/uploads/ASI-100-Plastic-Scintillator.pdf accessed on 7 September 2020).
8. AMETEK Inc. – ORTEC, "digiBASE 14-Pin PNT Tube Base with Integrated Bias Supply, Preamplifier, and MCA (with Digital Signal Processing) for NaI Spectroscopy," available at https://www.ortec-online.com/-/media/ametekortec/brochures/digibase.pdf (accessed on September 7th, 2020).
9. AMETEK Inc. – ORTEC, "MAESTRO Multichannel Analyzer Emulation Software," available at https://www.ortec-online.com/-/media/ametekortec/brochures/maestro.pdf?dmc=1&la=en accessed on September 7th, 2020).
10. Gooding, T. J. and Pugh, H. G. "The Response of Plastic Scintillators to High-energy Particles" *Nuclear Instruments and Methods*. Vol. 7 (1960) pp. 189-192.
11. Taylor, C. J., et. al. "Response of Some Scintillation Crystals to Charged Particles." *Physical Review*. Vol. 84, No. 5 (1 December 1951). pp. 1034-1043.

12. W. Preusse and S. Unterricker, “The contribution of cosmic ray muons to the background spectrum of gamma ray spectrometers.” *Nuclear Instruments and Methods in Physics Research B*. Vol. 94 (1994) pp. 569-574
13. J. F. Ziegler, “Terrestrial Cosmic Rays”, *IBM Journal of Research and Development*, 1996, p 23.
14. P. K. F. Grieder, *Cosmic Rays at Earth – Researcher’s Reference Manual and Data Book*, Elsevier, 2001.
15. C. Y. E. Ho, “Cosmic Ray Muon Detection Using NaI Detectors and Plastic Scintillators,” University of Virginia. Available at https://home.fnal.gov/~group/WORK/muonDetection.pdf accessed on September 7th, 2020).
16. D. E. Groom et. al, “Muon Stopping Power and Range Tables 10 MeV – 100 TeV,” *Atomic Data and Nuclear Data Tables*, Vol 76, No. 2. July 2001.
17. C.J. Werner, et al., "MCNP6.2 Release Notes", Los Alamos National Laboratory, report LA-UR-18-20808 (2018).

4. CHARACTERIZATION OF A GAMMA SPECTROMETER-NEUTRON COUNTER BACKGROUND CORRELATION IN MOBILE SEARCH SYSTEMS*

4.1. Introduction

One major concern in nuclear security is nuclear terrorism. If an attack did occur, a terrorist group would likely use a radiological dispersal device (RDD – known as a "dirty bomb") or an improvised nuclear device (IND). Recent events have put into perspective the potential damage if an IND were used in an attack, particularly the August 2020 explosion in Beirut, Lebanon. While the ammonium nitrate explosion was the result of negligence, its yield was estimated to be equivalent to 0.5-1.5 kilotons of TNT [1,2]. This caused widespread, catastrophic damage to the city of Beirut. Low yield weapons of less than 10 kT have been designed and tested by both the United States and Russia; therefore, it is conceivable that even a poorly designed IND would have an explosive yield equivalent to (or greater than) that in Beirut. This would result in similar levels of damage in addition to the spread of radiological contamination.

Ideally, an RDD or IND would be found before it detonated, but if one does detonate, one central question in its response becomes "are there more?" The latter was a concern during recent incidents (also non-nuclear ones) in the United States, namely the successful bombing of downtown Nashville on December 25, 2020, and the unsuccessful use of pipe bombs as part of the terror attack on the United States Capitol on January 6, 2021 [3,4]. During those events, responders' time was very limited to find and neutralize any

---

*Reprinted with permission from ARTICLE TITLE by Jackson N. Wagner, Craig Marianno, and Daren Cline in *JOURNAL* additional threats before they caused harm. The same is true, to a lesser degree, when securing an area that may be a target like a major public event, and in both cases, nuclear security operators would employ the mobile search system in an area to find an RDD or IND.

Mobile radiation search systems would be used to find the signature radiation these devices emit These systems employ vehicle-mounted gamma spectroscopy and neutron counting systems to canvass an area of interest [5]. Unfortunately, the necessity to investigate an area and do so quickly introduces difficulties in characterizing the ambient, or “background,” responses in both systems. These difficulties can be mitigated in the gamma spectroscopy system as the background spectrum is unique from that of any man-made radiological material. Conversely, this ability does not exist for the neutron counting system as it does not provide spectral data. In addition, the characteristics of the background neutron flux and the neutron detection systems result in low count rates that can vary significantly with common changes, particularly elevation and surrounding materials. These aspects can result in false neutron alarms from background changes or lack of alarms for weak neutron sources.

Previous work has indicated a correlation between the neutron count rate and the high-energy count rate in the gamma spectrometer above 4 MeV. This correlation appears in published measurements of various parking garages on the Texas A&M University campus [6]. Further work showed that these high energy signals are the result of muons and their correlation with neutrons is plausible as they are produced by similar processes, namely cosmic rays interacting with the Earth's upper atmosphere [7,8,9].

A well characterized relationship between the muon and neutron count rates will provide a method for better characterizing the background in the neutron counting system. This would enable the estimation of the background neutron count rate using the measured muon count rate. Since there are no man-made sources of muons, this estimation would not be affected by the presence of a man-made source of radiation [7]. A quality estimate of the neutron background would improve the sensitivity of the neutron counting system while reducing false alarms (i.e. make it easier to detect weaker neutron sources while adjusting to normal background changes). The latter is particularly important due to the time sensitivity of mobile search operations as false alarms take time to adjudicate.

Data that were analyzed to characterize this relationship came from three sources: measurements performed by the authors, measurements performed by nuclear security operators in cooperation with the authors, and measurements collected by other nuclear security operators during their standard operations. All three measurement sets consist of data from each organization's available gamma spectroscopy and neutron counting systems, and the detectors' readings were associated with the mobile search system's GPS location every second. Data from each source was analyzed independently from the other two. This is because the difference in equipment available to the authors and each of the two operators along with the difference in data collection methodology between the two operators.

Analysis of these three organizations' data sought to determine the expected form of the neutron-muon relationship. If a relationship exists, this analysis also sought to observe whether it varies in relation to three significant variables: elevation, latitude, and area type. These variables were considered because each is correlated with changes in the neutron and muon fluxes at the Earth's surface. Elevation was the first significant variable because neutrons and muons are two types of particles produced with the interaction of cosmic rays with the upper atmosphere. In this case, the atmosphere itself acts as a shield for these secondary particles. Previous work has indicated an exponential relationship between these particles' fluxes and the atmospheric density, where the fluxes increase as the density decreases in the lower atmosphere [9]. Atmospheric density has a strong correlation with elevation, and a linear approximation is valid up to 2000 m [10,11]. This enables the use of elevation in place of atmospheric density, and the mobile search system is able to measure elevation through its GPS location.

Latitude was the second significant variable considered, and it indicated variances in the Earth's magnetic field, where that field acts as a shield to the primary cosmic rays before they interact with the atmosphere. This is because the cosmic rays the create neutrons and muons are mostly made up of protons. As a result, some of those cosmic particles are deflected as they move through the magnetic field due to forces which follow the "righthand rule" of physics [8,9]. The more these primary cosmic particles are deflected, the larger the reduction in the flux of neutrons and muons at the Earth's surface. The strength of this shielding effect is described through a location's geomagnetic rigidity, where larger rigidity values indicate that the magnetic field has a more horizontal direction (relative to the ground) and thus deflects more cosmic rays. In the continental United States, this value has a strong inverse correlation with latitude, which means the neutron and muon fluxes are higher in the Northern US than in the Southern US [9].

The third variable is an area's level of urbanization, which indicates the amount and/or geometry of material around the detectors. Many materials, particularly common building materials like concrete, may also shield neutrons and muons. These shielding effects occur when those materials are directly overhead or nearby the detectors. To capture the presence of these materials, urbanization is separated into four broad categories:

1. rural – open, largely undeveloped areas, possibly with isolated buildings nearby
2. suburban – lightly or moderately developed areas with many short (i.e. less than three stories tall) buildings nearby, which includes areas with significantly developed road infrastructure (i.e. an interstate highway in a city)
3. urban – highly developed areas with a high density of tall (four or more stories tall) buildings nearby, sometimes referred to as "urban canyons"
4. parking garage – within a parking garage or other extreme environment where materials are directly above and below the mobile system and the system can move a nontrivial distance above or below the ground.

In collecting data for this analysis, measurements sought to achieve samples of all three variables with ranges as broad as possible, and those from the three sources described above had a variety of success in this regard. First, the authors' measurements described below were able to achieve a broad sample of all three variables through numerous measurement campaigns that controlled for detector setup as much as possible. This included measurements to remove potential correlations between one or more variables. Second, two teams of nuclear security operators collected additional data for this research. Their measurements produced a broad enough sample across one of latitude or elevation when the teams' data were considered together, but a correlation between those two variables meant both could not be considered. These teams' collection methodology was similar to those described below with their own systems. However, equipment availability resulted in an inability to strictly control for detector setup. These differences were known and were accounted for as best as possible during analysis but could not be done precisely. Finally, another nuclear security organization provided data from their typical operations. Their data were collected through numerous campaigns with many different mobile search systems employed over a four-year period (between 2013 and 2017). While these data produced the broadest sample across both elevation and latitude, information on their collection methodology and detector setup were not provided beyond the number of each detector. The latter aspect was accounted for in the analysis of their data for this research. However, because of this potential for experimental inconsistencies, conclusions drawn from this dataset may not be as strong as those from the former two.

4.2. Materials and Methods

The authors' measurements sought to emulate mobile search systems as much as possible, namely by employing both gamma spectroscopy and neutron counting systems in a moving vehicle. The gamma spectroscopy system used at least one 2"-by-4"-by-16" (5.08 cm-by-10.16 cm-by-40.64 cm) sodium iodide (NaI) detection system with an Ametek-Ortec (Oak Ridge, TN) digiBASE multichannel analyzer (MCA) [12]. Energy calibrations were made using ^{137}Cs and ^{22}Na as shown in Table 4-1 to achieve an approximately 70 MeV energy scale, which is significantly different than that used in operational mobile search systems. This was necessary to enable the discrimination of background gamma rays as previous work showed that muons are the primary particle measured on these energy scales [7]. Gamma ray information was discriminated by ignoring data below 4 MeV, which correlated with channel 62 (of 1024, with the first channel labeled "0") on this energy scale. Since previous work shows that the detector's orientation may vary the muon count rate, two of these detectors were employed with one laying flat with its largest face parallel to the ground (i.e. with its largest face "looking up" from the vehicle) and the other laying with its largest face perpendicular to the ground (i.e. with its largest face "looking out" from the vehicle). However, only the data from the "looking up" orientation were considered because the effect of the detector's orientation would only alter the muon data by a multiplicative constant. All the measurement campaigns used at least one neutron counter. Most campaigns used an Ortec system with four 1"-by-18" (2.54 cm-by-45.72 cm) ^{3}He tubes encased in a high-density polyethylene (HDPE) moderator [5]. Additionally, one campaign used only a Thermo Fisher Scientific (Waltham, MA)

Packeye backpack system with 2”-by-16” (5.08 cm-by-40.64 cm) ^{3}He tubes without a moderator, and one campaign used both of these systems [13]. Photos of these detectors individually are shown in Figure 4-1.

Table 4-1. Calibration information for the NaI and PVT detector.

				^{137}Cs	^{22}Na	
	Gamma Ray Energy		[keV]	662	511	1274
NaI	Photopeak	Energy	[keV]	662	511	1274
		Channel Number		10.5 ± 1	8 ± 1	19.5 ± 1
	digiBASE Voltage		[V]	500		
	Calibration		[keV ch^{-1}]	68.0 ± 10.7		
PVT	Compton Edge	Energy	[keV]	477.65	-	1061.18
		Channel Number		8 ± 1	-	15 ± 1
	digiBASE Voltage		[V]	720		
	Calibration		[keV ch^{-1}]	83.3 ± 16.8		

Measurements were performed in a variety of locations throughout the central region of the continental United States. The two largest campaigns in terms of area collected data during long-haul roundtrip travel starting in College Station, Texas. Most of the areas on these campaigns were classified as “rural” for the urbanization variable since much of them were open, lightly developed highways. The first was a trip to/from Los Alamos, New Mexico, with stops in Hobbs, Albuquerque, Santa Fe, and Clovis, New Mexico. This mainly used a charter bus, which prevented the use of the Ortec neutron counting system, and only the Thermo backpack system was used, instead. In addition to these, measurements were collected from a sedan in the Santa Fe, New Mexico, area, and the different vehicle allowed for the use of both neutron counting systems. The other trip was to/from Ann Arbor, Michigan, with stops in Effingham, Illinois, and Warsaw, Indiana. Unlike the other trip, this one used a mid-sized SUV, allowing the Ortec neutron counter to be used. The Thermo backpack was not used for this second trip or any other campaign because its data collection system failed after the first trip. This failure made the detector unusable since its data could no longer be logged. Therefore, only the Ortec system was used for neutron counting on the second trip and all other measurement campaigns.

Other measurement campaigns took place in localized areas which consisted of two types that focused on two different urbanization categories. One type canvassed the urban areas of major cities in Texas. These cities were Austin, Dallas, Fort Worth, Houston, and San Antonio, and the followed routes to cover as much of their downtown areas as possible. This was completed to see what effect an "urban canyon" had on the neutron and muon background. The other type of campaign focused specifically on parking garages on the Texas A&M University campus, specifically, the Polo Road Garage (PRG), the Central Campus Garage (CCG), and the South Side Garage (SSG). These measurements had a similar method as performed in previous work, with one long, static measurement on each level, along with additional "sweep" measurements of the garages where the system traversed the entire structures [6]. Again, these were similar to those discussed in previous work, but measurements of only one garage were repeated (CCG) and used a slightly different system to allow the data's inclusion with the rest of the campaigns. The setup of the detectors in the various vehicles used for these campaigns are shown in Figure 4-2.

These images also show a PVT detector that was employed with a similar calibration as the NaI detectors. In addition to the detectors' data, GPS location data (including elevation) were logged every second for all these campaigns (where a GPS signal was attainable).

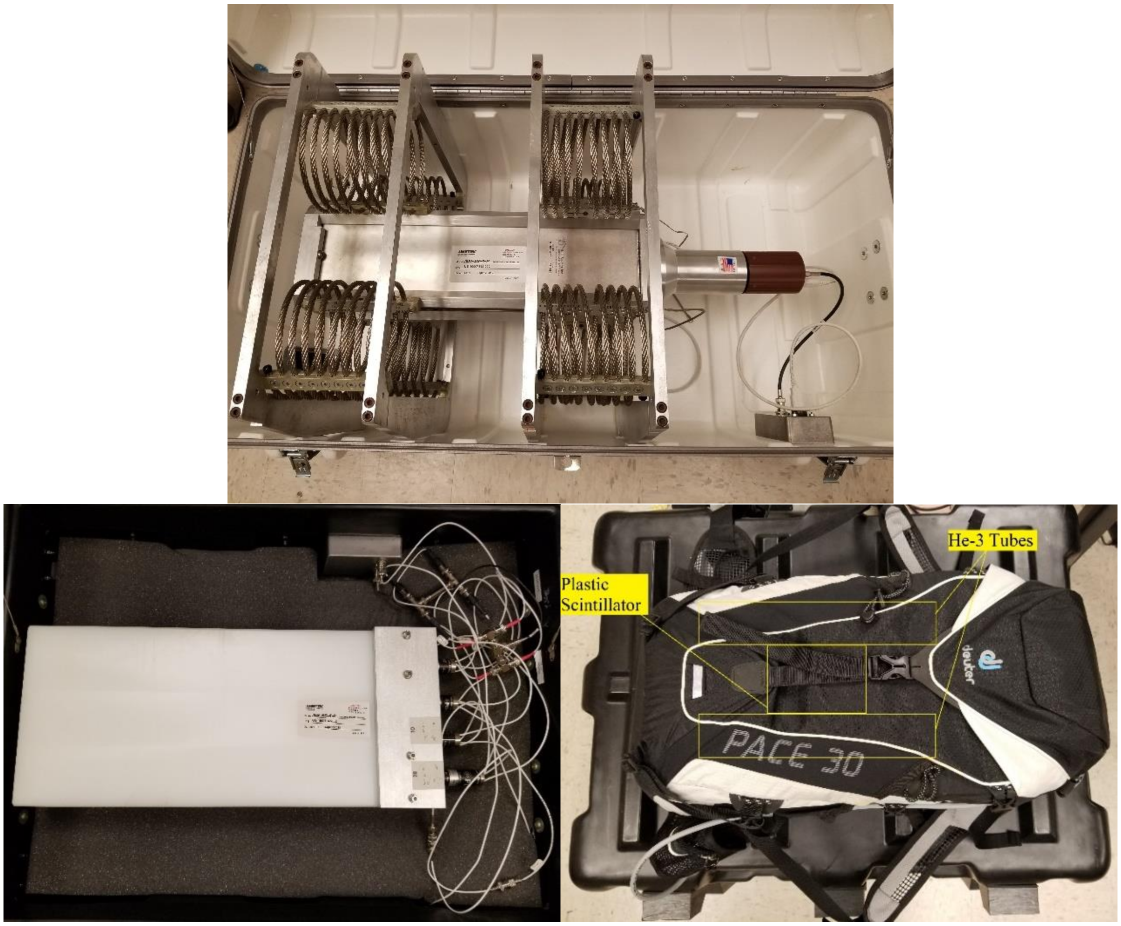

Figure 4-1. Photos of the NaI scintillator (top), Ortec NAI-SS neutron counter inside its ruggedized case (bottom left), and Thermo PackEye neutron counter (bottom right) used in mobile search measurements.

Similar data were obtained from two organizations that perform nuclear security operations, both of which are a part of the United States Department of Energy (DOE). One organization was the Radiological Assistance Program (RAP), and two of their teams were able to collect data in cooperation with the authors. The survey teams collected measurements in various area types (as defined above) near the cities in which the teams are based, namely Albuquerque, New Mexico, and Chicago, Illinois. These measurements were done using the teams' standard detection systems. The other organization that provided data was the Remote Sensing Laboratory (RSL), and their data were collected between 2013 and 2017 throughout the continental United States, primarily in cities. Unlike those from the RAP teams, the collection methodologies for RSL's measurements were not provided, nor were their precise detector setups. The only data RSL were able to provide were the measurement locations, the relevant count rate data, and the number of standard detectors used (i.e. the number of their standard gamma spectrometers or neutron counters). The locations of RSL's measurements are shown in Figure 4-3.

Each of these organizations' sets of data were analyzed independently for two reasons: the different detection systems that were used, and the different system configuration and operation methodologies used. The potential for difference is included in both reasons because much of the information about RSL's data are unknown for security reasons. Each organizations' standard neutron counting and gamma spectroscopy systems differed from those available to the authors. Another notable difference was that government systems used larger ^{3}He tubes for neutron counting and NaI detectors for gamma spectroscopy. A significant difference in the government measurement campaigns that instead of modifying the NaI energy scale to observe muon interactions, these systems employed an "overflow" channel, which counted all signals in the detector above their standard calibrated scale (typically 3 MeV).

The analysis of these data sought to observe and characterize a relationship between the neutron and muon count rates over the three variables described above. Previous work suggested that this relationship was linear, and analysis of both the neutron and muon count rates individually will indicate the relationship's true functional form across these variables [6]. The result of this analysis will define a mathematical relationship between the neutron and muon count rates and their constituent variables, elevation, latitude, and area type. Because of the random nature of radiation detection, all these relationships described affect the average count rate of the particles in each detector, which makes the method of calculating averages from the measured data consequential. Therefore, data were binned across the three variables before an average was calculated: first by its area type, then by its latitude with bin widths of 0.1 degrees, and finally be elevation with bin widths of 30 m. Since these measurements follow Poisson processes, variances were calculated in relation to measurements' total counts. Therefore, standard deviations, σ, presented with count rate data were estimated as $\frac{\sqrt{\boldsymbol{rt}}}{\boldsymbol{t}}$, where $\boldsymbol{r}$ represents a measurement's overall count rate in s^{-1} and $\boldsymbol{t}$ is the measurement time.

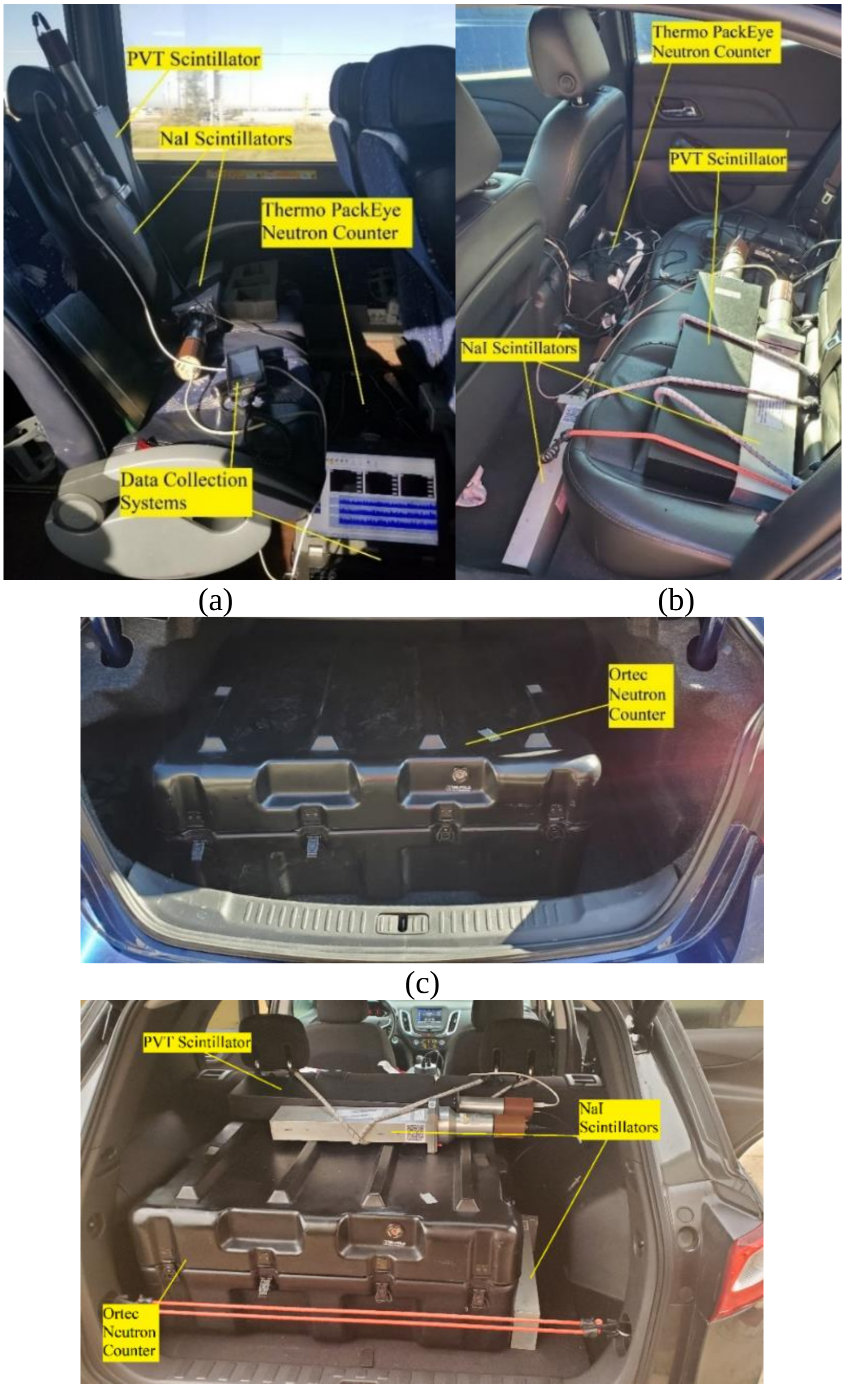

(a) (b)

(c)

(d)

Figure 4-2. Labelled photos showing the detectors set up in a charter bus for measurements on the College Station/Los Alamos road trip (a), in a sedan's cabin (b) and trunk (c) for mobile search type measurements (where the Thermo backpack was only used for one of them), and in an SUV's trunk for measurements during the College Station/Ann Arbor road trip (d).

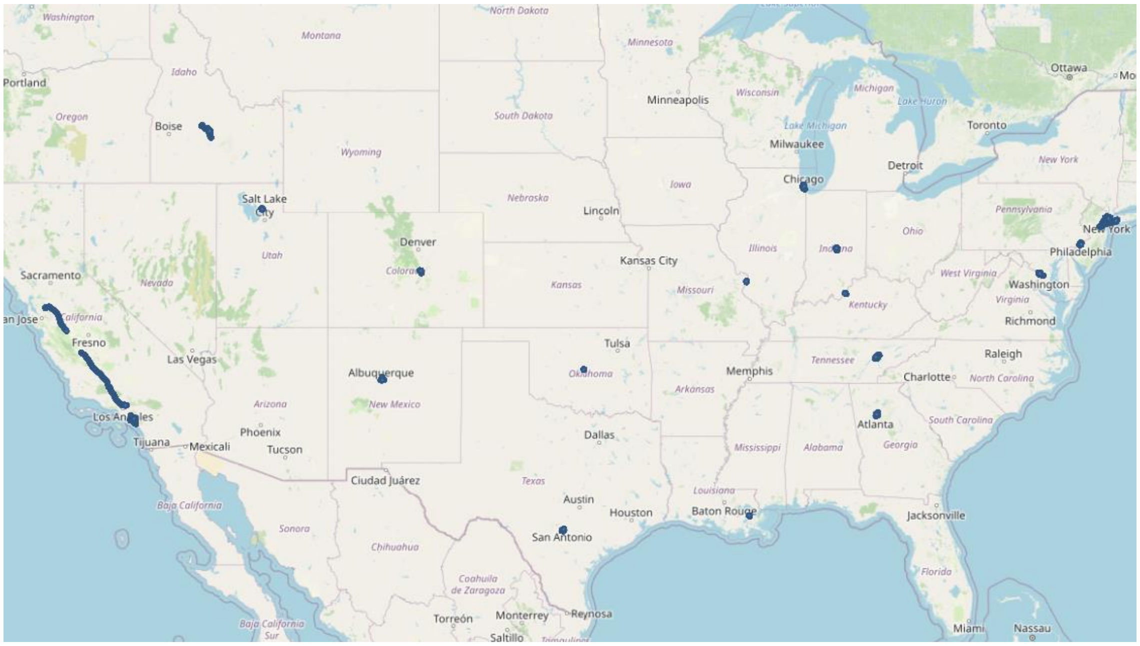

Figure 4-3. Map of locations where neutron and muon data were collected by RSL during operations between 2013 and 2017**.**

To better confirm the behavior of the above analysis, their results were compared against simulations using FLUKA, a Monte Carlo simulation code maintained by CERN [14,15]. While it was initially designed for simulating particle accelerator applications, FLUKA has a built-in cosmic ray source and an auxiliary “atmloc” program to build geometry representing the Earth’s atmosphere at a given location. This enables the calculation of secondary cosmic particles throughout the atmosphere and at the Earth’s surface. For this analysis, an additional surface feature was placed in each of these generated geometries to represent the elevation of a measured location. The neutron and muon currents across that additional feature were calculated using USRBDX tallies, which are normalized to the number of simulated primary particles. Each calculated current’s standard deviation, σ, was estimated using FLUKA’s reported standard error from three runs (or “cycles”) of each simulation. Simulations were completed for each urban area and a selection of locations along the Los Alamos and Ann Arbor road trip routes, and their results were compared against the collective behavior of the measured data from those locations. The additional locations measured by RAP teams and RSL were not simulated because their measurement methodologies were not as strictly controlled. Geomagnetic and geophysical data for each simulated location is listed in Table 4-2. That table also includes each location's geomagnetic rigidity which represents the horizontal strength of the Earth's magnetic field and acts as a shield against the primary cosmic particles. These rigidity values were calculated using a tool that applies the MAGNETOCOSMICS package of the Geant4 simulation code [16,17].

Table 4-2. Information on each location for which the neutron and muon currents were calculated in FLUKA.

			Geophysical			Geomagnetic		
City	State	Year	Latitude [degrees]	Longitude [degrees]	Elevation [m]	Latitude [degrees]	Longitude [degrees]	Rigidity [GV]
Little Rock	AR	2021	34.73	-92.27	102	43.29	-22.31	3.49
West Memphis	AR	2021	35.15	-90.18	64	43.84	-19.98	3.37
Cairo	IL	2021	37.01	-89.18	96	45.75	-19.02	2.91
Effingham	IL	2021	39.12	-88.55	180	47.88	-18.5	2.64
Indianapolis	IN	2021	39.79	-86.15	218	48.66	-15.77	2.43
Warsaw	IN	2021	41.24	-85.85	251	50.12	-15.55	2.12
Ann Arbor	MI	2021	42.27	-83.73	256	51.24	-13.14	1.96
Marshall	MI	2021	42.27	-84.95	280	51.19	-14.59	1.93
Albuquerque	NM	2019	35.11	-106.63	1619	42.58	-38.46	3.96
Clovis	NM	2019	34.40	-103.21	1301	42.22	-34.56	3.94
Hobbs	NM	2019	32.70	-103.14	1104	40.54	-34.23	4.32
Santa Fe	NM	2019	35.69	-105.94	2194	43.22	-37.8	3.82
Abilene	TX	2019	32.45	-99.73	524	40.58	-30.44	4.21
Austin	TX	2020	30.27	-97.73	149	38.53	-27.92	4.58
College Station	TX	2020	30.63	-96.33	103	38.99	-26.42	4.45
Dallas	TX	2020	32.78	-96.81	131	41.09	-27.19	4.08
Houston	TX	2019	29.75	-95.36	32	38.24	-25.29	4.63
Lubbock	TX	2019	33.58	-101.86	976	41.52	-32.94	4.11
San Antonio	TX	2020	29.42	-98.49	198	37.64	-28.66	4.87
Texarkana	TX	2021	33.44	-94.06	91	41.9	-24.19	3.83

4.3. Results and Analysis

A plot of the neutron count rates versus the muon count rates based on urbanization category are as shown in Figure 4-4, and the data came from the NaI scintillator in the “looking up” orientation and the Ortec neutron counter. This specific combination of detectors was selected because its sample size was much larger than from any other combination (from the Thermo Packeye neutron counter, the NaI scintillator in the "looking out" orientation, and the PVT scintillator). Additionally, these other detector combinations showed results similar to Figure 4-4 that differed by some constant (depending on detector characteristic), which would make their analysis somewhat redundant. While the data in Figure 4-4 appear linear above 10 muon counts per second, their shape at low count rates suggest a linear fit is not valid. As mentioned above, analysis of the constituent neutron and muon count rates is necessary to understand the true functional form of this relationship, and that analysis looked at these count rates as functions of elevation and latitude.

The neutron and muon count rates as functions of elevation (again, based on their urbanization category) are shown in Figure 4-5. Exponential fits are applied to each count rates' data that were not from urban areas or parking garages, and their R^2 values indicate both fits are strong (0.98 for muons and 0.80 for neutrons). The urban and parking garage data that appear at elevations between 0 m and 300 m were excluded from these fits as a distinct decrease in their count rates occurred, which was the result of the shielding introduced by building materials in those areas. A linear relationship appears plausible for the neutron count rate data, particularly due to deviations from the exponential equation at high elevations. However, literature indicates that such a relationship would not apply. Not only do previous findings indicate an exponential increase with increasing elevation, but the same is indicated in theoretical approximations [9]. In this case, the neutron source could be approximated as a disc with infinite radius with the detector some distance from it. If air were approximated as a homogeneous shielding medium, the neutron flux would vary with that distance by the exponential integral function, which results in an exponential function for these distances [18].

A similar plot of the neutron and muon count rates as functions of latitude are shown in Figure 4-6. In this case, linear fits were applied to data that were not from urban areas or parking garages, but the data for these fits were limited further due to covariance between latitude and elevation. The data that appear in yellow in Figure 4-6 had a strong linear relationship between elevation and latitude (R^2 = 0.90), which can be observed in Figure 4-7. The R^2 values of the linear fits with latitude on the remaining neutron and muon data indicate that they are weak on their own (0.36 for muons and 0.09 for neutrons). However, these fits are valid despite that. This is because the R^2 value can be interpreted as the percentage of data's variance explained by the equation of fit. Following this, a fit with an R^2 value of 1 would indicate that the fit explains 100% of the data's variance, and decreasing values indicate that more of the data's variance is the result of some other source (either another variable or random chance). Considering that, the linear fits with latitude are significant despite their smaller R^2 values because those values suggest the fits account for some amount of variance that may not be explained by the exponential fits with elevation.

The results of the FLUKA simulations confirm these behaviors. Figure 4-8 shows the neutron and muon currents at each location as functions of elevation, which have strong exponential fits (R^2 values of 0.92 for muons and 0.98 for neutrons). Similarly, Figure 4-9 shows those currents as functions of latitude, and the data that did not have a covariance with elevation had strong linear fits (R^2 values of 0.88 for muons and 0.63 for neutrons). These results are important because the fits on the FLUKA data match the functional forms implied by previous work while the data's overall shapes match that of the measured data for the corresponding locations. This indicates that the equations of fit selected for the measured data in Figure 4-5 and Figure 4-6 (with exponential and linear forms, respectively) are appropriate.

Figure 4-5 and Figure 4-8 show that the measured and calculated neutron data appear to deviate from the exponential fits at high elevations (> 2000 m). The primary explanation for this is the fact that elevation is used as a proxy for the thickness and density of the atmosphere that shields these particles. While atmospheric thickness is naturally linear with elevation, its density, frequently described as air pressure, is not. Literature suggests that the true relationship between elevation and air pressure is $(760\ \text{mm Hg}) \cdot (1 - 2.25577 \cdot 10^{-5} x)^{5.25588}$, where x is the elevation above sea level in meters [10,11]. A linear approximation is applicable for this function, but only for a range of 2000 m (i.e. between sea level and 2000 m or between 500 m and 2500 m). This linear approximation would underestimate the air pressure outside this range, which in turn would make elevation's effect on the muon and neutron count rates appear stronger than reality. The measured and simulated neutron data are shown in Figure 4-10 as a function of estimated air pressure instead of elevation, where the pressure was calculated using the above function. Comparing these data to the corresponding neutron plots in Figure 4-5 and Figure 4-8 show that the exponential fits for both are stronger than those with elevation (the R^2 values increased). Despite this, elevation was still used for this analysis (instead of replacing it with air pressure) because search operations are unlikely to occur at elevations above 2000 m, and thus converting to air pressure would be an unnecessary calculation for operators when elevation is sufficient.

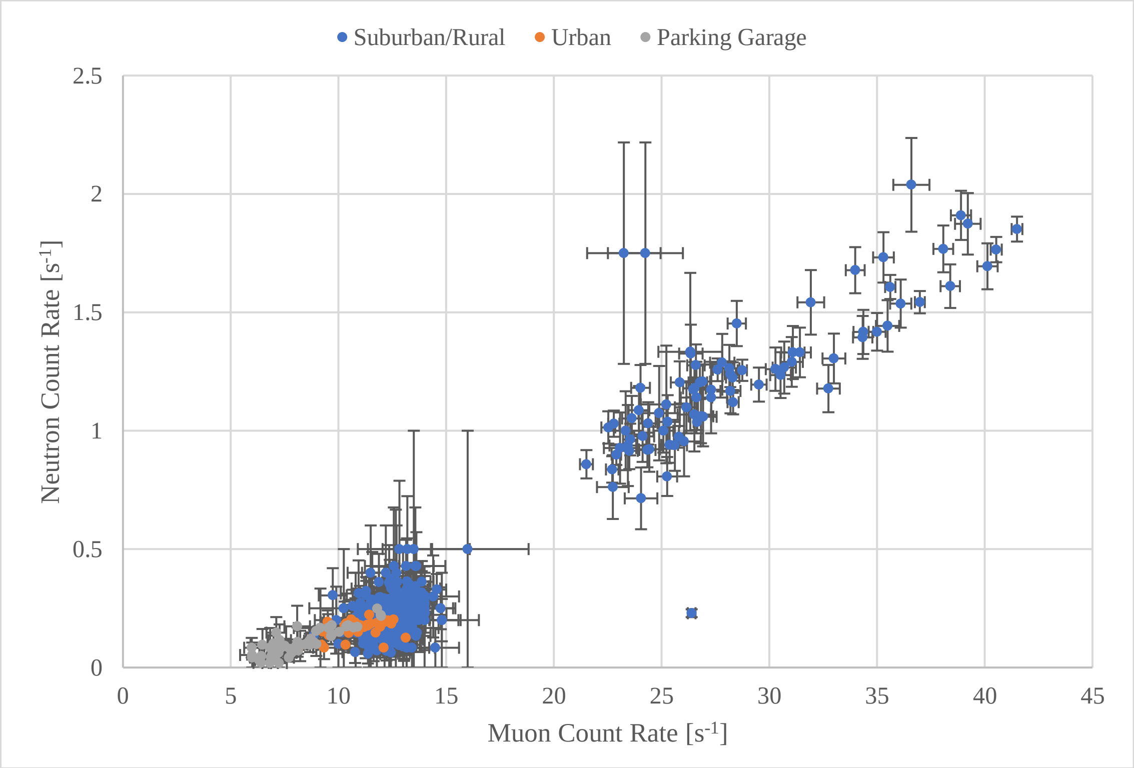

Figure 4-4. Plot of neutron count rates versus muon count rates measured by the authors. Data are separated by whether they were collected in urban areas (orange), parking garages (grey), and all other areas (blue). 1-σ error bars are shown.

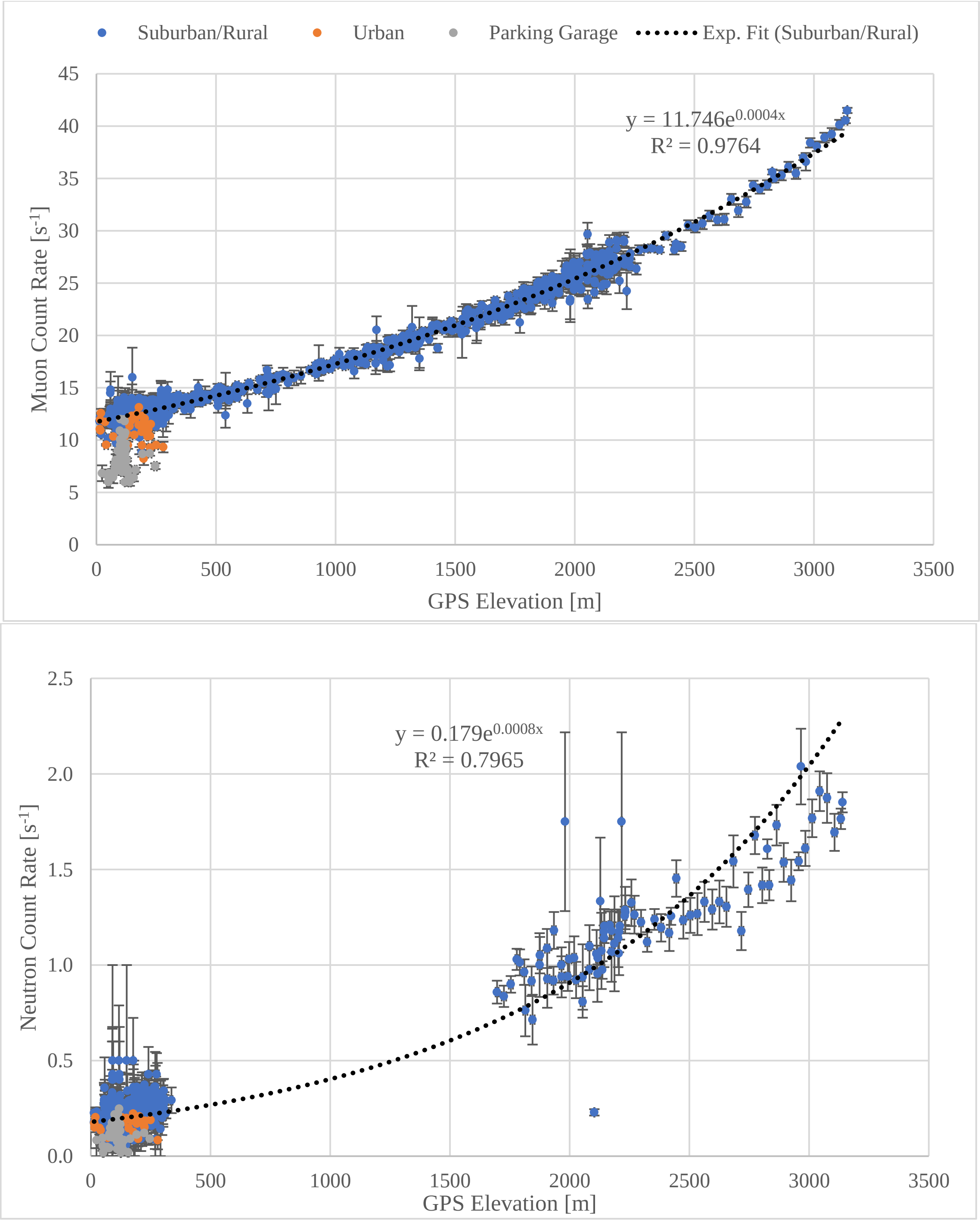

Figure 4-5. Plot of muon (top) and neutron (bottom) count rates versus elevation measured by the authors separated by area type. Data from urban areas are shown in orange, parking garages in grey, and all other data in blue, and the exponential fits are applied to the latter. 1-σ error bars are shown. The gap in neutron data between 300 m and 1700 m is the result of lack of ability to operate the neutron detector for a period during the College Station/Los Alamos trip.

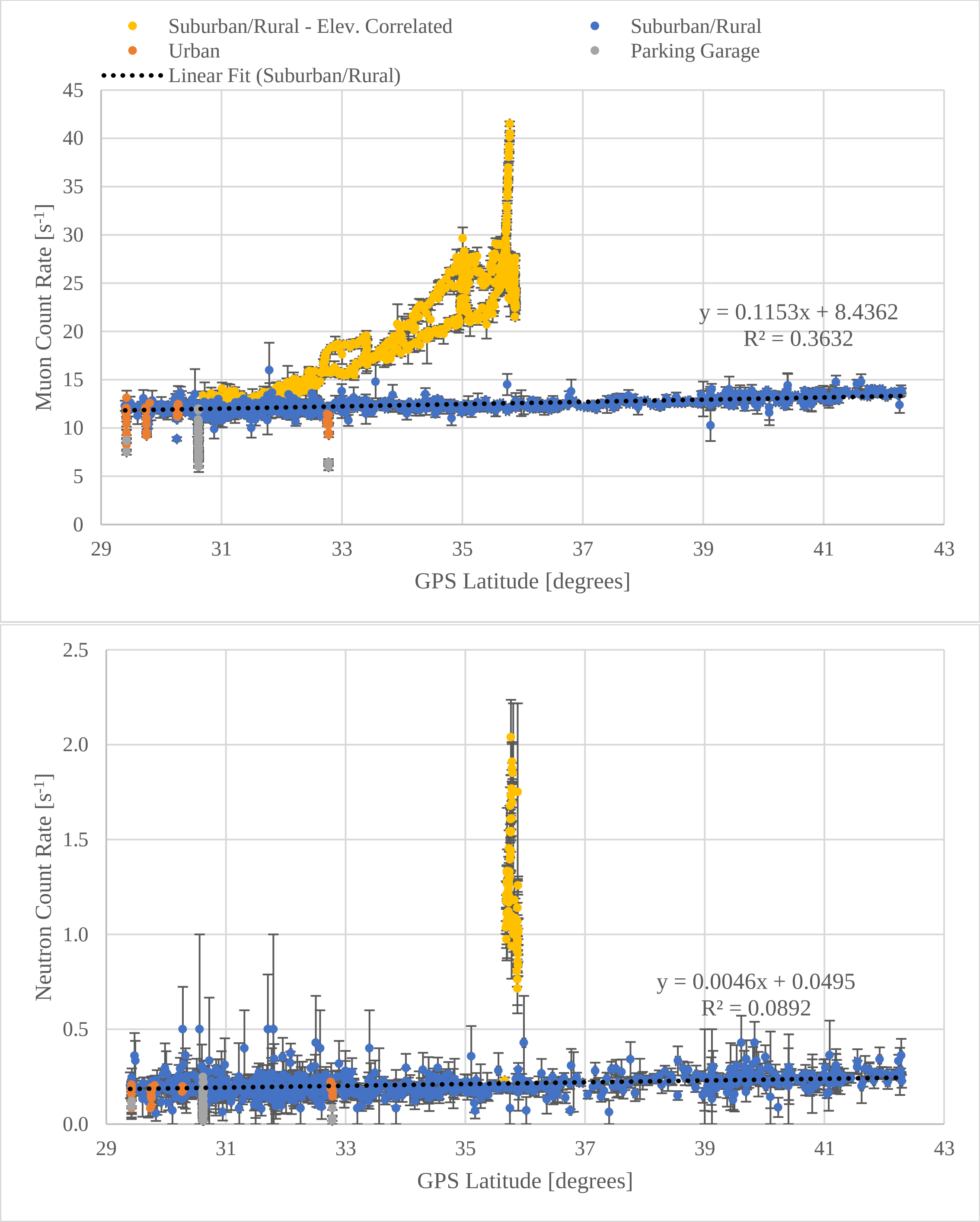

Figure 4-6. Plot of muon (top) and neutron (bottom) count rates versus GPS latitude measured by the authors separated by area type. Data from urban areas are shown in orange, parking garages in grey, and all other data that were not correlated with elevation in blue. The data in yellow are from the College Station/Los Alamos trip and have a strong correlation between latitude and elevation. 1-σ error bars are shown.

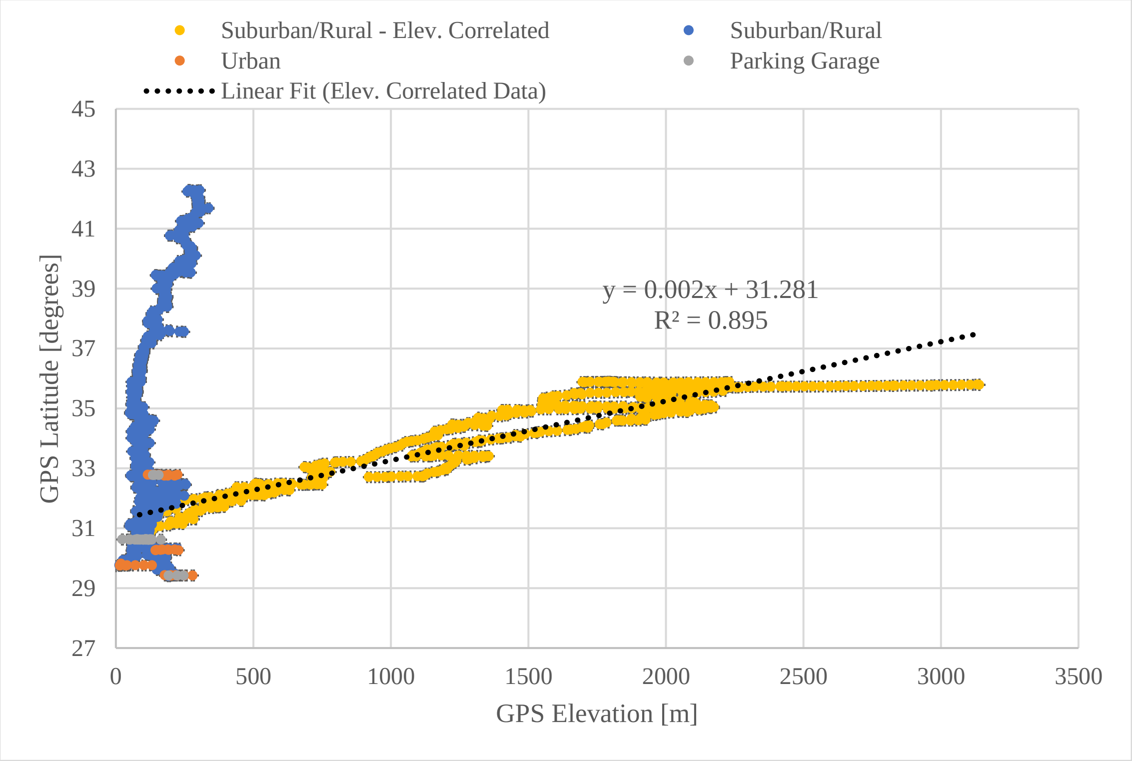

Figure 4-7. Plot of GPS latitude versus GPS Elevation measured by the authors separated by area type. Data from urban areas are shown in orange, parking garages in grey, and all other data that were not correlated with elevation in blue. The data in yellow are from the College Station/Los Alamos trip and have a strong correlation between latitude and elevation. 1-σ error bars are shown.

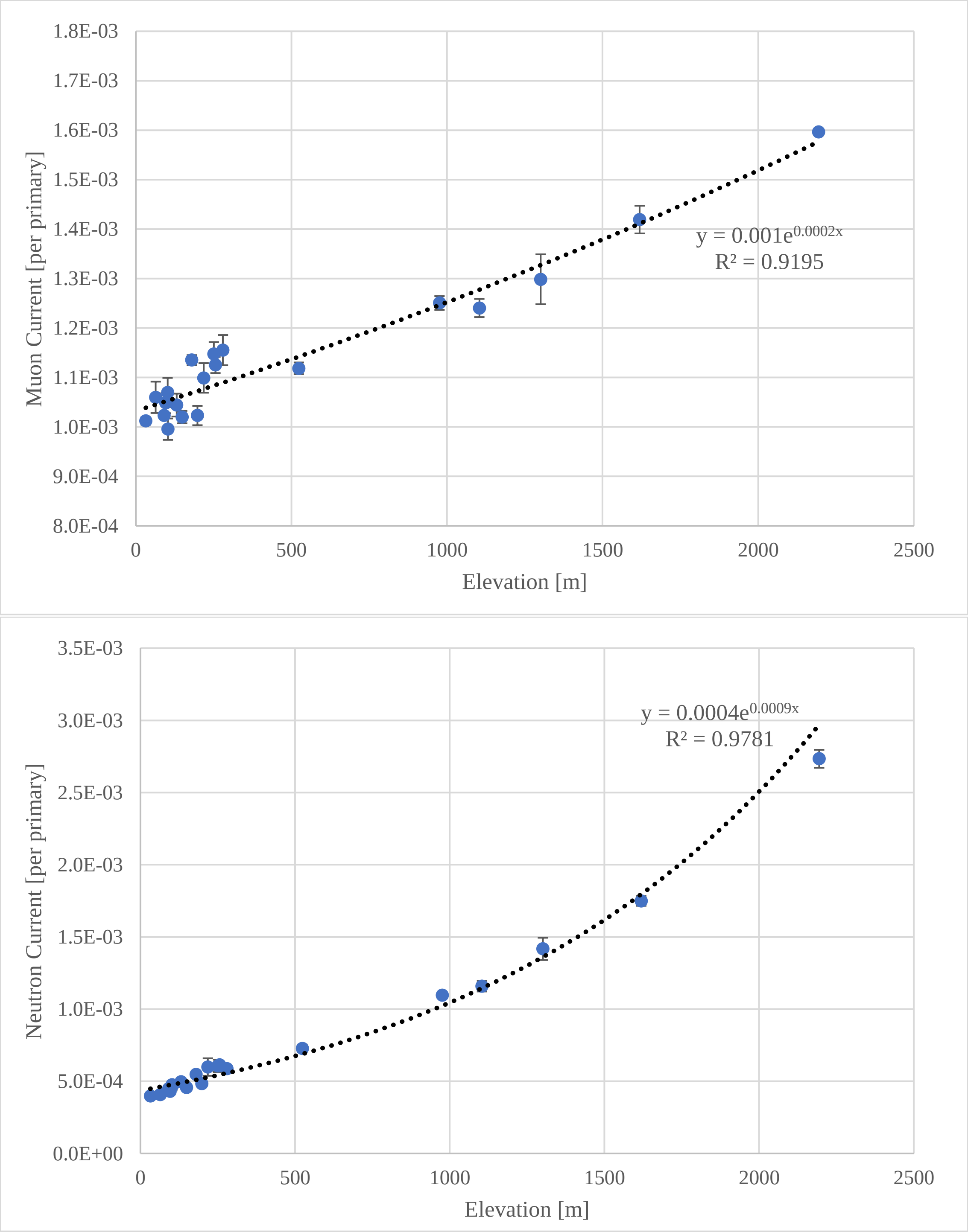

Figure 4-8. Plots of muon (top) and neutron (bottom) currents versus elevation calculated using FLUKA with exponential fits. Each point represents a location where the authors measured data. 1-σ error bars are shown.

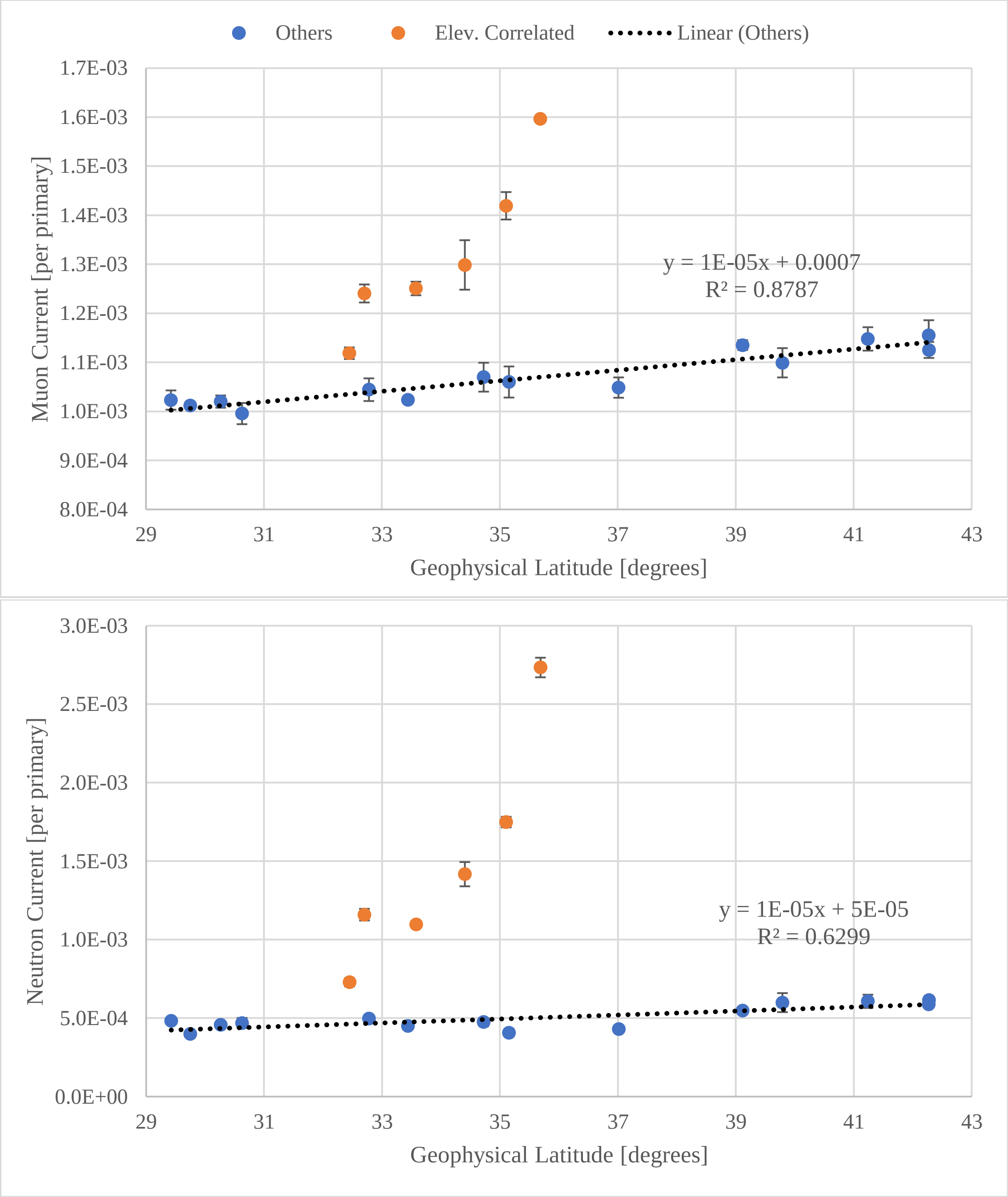

Figure 4-9. Plots of muon (top) and neutron (bottom) currents versus geophysical latitude calculated using FLUKA with linear fits on data that did not have a strong covariance with elevation (blue). Each point represents a location where the authors measured data. 1-σ error bars are shown. Data shown in orange came from locations that increased in elevation while also increasing in latitude (i.e. the orange point at 32.5 degrees occurred at an elevation of 500 m while the orange point at 35.5 degrees occurred at an elevation of 2200 m).

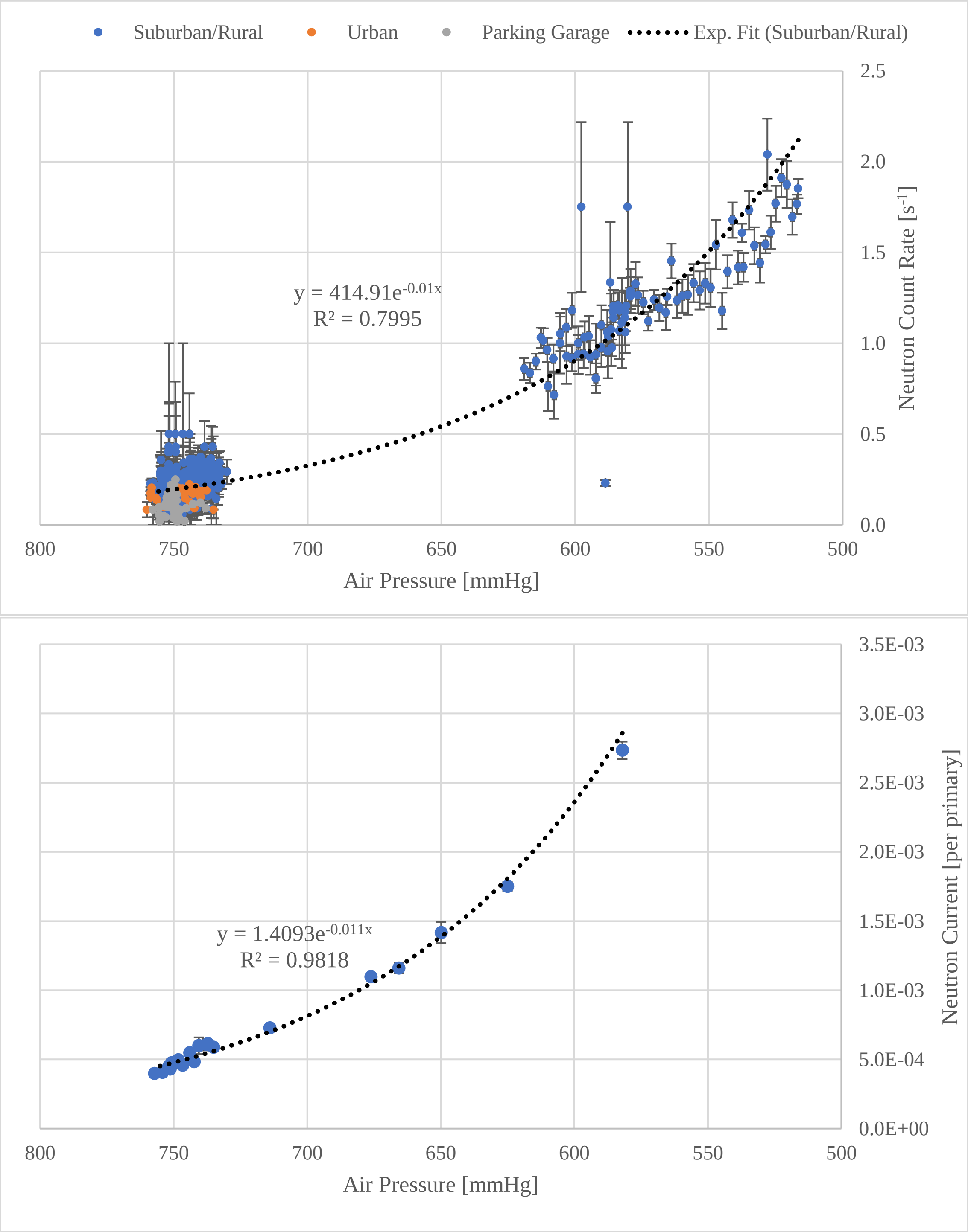

Figure 4-10. Plots of measured neutron count rate (top) and FLUKA-calculated neutron current (bottom) as functions of air pressure. 1-σ error bars are shown.

With these fits in mind, the functional form of the neutron/muon relationship can be derived. The neutron count rate, n, and muon count rate, m, as functions of elevation, x, and latitude, y, are shown in Eq. 4.1 and Eq. 4.2, respectively. These forms only apply to latitudes between 25 and 45 degrees North or South because literature shows the flux variance is linear in these regions. At higher latitudes, a constant value applies, and a quadratic function applies between 25 degrees North and 25 degrees South (although a constant approximation may also apply) [9]. These two equations can be related to each other through substitution. First, Eq. 4.1 is inverted to become elevation as a function of muon count rate and latitude. No singularity occurs because neither constant in Eq. 4.1 can be zero, nor can y be zero as discussed above. This function will be substituted for elevation in Eq. 4.2, where elevation was selected as the substitution variable because it is had the largest effect on the data. Performing that substitution yields the neutron count rate as a function of latitude and muon count rate as shown in Eq. 4.3 (after simplifying).

While Eq 4.3 represents the most accurate form of this function, it is difficult to model without using nonlinear methods. One meaningful approximation of this function would be to consider the constants b and g as zero. This approximation is only valid because the range of latitude does not include zero, but it has the downside of increasing the magnitude of constants A and D since latitude's effect follows an increasing linear function. However, this approximation provides the ability to linearize the function, which enables the application of linear regression's more rigorous statistical tests. As a result, the model for the neutron/muon-latitude relationship becomes a power law function for both variables.

$$m(x,y) = (Ay + b)e^{cx} \tag{4.1}$$

$$n(x,y) = (Dy + g)e^{kx} \tag{4.2}$$

Where:

x = elevation above sea level [m]
y = geophysical latitude [degrees]
$m(x)$ = muon count rate [s^{-1}]
$n(x)$ = neutron count rate [s^{-1}]
A, D = constants [s^{-1} $\mathrm{degrees}^{-1}$]
b, g = constants [s^{-1}]
c, k = constants [m^{-1}]

$$m(x,y) = (Ay + b)e^{cx} \tag{4.1}$$

$$\frac{m}{(Ay + b)} = e^{cx}$$

$$cx = \ln\left(\frac{m}{Ay + b}\right)$$

$$x = \frac{\ln\left(\frac{m}{Ay + b}\right)}{c} \qquad (c > 0)$$

$$n(x,y) = (Dy + g)e^{kx} \tag{4.2}$$

$$n(m,y) = (Dy + g)e^{k\left(\frac{\ln\left(\frac{m}{Ay+b}\right)}{c}\right)}$$

$$n(m,y) = (Dy + g)e^{\frac{k}{c}\left(\ln\left(\frac{m}{Ay+b}\right)\right)}$$

$$n(m,y) = (Dy + g)\left(e^{\ln\left(\frac{m}{Ay+b}\right)}\right)^{\frac{k}{c}}$$

$$n(m,y) = (Dy + g)\left(\frac{m}{Ay + b}\right)^{\frac{k}{c}}$$

$$n(m,y) = \frac{(Dy+g)}{(Ay+b)^{k/c}} m^{k/c} \tag{4.3}$$

$$n(m,y) \approx \frac{Dy}{(Ay)^{k/c}} m^{k/c} \tag{4.4}$$

Since two variables are involved, a multiple regression is required, which is more complicated to display with the data. The results of the regression on the authors' measured and simulated data are shown in Table 4-3 using the form $n(m,y) = Ay^b m^c$. Those regressions suggest that latitude may not be a significant variable in this relationship, namely through the large p-value for the latitude coefficient from the regression on the measured data. In regression analysis, the p-value indicates the "false positive" probability of rejecting the null hypothesis that the coefficient is zero. A coefficient and its corresponding variable are considered significant if that probability is sufficiently low. That threshold is selected to an investigator's preference, but a common value of 0.05 was used. As such, the p-value of 0.167 for the latitude coefficient indicates it is not significant. Therefore, if latitude is not a significant variable, then a simple power law fit is valid. Analysis of the data from RSL and RAP will help in determining if this is the case.

Plots of the neutron count rate versus the muon count rate from RAP's and RSL's data are shown in Figure 4-11. These data have a similar shape as those measured by the authors as shown in Figure 4-4, which means similar regressions were applied. The results of those regressions are displayed in Table 4-4. In this case, the regression on RAP's data suggests the latitude variable is significant where that on RSL's data suggests it is not. A deeper look into RAP's data indicates why this occurred: RAP's measurements produced a strong inverse correlation with latitude. Measurements in the Chicago area had a low elevation (approximately 150 m) but a high latitude (approximately 40 degrees N), but similar measurements in the Albuquerque area had a range of high elevations (1500 m to 3200 m) but a low latitude (approximately 35 degrees N). This covariance likely caused the relatively large negative value of b shown in Table 4-4. This sampling issue was not present in RSL's data because the locations they measured provided data from a broad range of elevations and latitudes with minimal covariance. All of these aspects would indicate that latitude produces a negligible effect on the neutron/muon relationship and thus can be considered constant.

Table 4-3. Data on multiple regressions of the author's measured and calculated neutron data as functions of the muon and latitude data. A variable is considered not significant if its regression coefficient has a P-value greater than 0.05.

	Regression coefficients ($n = Ay^bm^c$)					Regression statistics	
Data Source		b	P-value, b	c	P-value, c	R^2	Observations
Measured	7.58E-3	0.130	0.167	2.040	0.000	0.795	972
Simulated	1.72E11	-0.819	0.001	4.464	3.21E-14	0.965	20

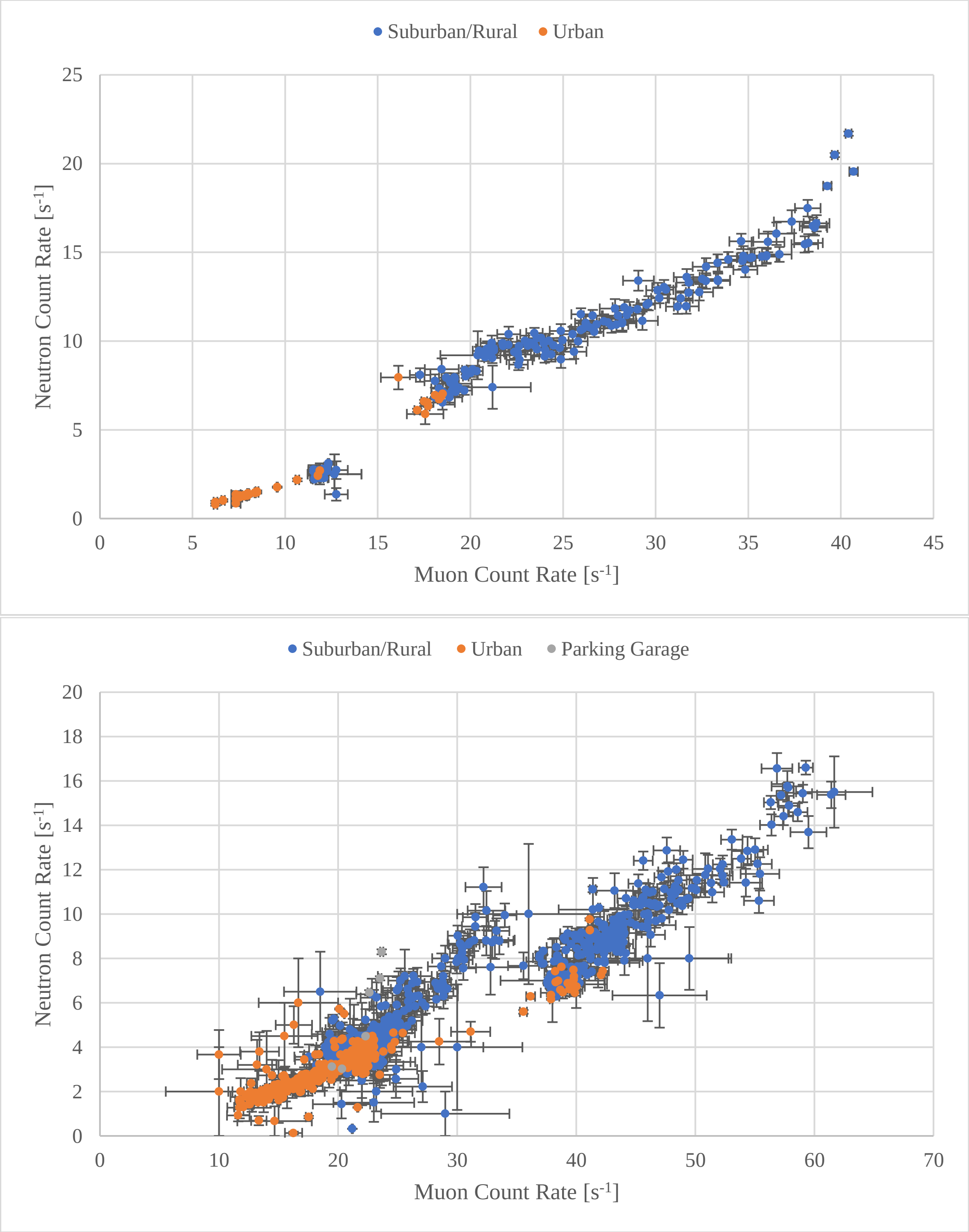

Figure 4-11. Plot of neutron count rates versus muon count rates measured by RAP teams (top) and RSL (bottom). Data are separated by whether they were collected in urban areas (orange), parking garages (grey), and all other areas (blue). 1-σ error bars are shown.

Table 4-4. Data on multiple regressions of RAP's and RSL's neutron data as functions of their muon and latitude data. A variable is considered not significant if its regression coefficient has a P-value greater than 0.05.

	Regression coefficients ($n = Ay^b m^c$)					Regression statistics	
Data Source	A	b	P-value, b	c	P-value, c	R^2	Observations
RAP	2.86E4	-3.333	1.03E-53	1.222	0.000	0.987	232
RSL	4.66E-2	0.056	0.405	1.350	0.000	0.844	1059

This result is important when considering the approximation made when deriving the model. Specifically, the approximation to obtain Eq. 4.4 would only serve to increase the effect of latitude in the model because, as mentioned above, latitude is an increasing linear effect on the neutron and muon count rates. Assuming those y-intercepts were zero would increase the magnitude of the constants A and D in Eq. 4.4 compared to those in Eq. 4.3, thus increasing the strength of latitude's effect in the model. Therefore, if the data indicated that latitude is not significant in a model which augmented its effect (as in Eq. 4.4), then the data would likely make the same indication if the more accurate model were applied (using Eq. 4.3).

Considering latitude as a constant would result in small changes to Eq. 4.3, which consist of reducing the expressions $Ay + b$ and $Dy + g$ to constants A^* and D^*, respectively. This change would result in the single variable power law relationship shown in Eq. 4.5. These functions are much simpler to model and display graphically as can be observed for each data set in Figure 4-12, Figure 4-13, and Figure 4-14. When comparing the equations of fit shown in these figures to those in Table 4-3 and Table 4-4, the small change in the regression's power coefficient confirms that latitude had a negligible effect, and that this simplified function is appropriate. It should be noted that the fits in Figures 4-12, 4-13, and 4-14 are only on the data that were not from urban areas or parking garages, and the reason for that will become apparent with discussion on the final variable, area type.

$$n(m,y) = \frac{Dy + g}{(Ay + b)^{k/c}} m^{k/c} \tag{4.3}$$

$$n(m) = \frac{D^*}{(A^*)^{k/c}} m^{k/c} \tag{4.5}$$

Where:

y = geophysical latitude [degrees]
m = muon count rate [s^{-1}]
n = neutron count rate [s^{-1}]
A, D = constants [s^{-1} degrees^{-1}]
g, b = constants [s^{-1}]
$A^*, D^* \approx Ay + b, Dy + g$ = constants [s^{-1}]; correlate to muon and neutron count rates at sea level, respectively
c, k = constants [m^{-1}]

Taking a measurement's area type into consideration was much more difficult than elevation or latitude. As mentioned previously, this meant to account for the amount of additional shielding material present around the detectors, which would be an additional cause of change in both count rates. Theoretically, this would add another exponential factor to Eq. 4.1 and Eq. 4.2 that would depend on the thickness of material nearby. However, this is virtually impossible to quantify for these constantly moving detectors, even on an average basis, which is why the data were separated into the three categories:

parking garage, urban, and all others. The final category is a combination of data from suburban and rural areas since the data indicated that the surrounding infrastructure of the former was not significant enough to have an effect on the detection of those downward travelling particles. Conversely (an intuitively), the other two categories did have a notable effect on both count rates because of those excess materials either next to or above the detectors, which can be observed in Figure 4-5 as neutron and muon count rates were decreased in urban areas and decreased further in parking garages as the two areas' shielding environments became more extreme. This leaves one question: whether the changes observed in Figure 4-5 prompt an adjustment to Eq. 4.5 and thus, a different, likely more complicated, function to represent the relationship between the neutron and muon count rates.

Observing the power law fits on the author's data from suburban and rural areas in Figures 4-12, 4-13, and 4-14 provide the answer to that question. The extrapolated equation of fit indicates that the data from urban areas or parking garages adhere to that power law function as muon count rates decrease due to the buildings' shielding. This is further demonstrated with a power law fit on all the author's data as shown in Figure 4-15 as its coefficients were less than 2% different than those for the fit in Figure 4-12. These results occurred in the other data sets as well: RAP's extrapolated fit is shown in Figure 4-13, and the power law fit on all their data shown in Figure 4-16 has coefficients that are less than 2% different than those in Figure 4-16. The same occurred for RSL's data in Figure 4-14 and Figure 4-18, respectively, where the coefficients of fit on all their data (Figure 4-18) were approximately 7% different than those for the extrapolated data (Figure 4-17) With these fits, the data do appear to deviate from the data at high muon count rates (> 30 s^{-1}), particularly in the authors' and the RAP teams' data. This is likely similar to the effect observed at high elevations in Figure 4-5, where the deviation was a result of air pressure as observed in Figure 4-10. These data came from very high elevations, particularly greater than 2000 m, where, as mentioned before, a linear approximation between elevation and air pressure was less applicable. However, correcting for this would be more difficult than the correction in Figure 4-10: while using the count rate versus pressure relationships in Eq. 4.1 and Eq. 4.2 would change Eq. 4.5 in theory, the resulting regression equation would be the same because the functional form of Eq. 4.5 (a power law function) would not change.

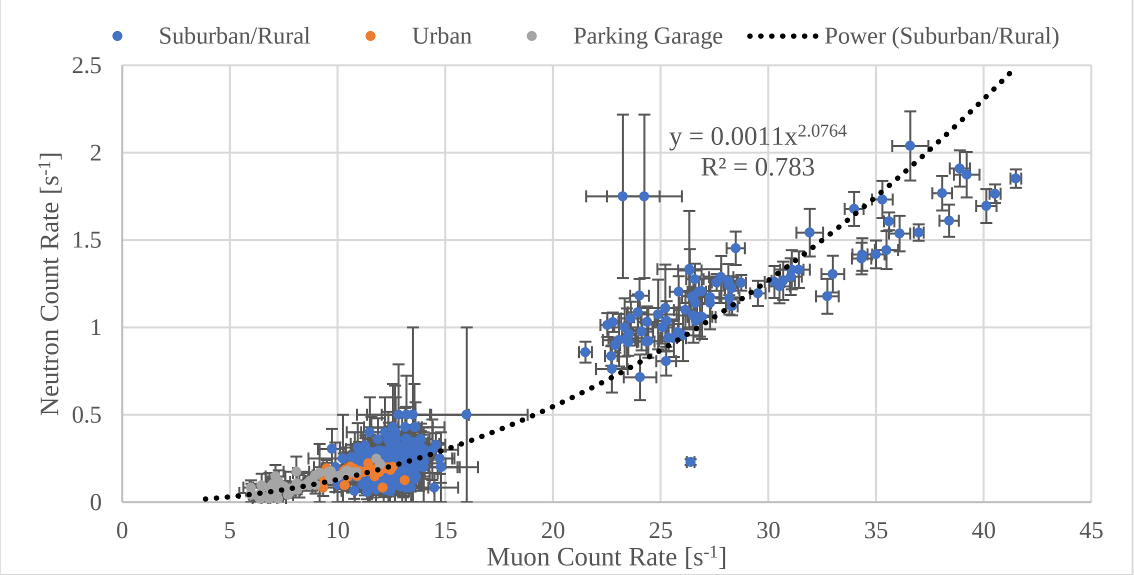

Figure 4-12. Plot of neutron count rates versus muon count rates measured by the authors with an extrapolated power law fit. Data are separated by whether they were collected in urban areas (orange), parking garages (grey), and all other areas (blue). Power law fits are applied to data from all other areas. 1-σ error bars are shown.

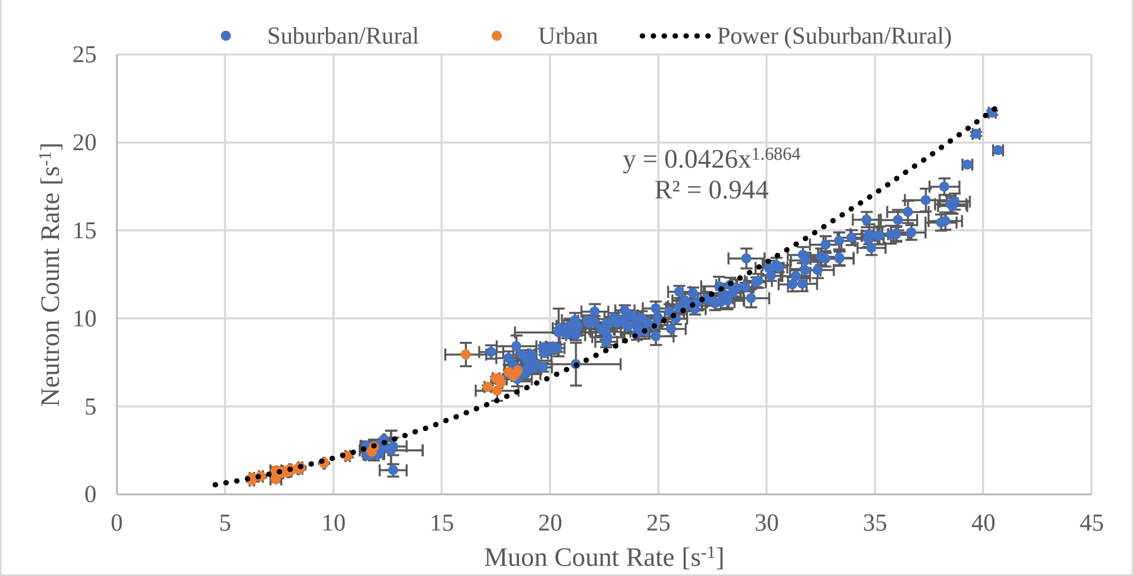

Figure 4-13. Plot of neutron count rates versus muon count rates measured by the RAP teams with an extrapolated power law fit. Data are separated by whether they were collected in urban areas (orange) and all other areas (blue). Power law fits are applied to data from all other areas. 1-σ error bars are shown.

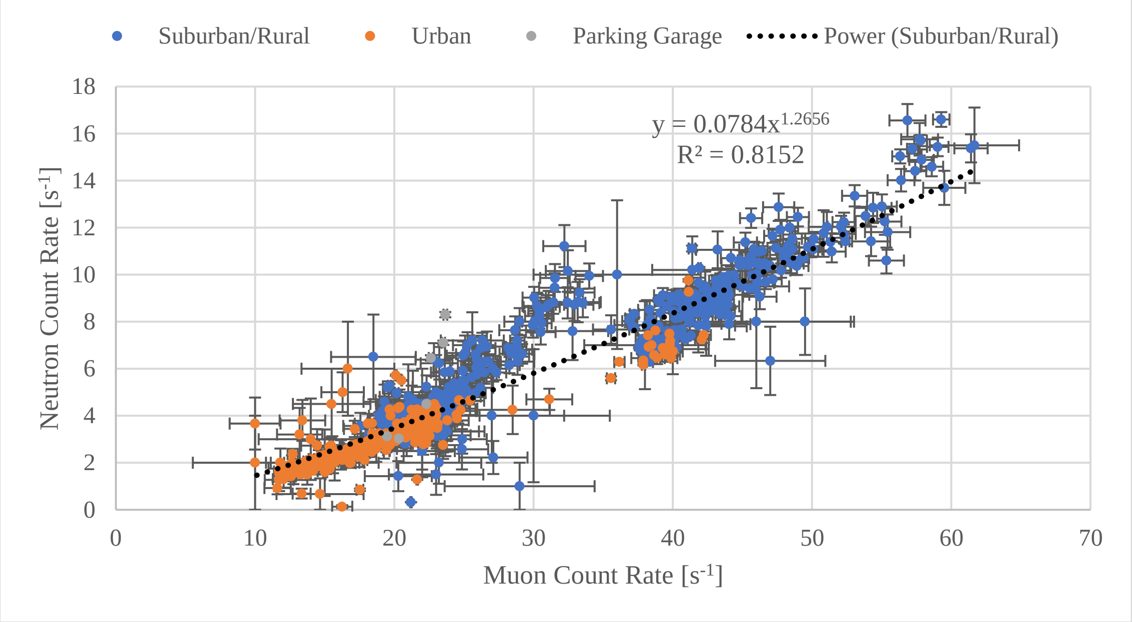

Figure 4-14. Plot of neutron count rates versus muon count rates measured by RSL with an extrapolated power law fit. Data are separated by whether they were collected in urban areas (orange), parking garages (grey), and all other areas (blue). Power law fits are applied to data from all other areas. 1-σ error bars are shown.

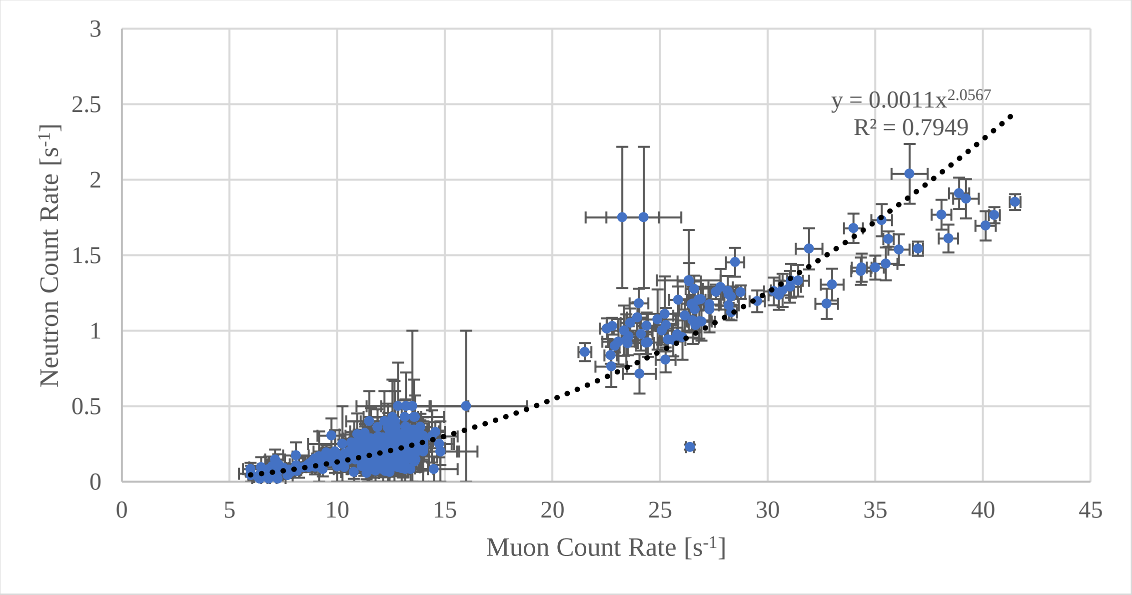

Figure 4-15. Plot of neutron count rates versus muon count rates measured by the authors with a power law fit on all data. 1-σ error bars are shown.

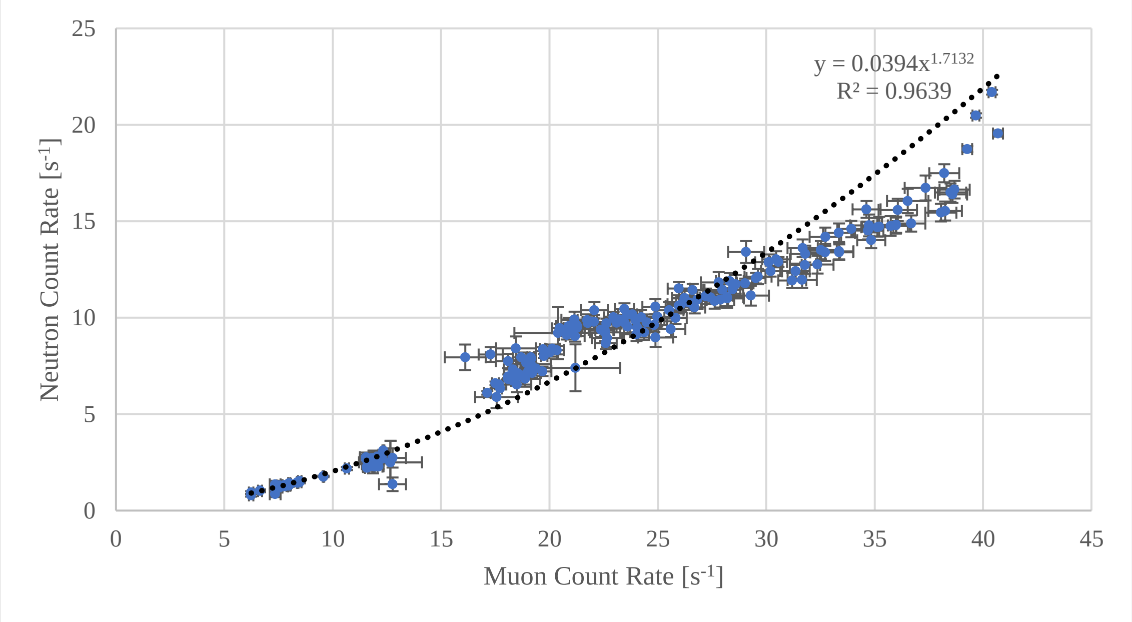

Figure 4-16. Plot of neutron count rates versus muon count rates measured by the RAP teams with a power law fit on all data. 1-σ error bars are shown.

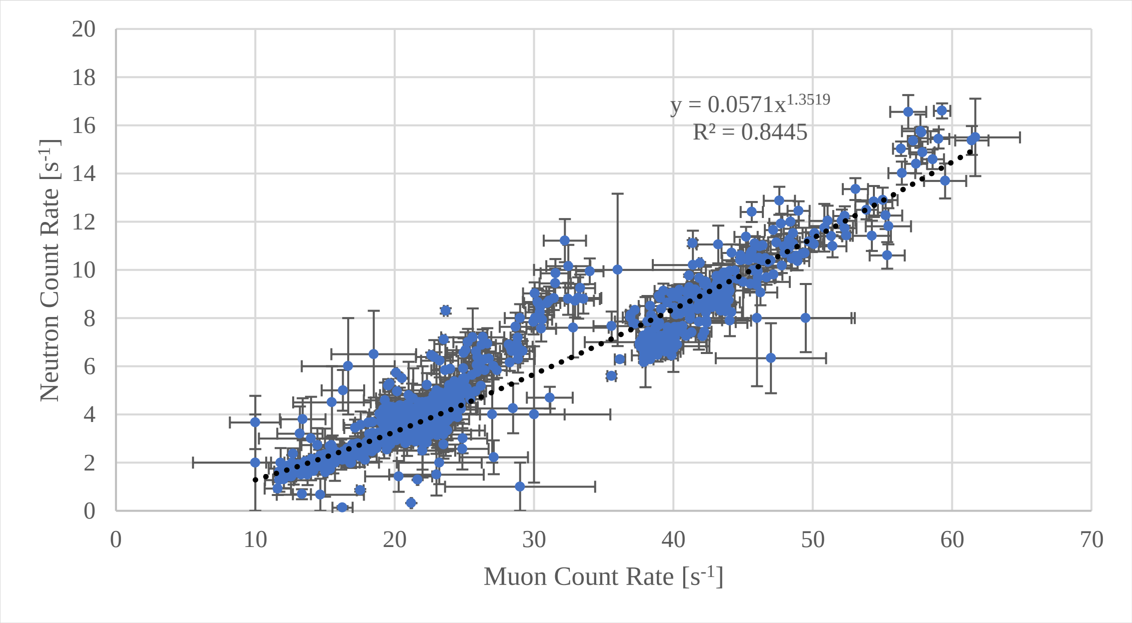

Figure 4-17. Plot of neutron count rates versus muon count rates measured by RSL with a power law fit. 1-σ error bars are shown.

The results of the above analysis show that the neutron and muon count rates have a strong power law relationship on an average basis. Therefore, if a mobile search system is able to measure muons, it can be used to estimate the average neutron count rate for background. This ability is important as that average neutron count rate is the basis of determining when the neutron detectors should produce an alarm. Making estimates of the average neutron count rate in relation to muon detection enables a dynamic neutron alarm metric, which would reduce false alarms and increase the detector's sensitivity to neutron-emitting materials. Future work will determine this relationship's effectiveness in producing neutron alarms when a source is present.

Unfortunately, these results show that the power law relationship is also dependent upon the configuration of detectors used in the mobile search system. While the relationship exists in all systems tested, each system's relationship has different coefficients. It is likely that the coefficients depend on a variety of characteristics of the constituent neutron and muon detectors, but more research is required to determine if and how those occur. Until that occurs, this relationship remains empirical, and mobile search operators that wish to apply such a relationship will need to make measurements with their own systems to determine the power law relationship's coefficients.

4.4. Conclusion

This work shows that a mobile search system's neutron count rate is related to its muon count rate by a power law function. These systems can measure the muon count rate using its gamma ray spectrometer, and its power law relationship with the neutron counter response holds regardless of elevation, latitude, and area type. While this relationship is empirical, it indicates the potential for such systems to estimate their background neutron count rate during mobile search operations. Additional work is required to generalize the power law relationship, and even more work is necessary to determine whether such an estimate of the background neutron count rate is applicable as a neutron alarm metric. The success of the latter would indicate that such an estimation method would make mobile search systems more sensitive to certain radiological materials.

4.5. References

1. "Beirut explosion: What we know so far." *BBC News*. 11 August 2020. Available at https://www.bbc.com/news/world-middle-east-53668493 (accessed 19 February 2021).
2. S.E. Rigby, T.J. Lodge, S. Alotaibi, et. al "Preliminary yield estimation of the 2020 Beirut explosion using video footage from social media." *Shock Waves* 30, 671-675 (2020). Available at https://doi.org/10.1007/s00193-020-00970-z (accessed 19 February 2021).
3. The Tennessean Staff. "Nashville bombing: What we know about downtown explosion on Christmas morning." *The Tennessean*. 25 December 2020 (updated 28 December 2020). Available at https://www.tennessean.com/story/news/local/2020/12/25/nashville-explosion-what-we-know-downtown-christmas-morning/4044934001/ (accessed 19 February 2021)

4. L. Wamsley. “What We Know So Far: A Timeline of Security Response at the Capitol on Jan. 6.” *NPR*. 15 January 2021. Available at https://www.npr.org/2021/01/15/956842958/what-we-know-so-far-a-timeline-of-security-at-the-capitol-on-january-6 (accessed 19 February 2021).
5. D. L. Upp, R. M. Keyser, Performance of a car-mounted neutron and gamma-ray monitoring system for illicit material detection, in: Proc. 45th INMM Annual Meeting Institute of Nuclear Materials Management, 2004.
6. J. N. Wagner, C. Marianno, and T. McCullough, “Parking Garage Measurements Indicating a Gamma Spectrometer-Neutron Counter Background Correlation,” *International Journal of Nuclear Security*, Vol. 6: No. 1, Article 6. 2020. Available at: https://trace.tennessee.edu/ijns/vol6/iss1/6/
7. J. N. Wagner and C. Marianno, “Identification of the Ambient Response Relationship in Neutron Counting and Scintillation Measurement Systems,” *Radiation Science and Technology*. Vol. 7, No. 1, 2021, pp. 7-14. doi: 10.11648/j.rst.20210701.12
8. J. F. Ziegler, “Terrestrial Cosmic Rays”, *IBM Journal of Research and Development*, 1996.
9. T. Brice and T. Hall, “Pressure Altitude Calculator.” National Weather Service. Available at https://www.weather.gov/epz/wxcalc_pressurealtitude (accessed 19 February 2021).

10. “Atmospheric Pressure vs. Elevation above Sea Level” The Engineering ToolBox. Available at https://www.engineeringtoolbox.com/air-altitude-pressure-d_462.html (accessed 19 February 2021)
11. AMETEK Inc. – ORTEC, “digiBASE 14-Pin PNT Tube Base with Integrated Bias Supply, Preamplifier, and MCA (with Digital Signal Processing) for NaI Spectroscopy,” available at https://www.ortec-online.com/-/media/ametekortec/brochures/digibase.pdf (accessed on 7 September 2020).
12. Thermo Fisher Scientific Inc., FHT 1377 PackEye – Radiation Detection Backpack, available at https://static.thermoscientific.com/images/D19393~.pdf (accessed on 29 December 2018).
13. T.T. Böhlen, F. Cerutti, M.P.W. Chin, A. Fassò, A. Ferrari, P.G. Ortega, A. Mairani, P.R. Sala, G. Smirnov and V. Vlachoudis, "The FLUKA Code: Developments and Challenges for High Energy and Medical Applications" *Nuclear Data Sheets* 120, 211-214 (2014)
14. A. Ferrari, P.R. Sala, A. Fasso`, and J. Ranft, "FLUKA: a multi-particle transport code" CERN-2005-10 (2005), INFN/TC_05/11, SLAC-R-773
15. “Cutoff Rigidity Calculator.” Nearfield Water Management Tools. Available at http://nearfld.com/util/rigidity.php (accessed on 19 February 2021).
16. L. Desorgher. “MAGNETOCOSMICS Software User Manual” 2004. University of Bern. Available at http://cosray.unibe.ch/~laurent/magnetocosmics/doc/magnetocosmics_sum.pdf (accessed 19 February 2021).

17. J.K. Shultis and R.E. Faw, *Radiation Shielding*. American Nuclear Society, 2000

5. TESTS OF A GAMMA SPECTROMETER-NEUTRON COUNTER RELATIONSHIP AS A NEUTRON ALARM METRIC IN MOBILE SEARCH SYSTEMS*

5.1. Introduction

Nuclear security operators frequently employ mobile radiation search systems (MRSS) to screen areas for illicit nuclear materials. These vehicle-mounted systems can be employed for operations that require securing an area either before a major public event (like a sporting event or Presidential inauguration) or during an incident response (where such devices may have already been used). Fortunately, radiological material emits characteristic radiation, specifically gamma rays and neutrons, and an MRSS thus employs gamma spectroscopy and neutron counting radiation detectors to aid in locating these materials.

One requirement in these operations is understanding the ambient (or “background”) detector response, which is necessary for them to alarm when in the presence of man-made radioactive material. This is essential, as all alarms require adjudication, including incorrect ones, and the adjudication of these false alarms results in time lost during these extremely time-sensitive operations. Unfortunately, the fact that these systems are always moving makes characterizing much more difficult than would be needed for stationary laboratory measurements. This problem is mitigated in the gamma spectroscopy system as background produces an energy spectrum that is unique from any man-made materials. Conversely, the neutron counting system does not have such a unique background

*Reprinted with permission from ARTICLE TITLE by Jackson N. Wagner, Craig Marianno, and Daren Cline in *JOURNAL* response, and complexities in neutron physics causes that response to be affected in more ways than would occur in the gamma spectrometer.

Fortunately, previous research has shown that the problems with characterizing the neutron background can be mitigated using data from the gamma spectrometer after small modifications. That work found that when calibrated for much higher energy scales (up to 70 MeV instead of 3-4 MeV), the gamma spectrometer primarily detects muons [1]. These muons are produced by the same processes that produce background neutrons, which suggests that the detection of both particles would vary similarly in background conditions [2]. Further work showed that this indeed occurs in these mobile search systems, and the muon and neutron count rates are correlated by a power law relationship [3]. More importantly, no man-made source of muons exists outside of laboratory conditions, which means the muon count rate in a MRSS at any given time is much more likely to be from background than a neutron count rate. Thus, it is conceivable that the power law relationship determined from previous work could be applied to estimate the background neutron count rate using the muon count rate. That estimate could be used to determine if a man-made neutron source is present.

This research sought to test the applicability of a neutron alarm method derived from the neutron-muon power law relationship derived in previous work, particularly in a scenario where the neutron background is expected to change. For this, an MRSS's muon count rate was used to estimate its background neutron count rate and compared against what that detector observes when radiological material may be present. A parking garage was selected for these tests because it is the most extreme scenario where the neutron background is likely to change. The development of this method sought to improve the MRSS's capabilities to account for such changes as they would occur in parking garages or urban areas while maintaining its sensitivity to neutron emitting radiological materials. Since the neutron-muon relationship as it stands is empirical these tests required the use of the same system as was used in previous research to develop the relationship [3]. To determine this new method's effectiveness, it was also compared against a more intuitive alarm method from a constant estimate of the neutron count rate.

5.2. Materials and Methods

As mentioned above, these tests utilized the same system as those used to characterize the neutron-muon relationship described in previous work [3]. This consisted of one 2"-by-4"-by-16" (5.08 cm-by-10.16 cm-by-40.64 cm) sodium iodide (NaI) detection system with an Ortec digiBASE multichannel analyzer (MCA) and one Ortec neutron counting system with four 1"-by-18" (2.54 cm-by-45.72 cm) 3He tubes encased in a high-density polyethylene (HDPE) moderator [4,5]. The NaI detector's energy calibration was made using ^{137}Cs and ^{22}Na as shown in Table 5-1 to achieve an approximately 70 MeV energy scale, and data below channel 62 (of 1024 with the first channel labelled "0") were ignored to discriminate gamma rays. The detectors were placed in a vehicle as shown in Figure 5-1 with the NaI detector placed lying flat with its largest face parallel to the ground (i.e. with its largest face "looking up" from the vehicle). Data were also collected from a PVT detector in the same orientation and another NaI detector in a different orientation (lying flat with its largest face perpendicular to the ground – “looking out” from the vehicle), but they were not included since their neutron-muon relationships were not as well defined.

Table 5-1. Calibration information for the NaI detector.

			^{137}Cs	^{22}Na	
Gamma Ray Energy		[keV]	662	511	1274
Photopeak	Energy	[keV]	662	511	1274
	Channel Number		10.5 ± 1	8 ± 1	19.5 ± 1
Calibration		[keV ch^{-1}]	68.0 ± 10.7		

The parking garage in which these measurements took place was the Central Campus Garage (CCG) on the campus of Texas A&M University. This structure has eight levels of parking space with a mirrored, spiral traffic pattern, where two sides of the same parking level have opposite traffic directions (in terms of moving toward upper or lower levels). Schematics of a selection of the eight levels of CCG are shown in Figure 5-2. Measurements occurred in “sweeps” of the entire height of the garage. The mobile search system would begin on either the top or bottom level (eight or one, respectively) and follow the normal traffic route as it traversed up and down the garage until the vehicle returned to its starting location.

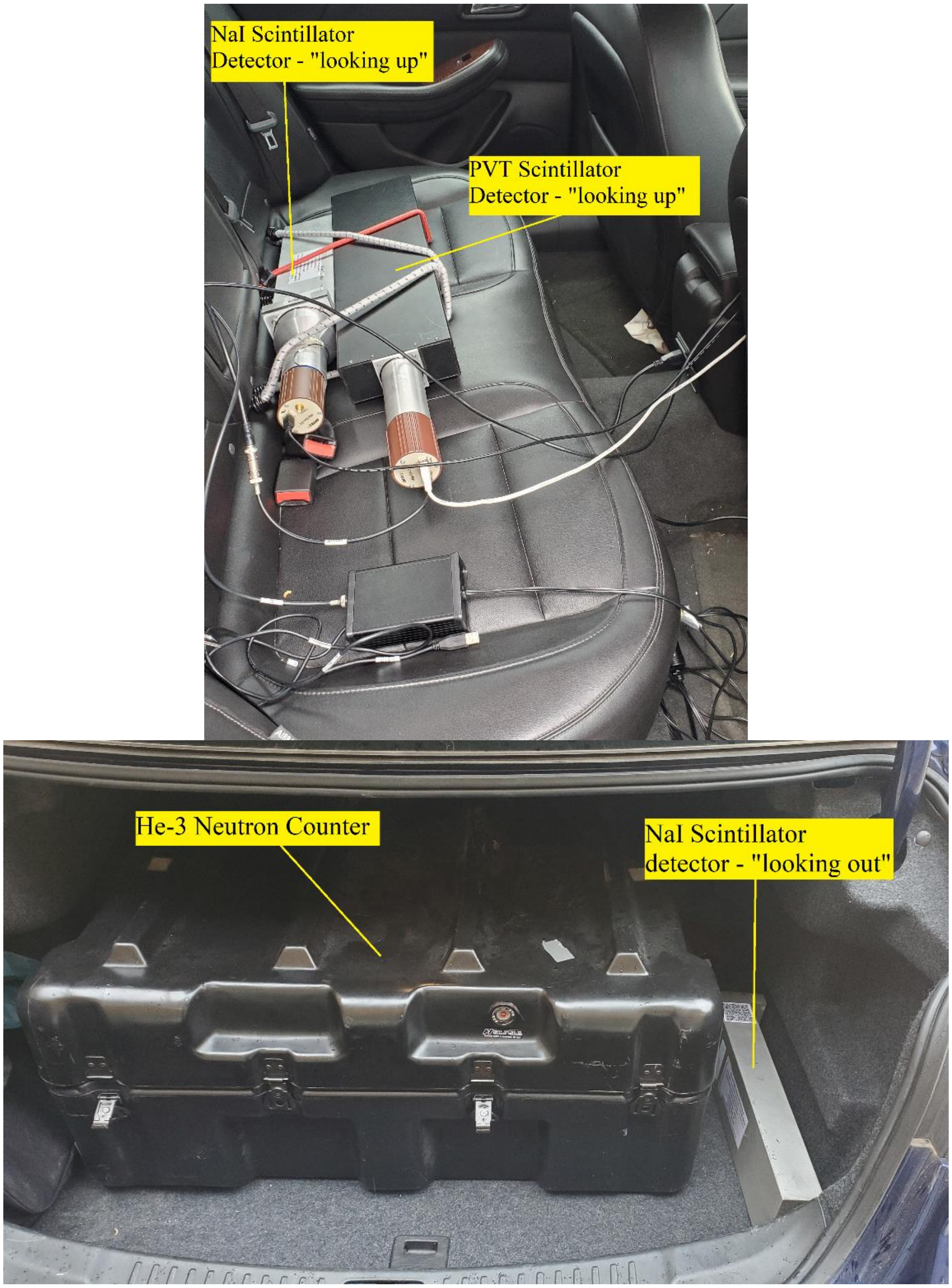

Figure 5-1. Detector setup in the cabin (top) and trunk (bottom) of a sedan used for mobile search measurements of a parking garage with a neutron source present.

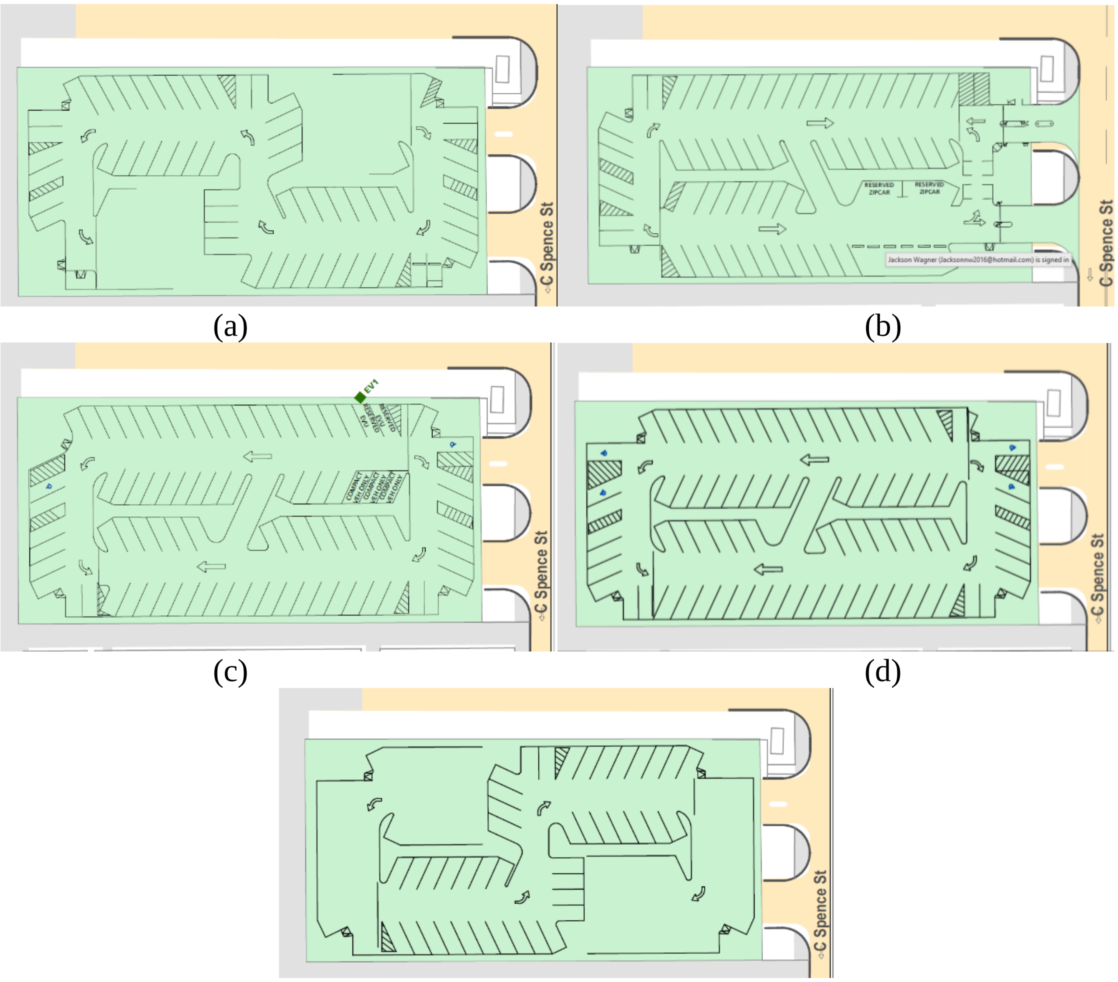

(a) (b)

(c) (d)

(e)

Figure 5-2. Maps indicating the layouts and traffic patterns of a selection of levels of CCG, which includes level 1 (a), level 2 (b), level 3 (c), level 7 (d), and level 8 (e). Mobile search sweeps began/ended on either level 1 or 8. During sweeps, the source was placed on the side of a level where traffic travelled downward (the bottom half shown in a, c, and d, and the top half shown in b and e).

For each sweep, a ^{252}Cf source present on one of eight levels of the garage. This source was placed in another vehicle that was parked on a given level on a side where the traffic flow was downward. The ^{252}Cf source had a total activity of approximately 886 kBq and a neutron emission rate of approximately 103,000 s^{-1}. After the eight sweeps with the source, one additional sweep was performed without the source in the garage. All data were collected during a single measurement campaign, and the overall measurement times of that campaign that correlate to the start and end of each sweep are shown in Table 5-2 with the respective start and source positions. Neutron and muon count rate data collected during these sweeps were used to create two neutron alarm metrics, values which indicate the presence of a man-made neutron source when a certain condition is met.

Table 5-2. Times in the measurement campaign (in seconds after starting acquisition) that sweeps began and ended along with the sweep's respective start/end level and source level. The final, background sweep (indicated by Source Level *) consisted of a full sweep that began/ended at Level 8 plus a "half-sweep" as the system returned to level 1 before exiting the garage.

Sweep Start/end Level	Source Level	Start Time [s]	End Time [s]
1	8	1090	1380
1	7	1450	1725
8	6	1940	2210
8	5	2280	2550
8	4	2630	2900
8	3	3000	3275
8	2	3380	3650
8	1	3770	4040
8	*	4160	4650

The primary difference between these two metrics is their method for estimating the average neutron count rate. This estimation is essential to an alarm metric as will be made clear later. The first alarm metric used an intuitive estimation of the average neutron count rate, namely one determined from a brief measurement of known background conditions. In this case, measurements occurred before entering the parking garage both while the MRSS was travelling to the area and was static nearby (measurements were between 300 s to 700 s relative those shown in Table 5-1). The estimate of the average neutron count rate then came from the overall average count rate during that period. This average value remained constant and was used throughout measurements, and its alarm metric was used as the control for these tests. The second alarm metric used a calculated estimate of the average neutron count rate based on the neutron-muon relationship defined in previous research. Specifically, the estimated average background neutron count rate was calculated from the measured average muon count rate as shown in Eq. 5.1 [3]. Unlike the control method, this estimate was dynamic and changed with expected changes in the neutron background. These changes occurred frequently in the parking garage with the variances in and amount of concrete shielding, hence its selection as the scenario for these tests.

$$\bar{n} = 0.001149\,\bar{m}^{2.0567} \tag{5.1}$$

Where:

$\bar{n}$ = average neutron count rate [s^{-1}]
$\bar{m}$ = average muon count rate [s^{-1}]

Using an average value of the neutron and muon count rates was necessary for these alarm metrics due to the characteristics of these particles. The physics that govern the creation and detection of both neutrons and muons result in their measurements being random variables, each with their own probability distribution. Specifically, these are Poisson random variables because measurements of these particles occur by counting the number detected over a given period. This means that the probability of a certain number of counts for each particle within a given time (which are integers greater than or equal to zero) will follow the Poisson probability mass function (pmf) as shown in Eq. 5.2. The shape of a pmf is dictated by its expected counts, λ, within that observation time. While Eq. 5.2. shows any observed value (greater than zero) is possible, increasingly large observations relative to the expected value are increasingly unlikely, which is the main aspect for any alarm metric.

$$\mathrm{pmf}(x) = \Pr(X = x) = \frac{\lambda^x}{x!} e^{-\lambda} \tag{5.2}$$

Where:

$X =$ Poisson random variable of counts (integers greater than or equal to zero) observed in a given time with an expected value of λ
$x =$ one observation of X
$\Pr(X = x) =$ the probability that an observation of X will result in x counts
$\lambda =$ expected number of counts from Poisson random variable X

An MRSS would operate under the assumption that no man-made source of neutrons is present (i.e. operators assume it is measuring “background”), and its alarm algorithm would expect to observe counts within a Poisson distribution that has a known expected value. In statistics, this assumption would be called the null hypothesis and is considered true under most, if not all, scenarios. An alarm occurs when an observation has an exceedingly low probability of occurring as part of the null hypothesis' Poisson distribution, thus providing evidence in favor of an alternative hypothesis. The alternative hypothesis in this case is that a man-made neutron source is present.

Evidence in favor of this alternative hypothesis is indicated when the background Poisson distribution has a low probability of producing a given observation. This probability is calculated by determining the cumulative probability of all count values less than the observation as described in Eq. 5.3. Because a man-made source of neutrons will increase the expected count rate, larger values from Eq. 5.3 would indicate stronger evidence for rejecting the null hypothesis that counts are from background. However, the null hypothesis cannot be rejected until the cumulative probability of that value is sufficiently large. This threshold is dictated by the desired maximum probability of false positives (i.e. how likely an incorrect rejection of the null hypothesis might occur). For this research, a false alarm probability of 0.05 was desired as it is what the International Atomic Energy Agency (IAEA) suggests for most measurement operations [6]. This means that the cumulative probability threshold needed to be 0.95. Therefore, if an observation causes Eq. 5.3 to produce a value greater than 0.95, it can be said that the observation likely did not come from background. As a result, the maximum probability of that statement being falsely made would be 0.05 (or one in twenty, on average).

While an alarm metric would monitor the result of Eq. 5.3 for values that are greater than greater than 0.95, the asymptotic nature of the Poisson cumulative distribution function makes this difficult to display visually. One solution is to modify the result of Eq. 5.3 by applying the function shown in Eq. 5.4 to generate an alarm metric, M_A. M_A would then be monitored for values that are larger than the threshold dictated by the selected false positive probability, which is this case is $\Pr(X \rightarrow x) = 0.95$ or $M_A = 2.9957$. The value of M_A has no asymptote, which makes its plots as a function of time more visually intuitive as will be observed later.

$$\Pr(X \rightarrow x) = \Pr(X < x) = e^{-\lambda} \sum_{i=0}^{x-1} \frac{\lambda^i}{i!} = e^{-\lambda} \left(1 + \frac{\lambda^1}{1!} + \frac{\lambda^2}{2!} + \cdots + \frac{\lambda^{x-1}}{(x-1)!} \right) \quad (5.3)$$

$$M_A = -\ln(1 - \Pr(X \rightarrow x)) \quad (5.4)$$

Where:

X = Poisson random variable of counts (integers greater than or equal to zero) observed in a given time with an expected value of λ
x = one observation of X
$\Pr(X \rightarrow x)$ = the probability that observation x is the result of variable X
λ = expected number of counts from variable X in a given time
M_A = Alarm metric

This is not a novel method for calculating an alarm metric and is arguably the simplest method. The main difficulty in its application is in estimating the expected value of λ, the background neutron count rate distribution. Any Poisson random variable's count distribution and its expected value will only match those suggested by Eq. 5.2 with an infinite number of observations, the collection of which is an impossible task for any human. However, any number of observations can produce an estimate of that value whose accuracy would increase with more observations.

While an MRSS has significant limitations in the observations they can obtain for their estimate, they still have a variety of techniques to make that estimation. One such technique has already been described: the measurement of background before entering the garage. The average neutron count rate over this time informed the expected value for the control method's alarm metric. Specifically, the expected value was the product of that average value and the observation time. As part of the control, this value was constant throughout the measurement and was used with observations to calculate values of Eq. 5.3 and Eq. 5.4.

The other estimation technique applied the neutron-muon relationship described in Eq. 5.1. That relationship allowed the estimation to be dynamic, and because of that, a much smaller observation time was used to estimate the expected value than that for the control. In this case, the average muon count rate at any given time was calculated using the data from the previous 15 s (this value was selected as the observation time for calculating both alarm metrics as well, which will be discussed below). That average muon count rate was used in Eq. 5.1 to calculate the average neutron count rate, and similar to the control method, the expected value was the product of that average neutron count rate and the observation times. While this estimate was dynamic during measurements, it and the observations were used with Eq. 5.3 and Eq. 5.4 similar to that with the control's estimate.

To properly use either expected value in the above equations, an observation time is required, which was 15 s for these measurements. This value was selected to reduce the random noise that appears in the observations while allowing the data to respond to the variances that occur in the parking garage while travelling at normal speeds. These variances came from the MRSS moving from one level to the next one (either up or down), thus changing the amount of nearby shielding, and this would occur approximately every 20 s during the sweeps. From this, 15 s was selected to reduce the likelihood that data from the previous level contributed to an observation. From this, the expected number of neutron counts (or the value of λ in Eq. 5.3) was the product of either method's average value and 15 s, which was then compared against the number of neutron counts measured over the previous 15 s (or the value of x in Eq. 5.3) at any given time. As mentioned previously, a common maximum false positive rate for these systems is 5%. Therefore, an alarm would occur if either method's value for M_A (from Eq. 5.4) was greater than 2.9957, particularly if that condition were met for a sustained period of time.

5.3. Results and Analysis

Plots of the two alarm metrics' values over time during the measurements are shown in Figure 5-3 through Figure 5-10 for sweeps 1 through 8, respectively, as defined in Table 5-1. These plots include markers showing the times where the sweep started and ended and the time the system reached the garage's "cross-over" point. The former simply indicate when the vehicle started and stopped moving through the garage, and by "cross-over point", the latter means the point where the vehicle reached the top or the bottom of the garage (depending on the level where the sweep started/ended) and thus changed whether it was moving upward or downward.

All these plots show that both methods would have produced alarms when the MRSS was nearest to (or on the same level and side as) the source as shown by the largest increase in the alarm metric(s). Along with that, both alarm metrics increased when the system was either on a level adjacent to the source or on the same level as the source, but on the opposite side. When that occurred, the metric from dynamic estimation method of the neutron expected value was more likely to exceed the alarm threshold and increase more than the constant estimation method.

As a comparison with these sweeps, the alarm metrics for the final, background sweep over time are plotted in Figure 5-11. This shows that the alarm metrics did not increase as much as when the source was present, as expected. However, there were two instances where the dynamic alarm metric crossed the alarm threshold in a meaningful way. The two alarm's midpoints occurred at approximately 4300 s and 4360 s, which would have been when the MRSS was on level one (the cross-over point) and level three, respectively. One explanation for this might be that while the source was not in the garage during this sweep, it was nearby as it was being secured in a building across the street during the first half of that sweep. This suggests that the system was still observing excess neutrons from that source, albeit in a reduced fashion from the other tests, which the dynamic alarm metric was able to recognize as such. This is further indicated by the fact that these occurred when the MRSS was on or just above/below ground level, where the garage walls would have had less of a shielding effect on that source than when the MRSS was at higher levels.

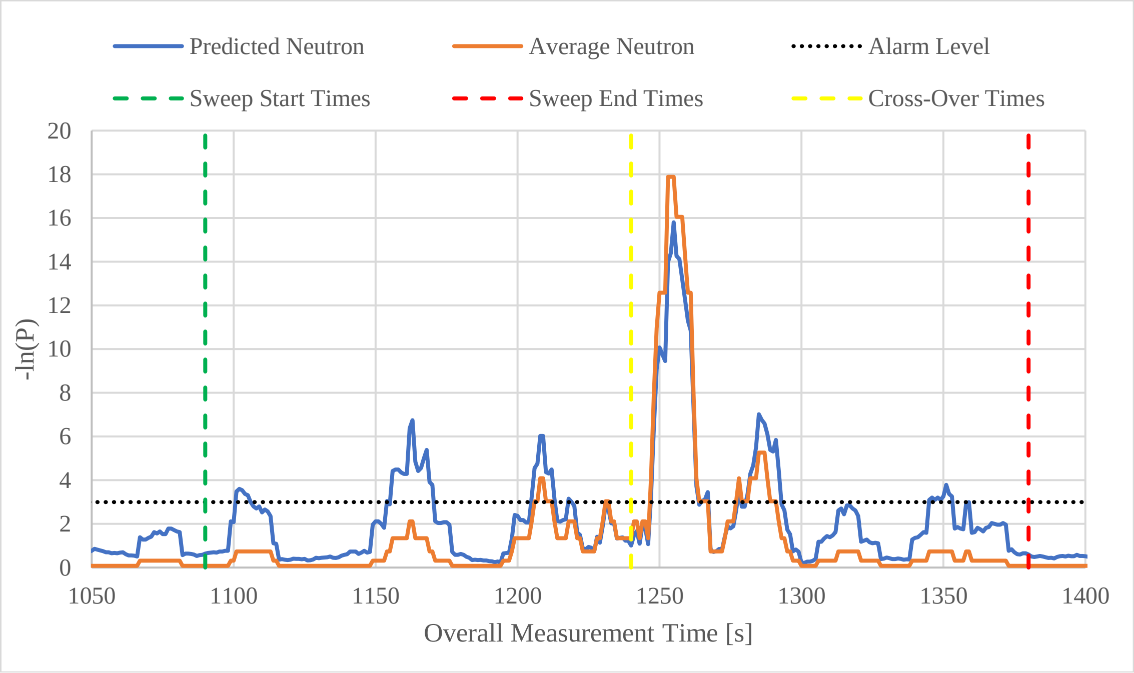

Figure 5-3. Alarm metrics over time during a sweep with the source on Level 8, where the sweep began and ended on Level 1 as indicated by the green and red vertical dashed lines, respectively. The yellow vertical dashed line indicates the cross-over point from the “upward” section of the garage to the “downward” section on Level 8. Alarm metrics were calculated using the predicted background neutron count rate (blue) and the constant average background neutron count rate (orange), and an alarm would occur when these metrics’ values were greater than the threshold indicated by the black dotted line.

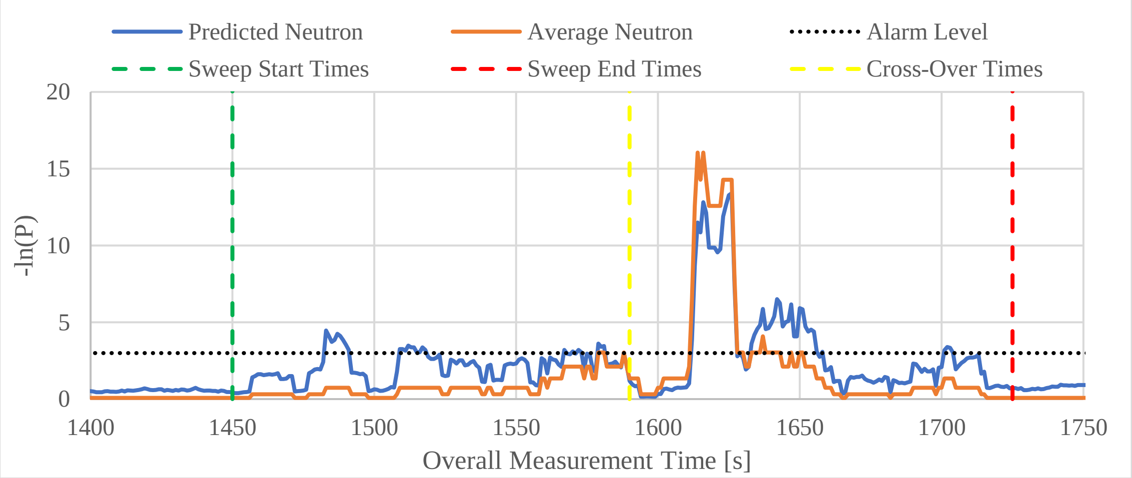

Figure 5-4. Alarm metrics over time during a sweep with the source on Level 7, where the sweep began and ended on Level 1 as indicated by the green and red vertical dashed lines, respectively. The yellow vertical dashed line indicates the cross-over point from the "upward" section of the garage to the "downward" section on Level 8. Alarm metrics were calculated using the predicted background neutron count rate (blue) and the constant average background neutron count rate (orange), and an alarm would occur when these metrics' values were greater than the threshold indicated by the black dotted line.

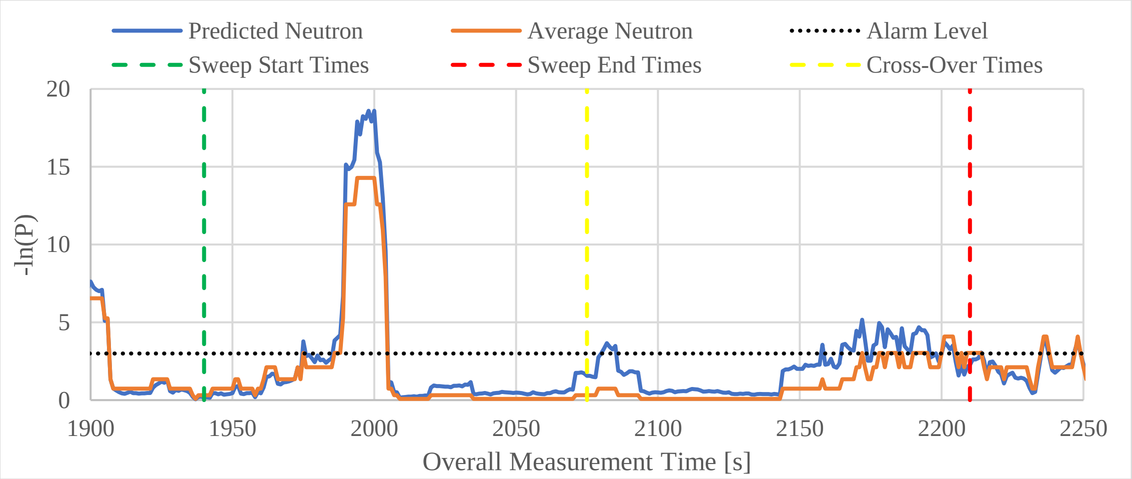

Figure 5-5. Alarm metrics over time during a sweep with the source on Level 6, where the sweep began and ended on Level 8 as indicated by the green and red vertical dashed lines, respectively. The yellow vertical dashed line indicates the cross-over point from the "upward" section of the garage to the "downward" section on Level 1. Alarm metrics were calculated using the predicted background neutron count rate (blue) and the constant average background neutron count rate (orange), and an alarm would occur when these metrics' values were greater than the threshold indicated by the black dotted line.

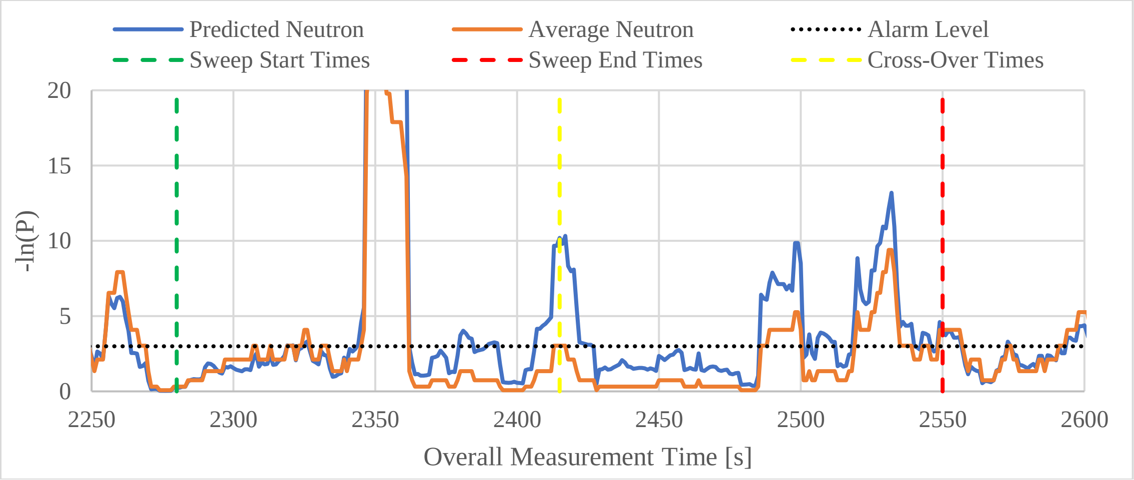

Figure 5-6. Alarm metrics over time during a sweep with the source on Level 5, where the sweep began and ended on Level 8 as indicated by the green and red vertical dashed lines, respectively. The yellow vertical dashed line indicates the cross-over point from the "upward" section of the garage to the "downward" section on Level 1. Alarm metrics were calculated using the predicted background neutron count rate (blue) and the constant average background neutron count rate (orange), and an alarm would occur when these metrics' values were greater than the threshold indicated by the black dotted line.

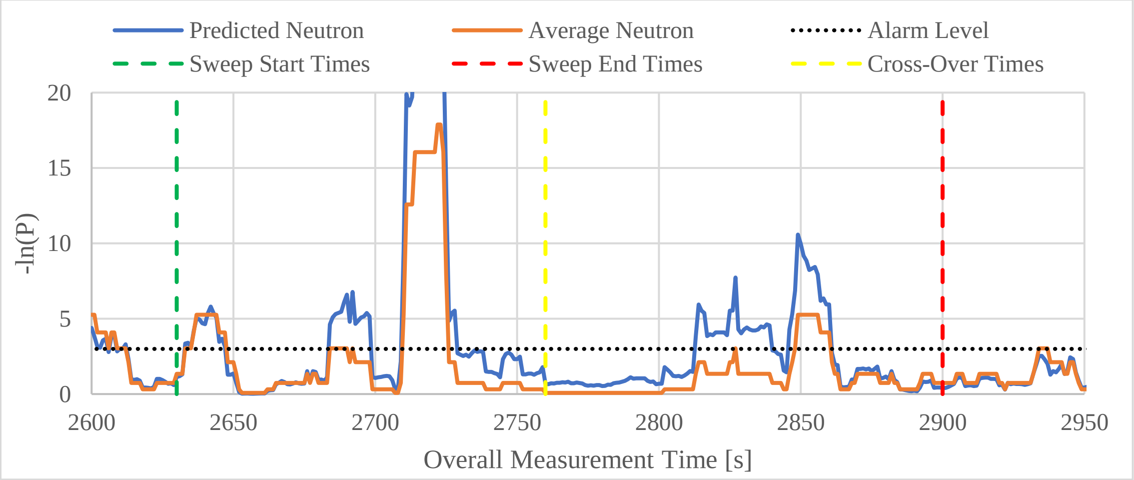

Figure 5-7. Alarm metrics over time during a sweep with the source on Level 4, where the sweep began and ended on Level 8 as indicated by the green and red vertical dashed lines, respectively. The yellow vertical dashed line indicates the cross-over point from the "upward" section of the garage to the "downward" section on Level 1. Alarm metrics were calculated using the predicted background neutron count rate (blue) and the constant average background neutron count rate (orange), and an alarm would occur when these metrics' values were greater than the threshold indicated by the black dotted line.

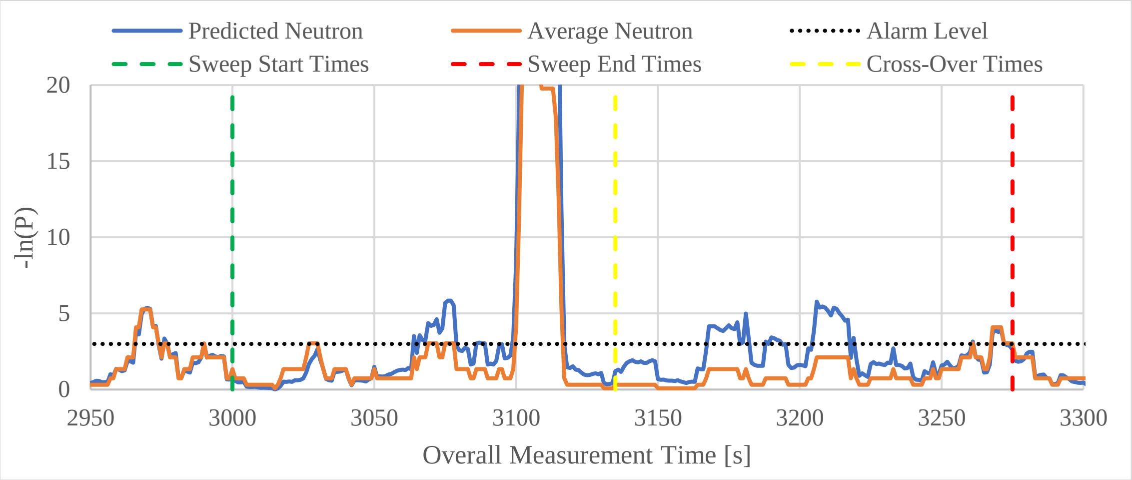

Figure 5-8. Alarm metrics over time during a sweep with the source on Level 3, where the sweep began and ended on Level 8 as indicated by the green and red vertical dashed lines, respectively. The yellow vertical dashed line indicates the cross-over point from the "upward" section of the garage to the "downward" section on Level 1. Alarm metrics were calculated using the predicted background neutron count rate (blue) and the constant average background neutron count rate (orange), and an alarm would occur when these metrics' values were greater than the threshold indicated by the black dotted line.

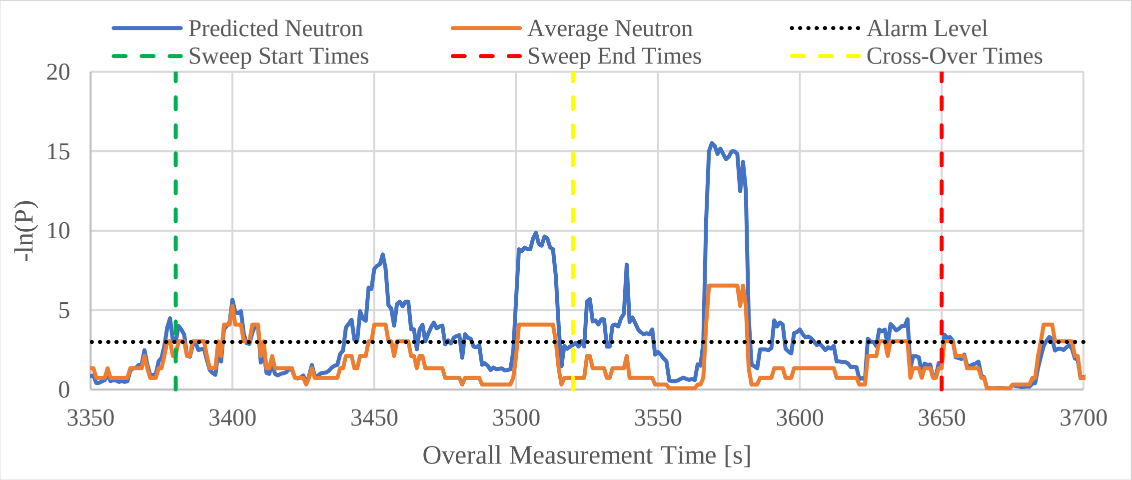

Figure 5-9. Alarm metrics over time during a sweep with the source on Level 2, where the sweep began and ended on Level 8 as indicated by the green and red vertical dashed lines, respectively. The yellow vertical dashed line indicates the cross-over point from the "upward" section of the garage to the "downward" section on Level 1. Alarm metrics were calculated using the predicted background neutron count rate (blue) and the constant average background neutron count rate (orange), and an alarm would occur when these metrics' values were greater than the threshold indicated by the black dotted line.

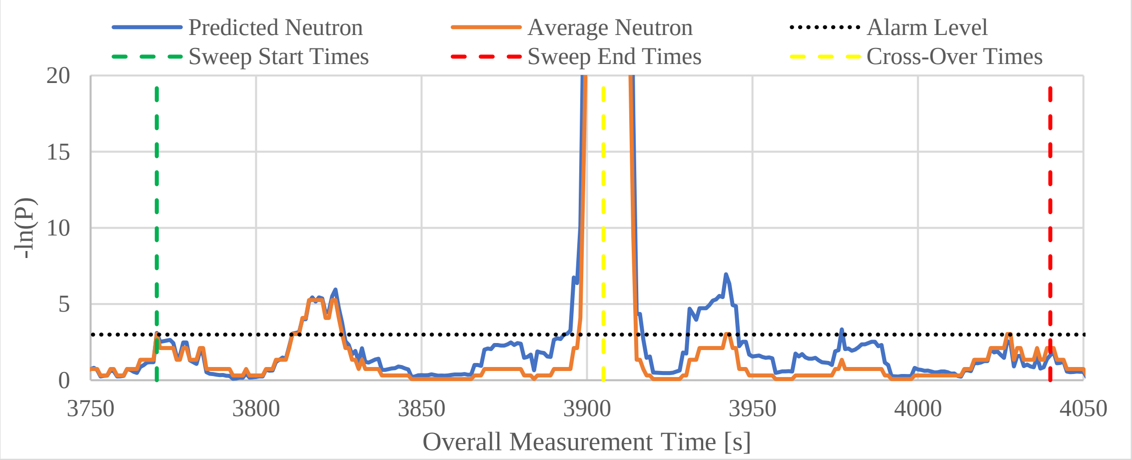

Figure 5-10. Alarm metrics over time during a sweep with the source on Level 1, where the sweep began and ended on Level 8 as indicated by the green and red vertical dashed lines, respectively. The yellow vertical dashed line indicates the cross-over point from the "upward" section of the garage to the "downward" section on Level 1. Alarm metrics were calculated using the predicted background neutron count rate (blue) and the constant average background neutron count rate (orange), and an alarm would occur when these metrics' values were greater than the threshold indicated by the black dotted line.

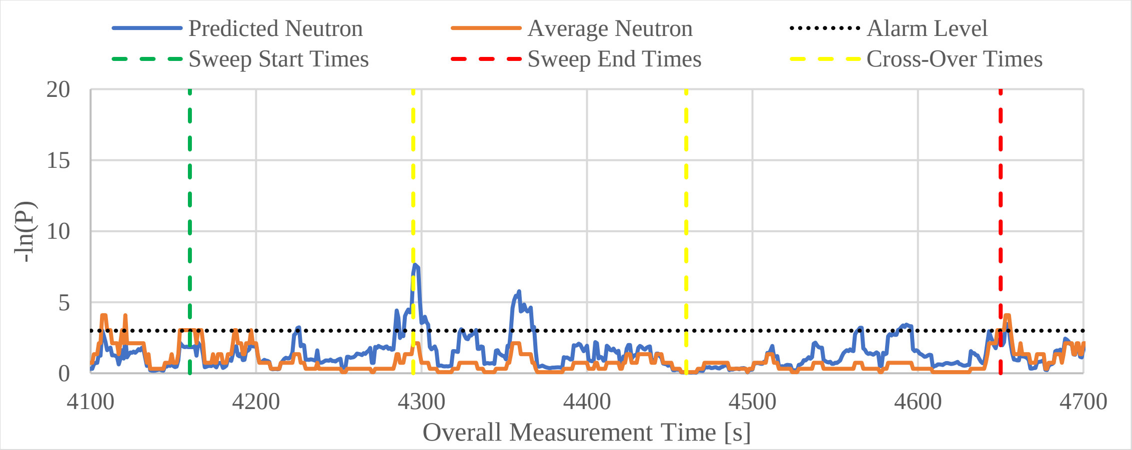

Figure 5-11. Alarm metrics over time during a sweep with no source in the garage, which consisted of one full sweep starting from Level 8 (green vertical dashed line) with an additional "half-sweep" that returned to Level 1 to exit the garage (red vertical dashed line). The yellow vertical dashed lines indicate the cross-over points with the first being from the "downward" section of the garage to the "upward" section at Level 1 and the second being from the "upward" section to the "downward" section at Level 8. Alarm metrics were calculated using the predicted background neutron count rate (blue) and the average background neutron count rate (orange), and an alarm would occur when these metrics' values were greater than the threshold indicated by the black dotted line.

Similar to the background sweep, the alarm metrics under more “normal” background conditions (before the system entered the garage) are shown in Figure 5-12. These data were collected in a suburban-type environment, where few buildings were near the system, but not in such a way that would affect the neutron or muon count rates. The source was brought in proximity of the detectors during the final setup, which caused the extremely high values between time 750 s and 880 s. After that, the system then entered the garage shortly after that (at 900 s) to get into position for the first sweep, hence the variable alarm metrics shown between 880 s and 1050 s. These data, particularly those before 750 s, show that in less extreme environments (i.e. not in urban areas or a parking garage) both alarm metrics would produce similar values regardless of whether a neutron source is present.

One potential limitation for this method lies in the way a system measures the muon count rate. For these measurements, the muon count rate was the total counts between 4 MeV and 70 MeV in an NaI detector. Measurements with this and similar systems have shown that the potential exists for excess detections at the lower end of this range. This occurred during a similar test with the above system, where the source was placed on the trunk of the vehicle (above the neutron detector). A plot of the relevant count rates during this time are shown in Figure 5-13. Those data show that the source caused the neutron count rate to increase significantly, but the “muon” count rate also increased, which in turn caused an increase in the estimated neutron count rate. However, Figure 5-14 shows that something similar did not occur when the source was nearby the mobile search system before it entered the parking garage.

A similar phenomenon occurred during measurements performed by a Department of Energy Radiological Assistance Program (RAP) team that were analyzed with previous work [3]. In that system, the muon count rate was the total counts in the NaI detector's overflow channel, which included counts between 3 MeV and approximately 12 MeV. During the measurements, the system was near an ion beam facility while it was active, which greatly increased their systems' neutron count rate as seen in Figure 5-15. Similar to the data in Figure 5-13, there was also an increase in this their overflow channel count rate, which caused the estimated neutron count rate to increase.

In both cases, the observed neutron count rate increased significantly to where an alarm still would have occurred despite the estimate being affected. Because of this, it is likely that the detections that occurred were the result of the sources themselves or secondary reactions they caused. In the case of the ^{252}Cf source, it is likely that the excess NaI detections were a result of (n,γ) reactions with materials in the vehicle. In this case, the $^{56}Fe(n,\gamma)^{57}Fe$ reaction is likely to occur in the vehicle's steel, and that reaction has a nontrivial probability of emitting gamma rays with energies up to 7.6 MeV [7]. This specific interaction is likely because the effect occurred when the source was placed on the vehicle (Figure 5-14), but not when the source was nearby for a significant period (Figure 5-13). Similar reactions are likely to have occurred in the scenario of the ion beam facility due to the excess radiation it may emit while active. However, the characteristics of that radiation and the nearby materials are unknown, which prevents any further speculation. These data suggest it is plausible that such an effect may only occur with strong neutron sources, but more research would be required to confirm such a characteristic. This confirmation would be important as these appear to be the only scenarios where non-background environments would affect the estimate of the background neutron count rate.

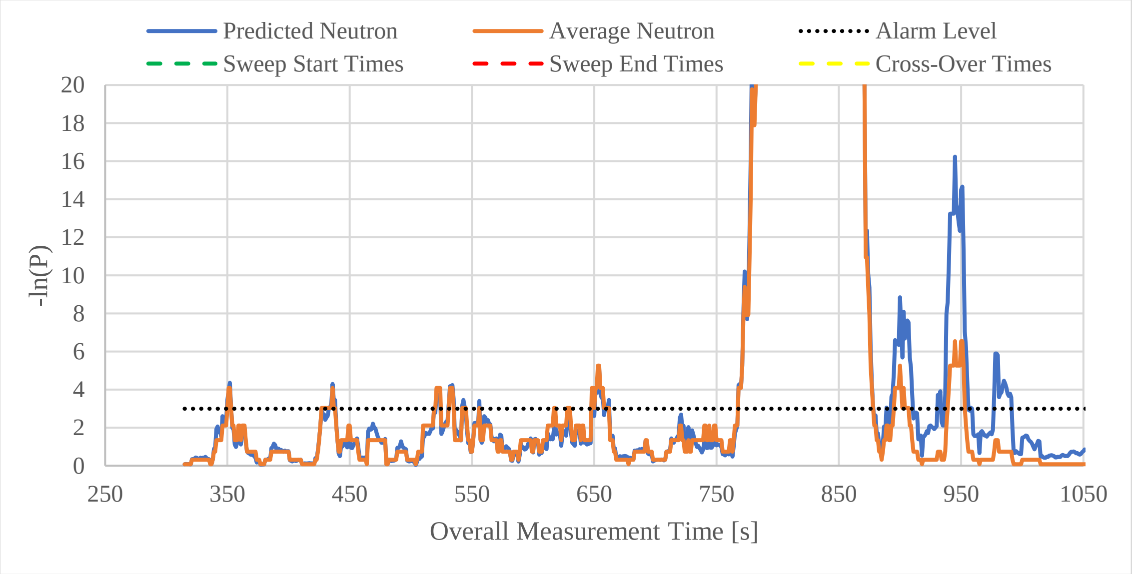

Figure 5-12. Alarm metrics over time during measurements prior to and just after entering the garage. Alarm metrics were calculated using the predicted background neutron count rate (blue) and the average background neutron count rate (orange), and an alarm would occur when these metrics' values were greater than the threshold indicated by the black dotted line. Data from 300 s to 700 s were used to calculate the average background neutron count rate. The source was next to the system between 750 s and 880 s. With the source in the garage, the system entered the garage at 900 s and moved into position for the first sweep after 1050 s.

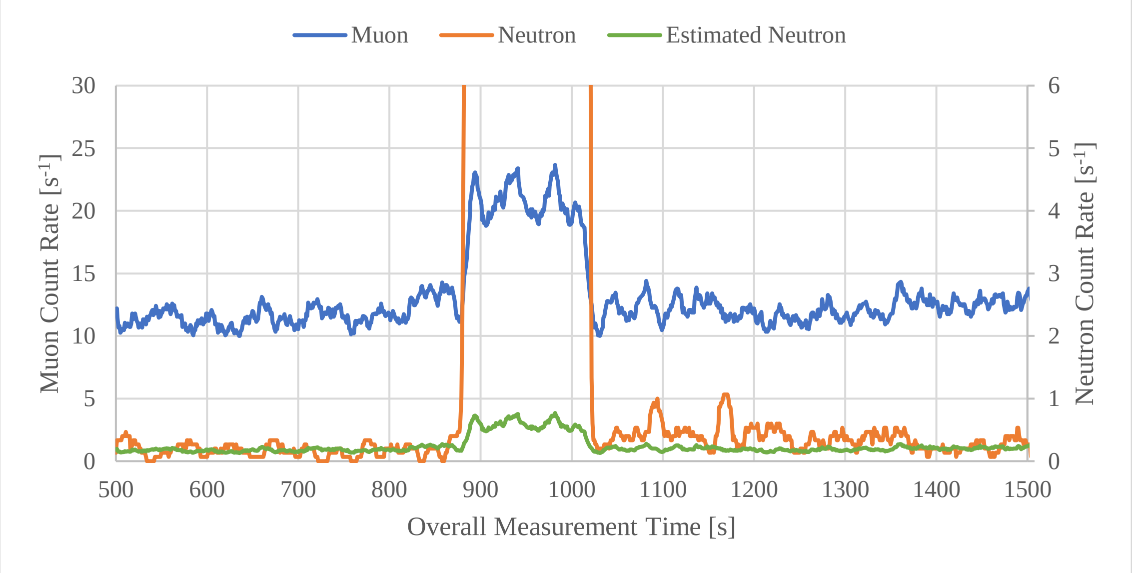

Figure 5-13. Muon (blue – left axis), observed neutron (orange – right axis), and estimated neutron (green – right axis) count rates over time during separate measurements with the mobile search system. The ^{252}Cf source was placed on the trunk of the mobile search vehicle between 870 s and 1040 s.

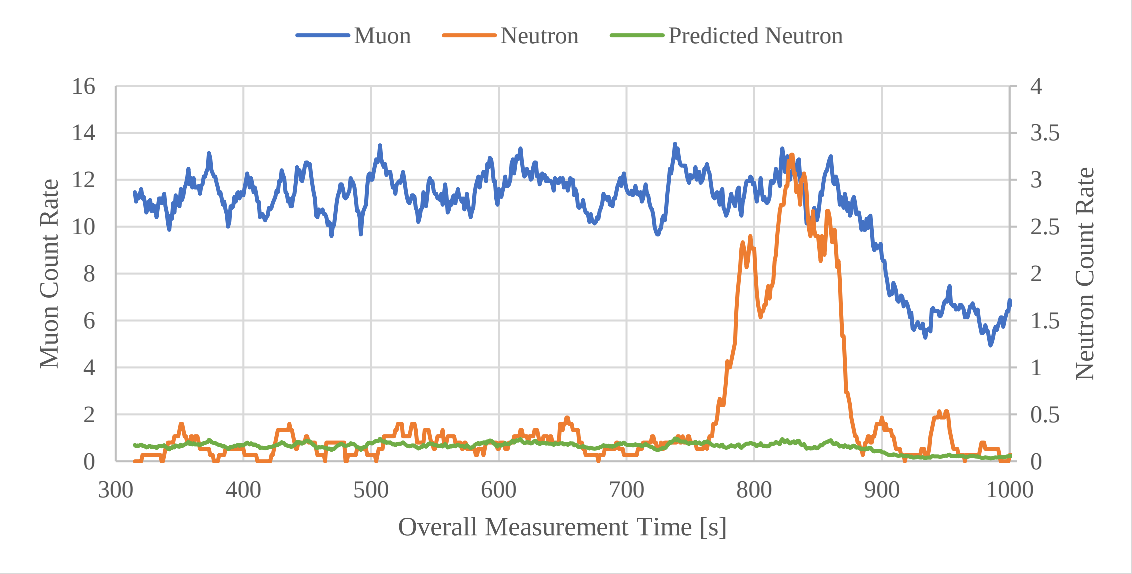

Figure 5-14. Muon (blue – left axis), observed neutron (orange – right axis), and estimated neutron (green – right axis) count rates over time before parking garage measurements with the mobile search system. The 252Cf source was placed adjacent to the system between 750 s and 880 s.

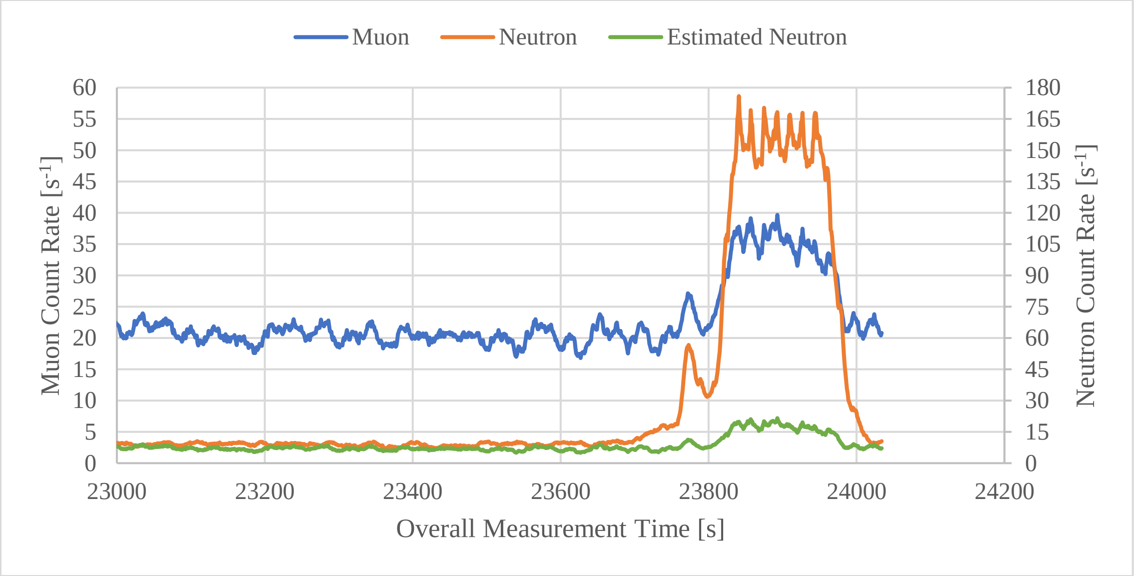

Figure 5-15. Muon (blue – left axis), observed neutron (orange – right axis), and estimated neutron (green – right axis) count rates over time during RAP measurements as part of previous work [3]. The ion beam facility was active between 23700 s and 24000 s.

5.4. Conclusion

This work shows that a dynamic estimate of the background neutron count rate from its power law relationship with an MRSS's muon count rate is a meaningful basis for a neutron alarm metric. Measurements of a source in a parking garage showed that the dynamic alarm method produced alarm at the same rate or more often than a commonly used method which applies a constant estimate of the neutron background. A dynamic method such as this has the added benefit of being able to account for common background changes an MRSS may observe, which should reduce an MRSS's false alarm rate. Along with that, it is conceivable that an improved estimate of the neutron background throughout an MRSS's operation would improve its sensitivity to neutron-emitting radiological materials (making it able to alert operators to smaller amounts). These aspects will require further study to quantify the potential reduction in an MRSS's false alarm rate and its minimum detectable activity.

5.5. References

1. J. N. Wagner and C. Marianno, "Identification of the Ambient Response Relationship in Neutron Counting and Scintillation Measurement Systems," *Radiation Science and Technology*. Vol. 7, No. 1, 2021, pp. 7-14. doi: 10.11648/j.rst.20210701.12
2. J. F. Ziegler, "Terrestrial Cosmic Rays", *IBM Journal of Research and Development*, 1996.
3. J. N. Wagner and C. Marianno, "Characterization of a Gamma Spectrometer-Neutron Counter Background Correlation in Mobile Search Systems," Unpublished.
4. D. L. Upp, R. M. Keyser, Performance of a car-mounted neutron and gamma-ray monitoring system for illicit material detection, in: Proc. 45th INMM Annual Meeting Institute of Nuclear Materials Management, 2004.
5. AMETEK Inc. – ORTEC, "digiBASE 14-Pin PNT Tube Base with Integrated Bias Supply, Preamplifier, and MCA (with Digital Signal Processing) for NaI Spectroscopy," available at https://www.ortec-online.com/-/media/ametekortec/brochures/digibase.pdf (accessed on September 7th, 2020).
6. INTERNATIONAL ATOMIC ENERGY AGENCY, "IAEA Safeguards Glossary," *International Nuclear Verification Series* No. 3, IAEA, Vienna (2003).

7. R.B. Firestone, T. Belgya, M. Krtička, et. al. “Thermal Neutron Capture Cross Section for ^{56}Fe(n,γ).” *Physical Review* C 95, 014328 (2017).

6. CONCLUSIONS

This work developed a new method to estimate the background neutron response in nuclear security systems that simultaneously employ neutron counting and gamma spectroscopy techniques, particularly in mobile search systems. This method is able to account for normal changes in neutron background that may occur during standard operations, and it improves these systems' sensitivity to neutron emitting radiological materials. Applying this method requires a non-standard data stream from a nuclear security operator's gamma spectroscopy system, where some operators already employ a usable technique with no modifications. Some such operators initially indicated a phenomenon related to that technique that led to the development of this method.

Nuclear security operators noted a correlation between their high gamma energy scintillator and neutron count rates during standard operations, which was independently confirmed as part of this work. This independent confirmation applied static measurements on all levels of multiple parking garages using ^{3}He neutron counters and a NaI scintillation spectrometer. The latter was calibrated to energies up to 50 MeV (using ^{137}Cs and ^{22}Na) and ignored common background gamma ray energies (0-4 MeV). These measurements observed a linear correlation between the neutron count rate and the 4-50 MeV gamma radiation count rate. The presence of this relationship required confirming its cause in these systems, namely the radiation background high energy scintillator responses.

Long radiation background measurements using scintillators calibrated for high gamma energies led to the confirmation that these high energy scintillator responses were the result of muons. The measured spectra for both NaI and PVT scintillator detectors exhibited one or more modes depending on the detector's orientation, and those modes appeared at energies that correlated with muon energy depositions for path lengths approximately equal to the detectors' dimensions. These results matched those from MCNP radiation transport simulations of the detectors' responses to background muons and simple Python calculations of muon path length spectra. Since muons cause these high energy scintillator responses, it indicates that the observed correlation is the result of background muons and neutrons being produced by similar processes.

The confirmation that high energy scintillator responses were the result of muons suggested that they would be correlated with background neutrons, and this result was indicated through measurements throughout the central region of the continental United States. These measurements used ^{3}He and NaI scintillators similar to those commonly employed in mobile search systems, and they measured areas during long trips in rural areas along with short campaigns that canvassed various cities' downtowns. The detectors' responses matched the expected variances in neutron and muon fluxes as functions of elevation, latitude, and local environment. More importantly, these responses produced a strong power law relationship for the neutron count rate as a function of the muon count rate, and this result appeared in similar data collected by nuclear security operators. The existence of this relationship suggests the background neutron count rate could be predicted.

The derived method to predict the background neutron count rate from the muon count rate was applied to a mobile search system, and it indicated that the prediction could be applied to determine whether neutron-emitting radiological material was present. These measurements were performed with a mobile search system sweeping a parking garage while a ^{252}Cf source was placed on various levels. The results showed that a neutron alarm metric derived from the predicted background neutron count rate performed at least as well as an alarm metric from a constant estimate of the neutron background when alerting for the presence of that material. Despite this ability to apply this dynamic estimate as an alarm metric, it can be improved through additional research.

6.1. Future Work

There are three areas where further research would augment the usability of this work, and the first area relates to the fact that the neutron-muon relationship presented is empirical. This means that operators who wish to apply the methods prescribed would need to collect background data using their specific system configuration, and then they are limited to that specific configuration when applying the method. A generalized relationship would be a massive improvement where operators would be able to calculate the parameters of Eq. 4-4 from their specific system characteristics (e.g. either detector’s size/dimensions, material, energy calibration, etc.).

A second area of improvement would be the ability to apply the prediction method in real-time. All the alarm metrics presented were calculated after the data were collected, but it would be naturally beneficial for a mobile search system to apply such a method (and produce alarms from it) during the mobile search operation. This could likely be done with algorithms that are already applied for similar systems but with a constant estimate of that neutron background.

The final area of improvement would be to confirm the behavior described in chapter 5, namely the phenomenon where the “muon” count rate increases in certain scenarios where a neutron source is present. As mentioned in that chapter, it is likely that the phenomenon is the result of (n,γ) reactions with common materials like iron. Work on this topic would seek to confirm that was the cause of the effect and whether such a phenomenon could possibly negate a neutron alarm.

APPENDIX A

MUON SPECTRA CALCULATION CODE

Muon path length/energy spectra calculation using Python as shown in Chapter 3. Results in three .csv files representing energy histograms for two detectors in three orientations each.

```
import numpy as np
import math
import pandas as pd
import multiprocessing as mp

#####DETECTOR Characteristics#####
#NaI
#   dimensions [cm] – 5.08  x  10.16  x 40.64
#   eDep/length [MeV/cm] - 3.667*1.305
#PVT
#   dimensions [cm] - 6.35 x 16.51 x 62.31
#   eDep/length [MeV/cm] - 1.032*1.956

##############These settings affect memory size and cpu time requirements###############
LENGTH_RESOLUTION = 0.2    #Length step size for particle entry locations [cm]
ANGLE_RESOLUTION = 1        #Angle step size for particle directions [degrees]
############################################################################

ENERGY_BIN_WIDTH = 0.05     #Width for energy bins in final histogram [MeV]
NUM_PROCS = 5              #Number of CPU processes to use (initially set to use 5 of 6 CPU processors)

def calcPaths( x,y,z,eLength,numRep ):
    #Calculates energy depositions for all muon directions entering the detector at point (x,y,z),
    #which is done by calculating muon path lengths and multiplying by eLength (muon dE/dx in detector).
    #numRep represents the number of times the physical situation is possible (i.e. by symmetry)
    zAngles = np.arange(0,90, ANGLE_RESOLUTION)
    xyAngles = np.arange(0,90, ANGLE_RESOLUTION)

    eDeps    = np.zeros(len(zAngles)*len(xyAngles))           #Energy Deposition Array
    eDepProb = np.zeros(len(zAngles)*len(xyAngles))         #Energy Deposition Probability Array

    zFlux = 0.02908*np.cos(zAngles/float(360)*2.0*np.pi)+0.003939  #Muon Trajectory Spectrum (Ref. 3-15)
    zSum = np.sum(zFlux)
    zProbs = zFlux/float(zSum)                                           #Muon Trajectory Probability Spectrum

    zAng = np.repeat(zAngles,90)
    zProb = np.repeat(zProbs,90)
    lengths = z * np.tan(zAng/float(360)*2.0*np.pi)
    xyMax = min(x,y)
    xyAngs = np.arange(0,len(zAng),1)%90
    xyTrueLength = xyMax / np.cos(xyAngs/float(360)*2.0*np.pi)
    otherDim = max(x,y)

    eDeps[lengths <= xyMax] = eLength * z / np.cos( zAng[lengths <= xyMax]/float(360)*2.0*np.pi )
    eDeps[np.where((lengths > xyMax) & (lengths <= otherDim) & (lengths > xyTrueLength))] = eLength * xyTrueLength[np.where((lengths > xyMax) & (lengths <= otherDim) & (lengths > xyTrueLength))] / np.sin( zAng[np.where((lengths > xyMax) & (lengths <= otherDim) & (lengths > xyTrueLength))]/float(360)*2.0*np.pi )
```

```
    eDeps[np.where((lengths > xyMax) & (lengths <= otherDim) & (lengths <= xyTrueLength))] = eLength * z / np.cos( zAng[np.where((lengths > xyMax) & (lengths <= otherDim) & (lengths <= xyTrueLength))]/float(360)*2.0*np.pi )
    eDeps[lengths > otherDim] = eLength * xyMax / np.sin( zAng[lengths > otherDim]/float(360)*2.0*np.pi )

    eDepProb = zProb*numRep/float(360)
    return (eDeps, eDepProb)

if __name__ == '__main__':

    pool = mp.Pool(NUM_PROCS)
    detTypes = ['NaI','PVT']
    detOrients = ['HorizLong','HorizShort','Vertical']

    for k in range(len(detTypes)):

        print('For ' + detTypes[k] + '...')

        if k==0:
            NaI = True
        else:
            NaI = False

        for l in range(len(detOrients)):

            print('\t' + detOrients[l] + '...')

            if l<2:
                Horiz = True
                if l==0:
                    LongUp = True
                else:
                    LongUp = False
            else:
                Horiz = False

            if NaI:
                short =  5.08
                med   = 10.16
                long  = 40.64
                eLength = 3.667*1.305
            else:
                short =  6.35
                med   = 16.51
                long  = 62.31
                eLength = 1.032*1.956

            if Horiz:
                yFull = long
                if LongUp:
                    zFull = short
                    xFull = med
                else:
                    zFull = med
                    xFull = short
            else:
                zFull = long
                xFull = short
```

```
        yFull = med

    import math
    xDims = np.arange(0,math.ceil(xFull*10)/10, LENGTH_RESOLUTION)
    yDims = np.arange(0,math.ceil(yFull*10)/10, LENGTH_RESOLUTION)
    zDims = np.arange(0,math.ceil(zFull*10)/10, LENGTH_RESOLUTION)

    size = (len(zDims)*(2*len(xDims) + 2*len(yDims) - 3) + 4*(len(xDims)-1)*(len(yDims-1))) * (90/ANGLE_RESOLUTION)**2
    eDeps = np.zeros(size)
    allData = pd.DataFrame({'Energy':eDeps, 'Probability':eDeps})
    del eDeps

    b = 0
    print('\t\tCalculating. 0% complete...              ', end='\r')
    for m in range(len(xDims)):
        for n in range(len(yDims)):

            x1 = xDims[m]
            x2 = xFull - x1
            y1 = yDims[n]
            y2 = yFull - y1

            if x1 == 0:
                x = xFull
                if y1 == 0:
                    y = yFull
                    for zLen in zDims:
                        z = zFull - zLen
                        res = pool.apply_async(calcPaths,args=(x,y,z,eLength,4,))
                        eDepAdd, eDepProbAdd = res.get()
                        add = len(eDepAdd)
                        allData['Energy'][b:b+add] = eDepAdd
                        allData['Probability'][b:b+add] = eDepProbAdd
                        b += add
                else:
                    for y in (y1, y2):
                        for zLen in zDims:
                            z = zFull - zLen
                            res = pool.apply_async(calcPaths,args=(x,y,z,eLength,2,))
                            eDepAdd, eDepProbAdd = res.get()
                            add = len(eDepAdd)
                            allData['Energy'][b:b+add] = eDepAdd
                            allData['Probability'][b:b+add] = eDepProbAdd
                            b += add
            elif y1 == 0:
                y = yFull
                for x in (x1,x2):
                    for zLen in zDims:
                        z = zFull - zLen
                        res = pool.apply_async(calcPaths,args=(x,y,z,eLength,2,))
                        eDepAdd, eDepProbAdd = res.get()
                        add = len(eDepAdd)
                        allData['Energy'][b:b+add] = eDepAdd
                        allData['Probability'][b:b+add] = eDepProbAdd
                        b += add
            else:
                z = zFull
```

```
                    for x in (x1,x2):
                        for y in (y1, y2):
                            res = pool.apply_async(calcPaths,args=(x,y,z,eLength,1,))
                            eDepAdd, eDepProbAdd = res.get()
                            add = len(eDepAdd)
                            allData['Energy'][b:b+add] = eDepAdd
                            allData['Probability'][b:b+add] = eDepProbAdd
                            b += add
                amount = b/float(size)*100
                print('\t\tCalculating. ' + str(round(amount,2)) + '% complete...        ', end='\r')

        binWidth = ENERGY_BIN_WIDTH
        print('\t\tEnergy data calculated. Binning into ' + str(binWidth*1000) + ' keV energy bins...')
        filename = detTypes[k] + '-' + detOrients[l] + '-eDepsAndProbs.csv'

        minErg = allData['Energy'].min()
        maxErg = allData['Energy'].max()

        ergBins = np.arange(int(minErg), int(maxErg)+1+binWidth,binWidth)
        allData['Energy Bin'] = pd.cut(allData['Energy'],bins=ergBins)

        outData = allData.groupby('Energy Bin')['Probability'].sum()
        del allData

        print('\t\tData binned. Saving...')

        outData.to_csv(detTypes[k] + '-' + detOrients[l] + '-eDepsAll-binnedProbability-' + str(binWidth) + 'MeVbins.csv')
        del outData
```

APPENDIX B

CONSIDERATION OF AN ALTERNATE EXPECTED NEUTRON COUNT RATE PREDICTION METHODOLOGY

Additional methods exist to estimate the expected neutron count rate value in Chapter 5. One such method applies a generalized relation between the expected neutron and muon count values implied by Eq. 5.1 (shown in Eq. B.1 below) as shown in Eq. B.2, where the expected count values equal the products of the average count rates and the observation time. The existence of that relationship suggests that the count rates of both particles can be considered as a joint probability distribution of two Poisson random variables, which can be calculated using Eq. B.3. This concept can be applied to estimate the expected number of neutron counts, η, for background conditions. One way to make this estimate is to take the natural logarithm of Eq. B.3, take the derivative with respect to η, and calculate where that equals zero as shown below.

As mentioned above, the estimate of η shown in Eq. B.4 is valid when calculated with background observations n and m. However, it cannot be used as a dynamic estimate of η because observations of n may not be from background once the mobile search begins, as bias would be introduced if an observation was not from background. This limits the application of Eq. B.4 to estimating a constant expected value similar to the method mentioned in Chapter 5. It would still require a measurement prior to the mobile search and still suffer from the same issues. Despite this, a potential dynamic estimation is still possible using a similar derivation that would instead calculate the most likely value of μ.

The derivation used to obtain Eq. B.4 would similarly be used to calculate the most likely value of μ as shown in Eq. B.5. The value of μ from Eq. B.5 would then be used in Eq. B.1 to estimate η, and the result of that would be used to indicate how likely a neutron count observation, n, would occur from background (again, applying Eq. 5.3 and Eq. 5.4). However, like the estimation in Eq. B.4, the final estimation of η by way of Eq. B.5 would see some bias if n were a non-background observation, albeit not as large as that from Eq. B.4's estimate. Unfortunately, this potential for bias means the estimators from Eq. B.4 and Eq. B.5 are not as useful as simply considering a muon count observation, m, as an estimate of μ, which will then be used to estimate η using Eq. 5.1.

$$\bar{n} = \alpha \bar{m}^{\beta} \;\Leftrightarrow\; \bar{m} = \left(\frac{\bar{n}}{\alpha}\right)^{1/\beta} \tag{B.1}$$

$$\bar{n}t = \alpha \bar{m}^{\beta} t \;\Leftrightarrow\; \bar{m}t = \left(\frac{\bar{n}}{\alpha}\right)^{1/\beta} t$$

$$\eta = \alpha \bar{m}^{\beta-1} \mu \;\Leftrightarrow\; \mu = \left(\frac{\bar{n}^{1-\beta}}{\alpha}\right)^{1/\beta} \eta \tag{B.2}$$

Where:

$\bar{n},\ \bar{m} =$ average neutron and muon count rates, respectively [s^{-1}]
$\alpha, \beta =$ constants from an empirical fit with a given neutron-muon detector combination
$t =$ observation time [s]
$\bar{n}t \approx \eta =$ expected neutron counts in time t
$\bar{m}t \approx \mu =$ expected muon counts in time t

$$\Pr(N = n, M = m) = \Pr(N = n) \cdot \Pr(M = m) = \frac{\eta^n}{n!} e^{-\eta} \frac{\mu^m}{m!} e^{-\mu} \tag{B.3}$$

Where:

$N,\ M =$ Poisson random variables of neutron and muon counts, respectively, observed in a given time with respective expected values η and μ
$n,\ m =$ observations of N and M, respectively
$\Pr(N = n; M = m) =$ the probability of observing both n from N and m from M
$\eta,\ \mu =$ expected number of counts from Poisson random variables N and M, respectively

$$f(\eta) = \ln\left(\frac{\eta^n}{n!} e^{-\eta} \frac{\mu^m}{m!} e^{-\mu}\right)$$

$$f(\eta) = n\ln(\eta) - \eta + m\ln(\mu) - \mu$$

$$f(\eta) = n\ln(\eta) - \eta + m\ln\left(\left(\frac{n^{1-\beta}}{\alpha}\right)^{1/\beta} \eta\right) - \left(\frac{n^{1-\beta}}{\alpha}\right)^{1/\beta} \eta \qquad \text{using Eq. B.2}$$

$f(\eta)$ is maximized where $\frac{\partial f}{\partial \eta} = 0$:

$$\frac{\partial f}{\partial \eta} = \frac{n}{\eta} - 1 + \frac{m}{\eta} - \left(\frac{n^{1-\beta}}{\alpha}\right)^{1/\beta} = 0$$

$$\frac{n - \eta + m - \eta\left(\frac{n^{1-\beta}}{\alpha}\right)^{1/\beta}}{\eta} = 0$$

$$n - \eta + m - \eta\left(\frac{n^{1-\beta}}{\alpha}\right)^{1/\beta} = 0$$

$$\eta + \eta\left(\frac{n^{1-\beta}}{\alpha}\right)^{1/\beta} = n + m$$

$$\eta\left(1 + \left(\frac{n^{1-\beta}}{\alpha}\right)^{1/\beta}\right) = n + m$$

$$\eta = \frac{n + m}{1 + \left(\frac{n^{1-\beta}}{\alpha}\right)^{1/\beta}} \qquad \text{(B.4)}$$

$$f(\mu) = \ln\left(\frac{\eta^n}{n!}e^{-\eta}\frac{\mu^m}{m!}e^{-\mu}\right)$$

$$f(\mu) = n\ln(\eta) - \eta + m\ln(\mu) - \mu$$

$$f(\mu) = n\ln\left(\alpha m^{\beta-1}\mu\right) - \alpha m^{\beta-1}\mu + m\ln(\mu) - \mu \qquad \text{using Eq. B.2}$$

$f(\mu)$ is maximized where $\frac{\partial f}{\partial \mu} = 0$:

$$\frac{\partial f}{\partial \mu} = \frac{n}{\mu} - \alpha m^{\beta-1} + \frac{m}{\mu} - 1 = 0$$

$$\frac{n - \alpha m^{\beta-1}\mu + m - \mu}{\mu} = 0$$

$$n - \alpha m^{\beta-1}\mu + m - \mu = 0$$

$$\mu + \alpha m^{\beta-1}\mu = n + m$$

$$\mu\left(1+\alpha m^{\beta-1}\right)=n+m$$

$$\mu=\frac{n+m}{1+\alpha m^{\beta-1}} \tag{B.5}$$